

THE ELECTRON-PHONON INTERACTION
IN A TWO DIMENSIONAL ELECTRON GAS

by

Nicholas Peter Hewett, B.Sc.

Thesis submitted to the University of Nottingham
for the degree of Doctor of Philosophy

December 1988

For my parents

CONTENTS

	<u>Page</u>
ABSTRACT	
CHAPTER ONE: Introduction	1
CHAPTER TWO: Experimental Technique	3
2.1 Introduction	3
2.2 Stress Apparatus	3
2.2.1 Thermometry	4
2.2.2 The Stress Application System	6
2.3 Device Design	7
2.4 Sample Mounting and Thermometer Contacts	8
2.5 Data Collection	9
2.5.1 Thermometry	9
2.5.2 Computerised Data Collection System	11
2.5.3 The Gate Voltage Sweep Unit	13
2.6 Commissioning the Apparatus	14
2.6.1 Electrical Interference	14
2.6.2 Noise and Accuracy of the Technique	14
2.6.3 Discussion of Design Compromises	15
CHAPTER THREE: The Silicon Inversion Layer	18
3.1 Introduction	18
3.2 Band Bending	18
3.3 Silicon Conduction Band Structure	19
3.4 Electric Quantisation	19
3.5 Electrical Transport Properties of a 2DEG	21
3.5.1 Introduction	21
3.5.2 Scattering Mechanisms	23
3.5.3 Localisation	25
3.6 Electrical Transport in a Magnetic Field	26
3.6.1 Introduction	26
3.6.2 A 2DEG in Crossed Electric and Magnetic Fields	27

3.6.3	The Quantum Hall Effect	31
3.6.4	The Current Distribution in the Quantum Hall Regime	34
CHAPTER FOUR: Theory of Phonon Emission from a Heated 2DEG		36
4.1	Introduction	36
4.1.1	The Electron-Phonon Interaction	36
4.1.2	Emission in a Quantising Magnetic Field	41
4.1.3	Discussion of the Main Theoretical Results	43
4.2	Phonon Scattering in Si(B)	47
4.2.1	Introduction to Phonon Scattering	47
4.2.2	Scattering Mechanisms	48
	4.2.2a Intrinsic Processes	48
	4.2.2b Extrinsic Processes	50
4.2.3	The Boron Acceptor in Silicon	51
4.3	Phonon Focussing	56
4.4	Review of previous work	57
4.4.1	Zero Magnetic Field	57
4.4.2	Quantising Magnetic Field	61
CHAPTER FIVE: Computer Modelling		64
5.1	Introduction	64
5.2	Theory	65
5.3	Method of Solution	68
5.4	Results	69
5.5	Discussion	70
5.6	Future Work	75
CHAPTER SIX: Experimental Results		77
6.1	Thermal Conductivity	77
6.2	Device Characterisation	78
6.3	Zero Magnetic Field Results	79
6.3.1	Phonon Emission Experiments	79
6.3.2	Electrical Transport Experiments	88
6.4	Quantising Magnetic Field Results	92

6.5	The Stress Tuned Phonon Filter	100
6.6	Conclusions and Future Experiments	102
	APPENDIX A: Computer Modelling Program	106
	REFERENCES	109
	ACKNOWLEDGEMENTS	112

ABSTRACT

At low temperatures the predominant energy loss mechanism for a Joule-heated two dimensional electron gas (2DEG) in a metal oxide semiconductor field effect transistor (MOSFET) is by acoustic phonon emission. By very accurately measuring the temperature gradient developed along the silicon substrate the phonon emission has been investigated as a function of electron concentration, device power, magnetic field and temperature.

In zero magnetic field the results show the cut-off predicted theoretically in the maximum phonon momentum that can be emitted in the plane of the 2DEG for low electron concentrations. It is also found that the momentum of the emitted phonons perpendicular to the plane of the 2DEG is restricted by the width of the 2DEG for the high resistivity (1000 Ωcm) substrates used. For carrier concentrations greater than $4.9 \times 10^{16} \text{ m}^{-2}$ phonon emission from an upper subband is seen. Electrical measurements indicate that the high mobility ($1.2 \text{ m}^2 \text{ V}^{-1} \text{ s}^{-1}$) of the devices used leads to changes in the screening of scattering potentials by the electrons being important. This is also seen in the phonon emission experiments.

Experiments performed in quantising magnetic fields up to 7 T show that for the powers used ($0.2 \mu\text{W mm}^{-2} - 500 \mu\text{W mm}^{-2}$) the phonons emitted arise from intra-Landau level scattering. Oscillations in the temperature of a thermometer situated directly opposite the middle of the 2DEG are attributed to the movement of the phonon emission to the corners of the 2DEG when the Fermi level is between Landau levels (the Quantum Hall regime). Other trends are attributed to the width of the Landau level limiting the maximum

phonon energy that can be emitted.

Attempts to use a stress tuned phonon filter to probe the frequency dependence of the phonon emission failed due to experimental difficulties.

CHAPTER 1

Introduction

The development of very sensitive thermal conductivity measurement techniques using external perturbations, such as magnetic fields and uniaxial stress, has allowed phonon spectroscopy to contribute results complementary to those provided by photon spectroscopy. The experiments are technically demanding but the equipment that has evolved allows the measurement of temperature differences with micro Kelvin resolution. The work presented in this thesis uses these low temperature thermal conductivity techniques to investigate the phonon emission from a Joule-heated two dimensional electron gas (2DEG) in a silicon metal oxide semiconductor field effect transistor (MOSFET).

In Chapter 2 the apparatus and experimental technique are presented. This equipment allows up to 200 N of force and a magnetic field of 7 T to be applied to the sample. Also presented is the data collection system which includes a computer controlled feedback apparatus developed to ensure that the electrical power dissipated in the 2DEG remains constant as the device resistance varies.

Chapter 3 introduces the basic electrical properties of a silicon MOSFET and then outlines, theoretically, the effect of a quantising magnetic field on a 2DEG.

The electron-phonon interaction in a 2DEG is treated theoretically in Chapter 4. This treatment is then used to predict the main phonon emission effects expected experimentally. Phonon focussing and phonon scattering in the Si(B) substrates will alter the detected phonon emission and so these processes are considered. The use of the boron impurity in silicon as a stress tuned phonon filter is introduced.

To aid the analysis of the experimental results presented in Chapter 6 a computer simulation of the temperature gradient along the silicon substrate, for various experimental geometries, was developed. The results produced by this simulation, and the validity of the assumptions used are discussed in Chapter 5.

Chapter 6 details the experimental results and presents an analysis based on these results. Comparison with the theoretical predictions is made and the discrepancies discussed.

CHAPTER 2Experimental Technique2.1 INTRODUCTION

The measurements reported in this thesis use the steady state Searle's Bar technique. A rod of uniform cross section, A , has heat introduced at one end at a constant rate, \dot{Q} . By measuring the temperature difference, ΔT , between two thermometers a distance, l , apart the thermal conductivity, K , can be calculated from

$$K(T) = (l/A) \cdot \dot{Q}/\Delta T \quad (2.1)$$

The quantity (l/A) is called the form factor. This equation assumes that $\Delta T \ll T/10$ where T is the mean temperature of the sample between the thermometers.

2.2 STRESS APPARATUS

The cryogenic insert used for this work has been described previously by Russell (1988) as the 'stress apparatus', and I am very grateful to Dr P A Russell and Mr B Hill for their considerable help in the design and construction of this equipment. It consists of an isolated helium pot situated inside an evacuated chamber. This is suspended on stainless steel tubes from a top plate incorporating a sliding collar to allow the height of the insert to be adjusted. Four of the support tubes provide rigidity allowing large tensile stresses to be applied to the sample with a stainless steel

wire which passes down the centre of the insert. The remaining tubes provide electrical lead throughs and pumping lines. The entire insert is placed within a liquid helium dewar supplied by Oxford Instruments PLC, and the sample stage in the evacuated chamber fits into the bore of a 7 Tesla split pair superconducting magnet supplied by Cryogenic Consultants Ltd. The dewar is mounted on a rotating turntable while the insert is fixed. This allows the relative angle of the sample and the applied magnetic field to be altered without removing the insert from the dewar.

The isolated pot and sample area is shown in Figure 2.1. Liquid helium is drawn into the pot via a fill tube and needle valve. With the needle valve closed the vapour pressure in the pot can be reduced by pumping, and this lowers the temperature of the pot and sample area to approximately 1 K. The pot is made of copper with a thickened base onto which the sample stage is bolted. This consists of a thick copper base into which three copper rods are bolted. The copper rods pass through three copper discs, which add rigidity, and are then terminated at a fourth copper disc. The sample is located between the third and fourth discs. The length of the copper rods required to form this sample stage meant that they could not be made from spectroscopically pure copper, and the effect of this will be discussed in section 2.6.3.

2.2.1 Thermometry

The thermometry used is identical to that described by Heraud (1985) and Ghazi (1978). The principal thermometers are two 27 Ω , 1/8 W, Allen-Bradley carbon resistors which are mounted in

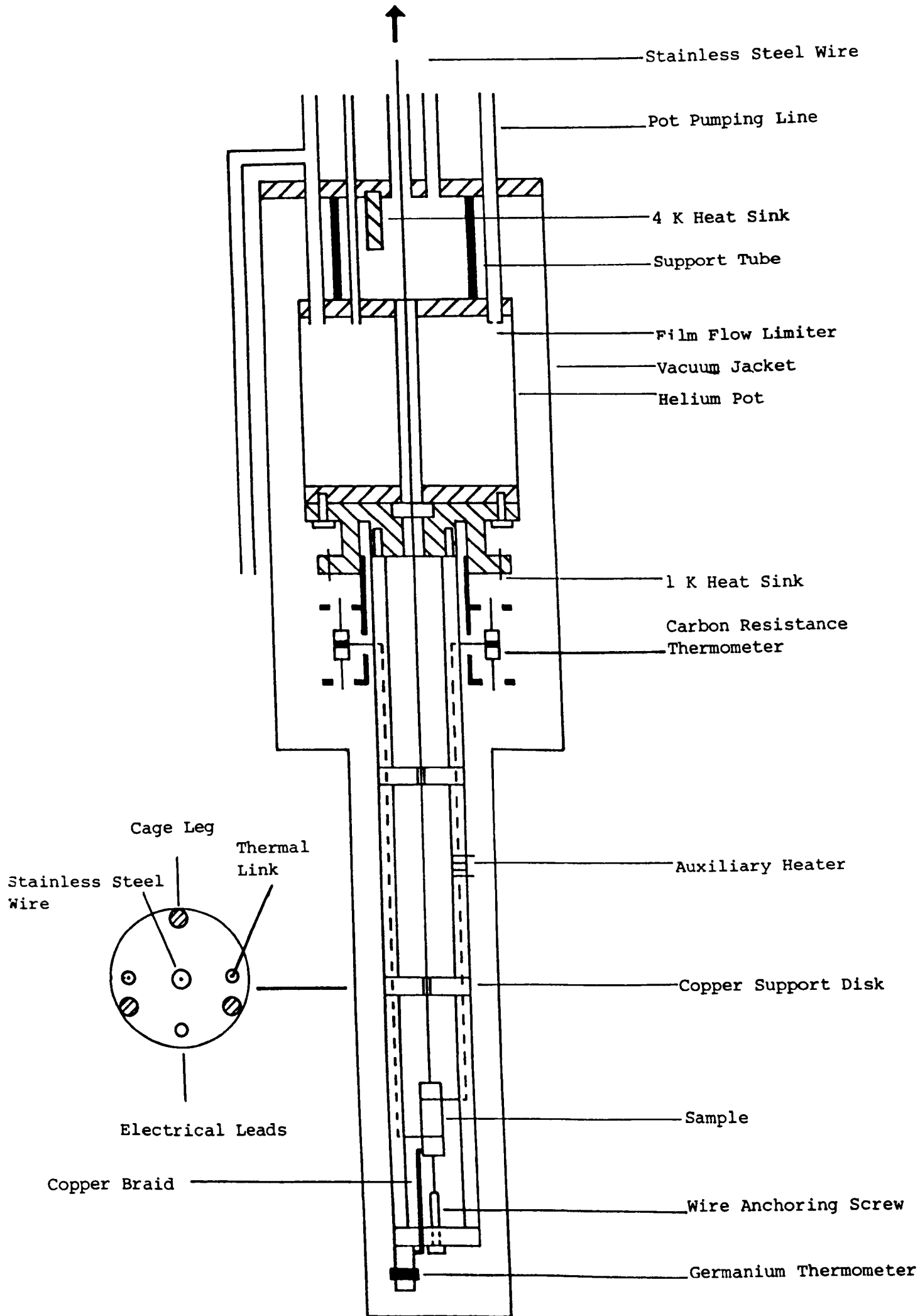


Figure 2.1: Schematic Diagram of Stress Apparatus

brass supports attached to the base of the helium pot approximately 17 cm above the centre of the magnetic field to reduce magneto-resistive effects. The resistors have all the outer enamel removed and 24 gauge copper wire wrapped around them in contact with the carbon granules. This copper wire is then soldered with 'non-superconducting' solder to 24 gauge copper wires which link the thermometers to the sample. At each of the copper discs these thermal links are supported by 0.1 mm fishing thread cradles to prevent vibration, and thermally isolate them from the rest of the apparatus. The connection of the thermal links to the sample is discussed in section 2.4.

The carbon resistance thermometers are calibrated against two pre-calibrated germanium resistance thermometers mounted in a copper block at the base of the sample area. The germanium thermometers were supplied calibrated over the range 1.5 - 50 K.

To raise the temperature of the entire sample stage an auxiliary heater ($\approx 1 \text{ k}\Omega$, non-inductively wound evanohm wire) is mounted on one of the copper rods, halfway between the sample and the helium pot. To introduce heat directly into the sample a main heater (strain gauge RS632-146) is either mounted directly on the sample with GE varnish, or mounted alongside the sample on silver foil attached to the sample with GE varnish. Power for the heaters is provided by two 12 V car batteries via a control and switch unit.

Thirty six electrical leads allow up to four Allen-Bradley thermometers and ten device connections. The leads are thermally anchored at 4.2 K by tightly wrapping them around two copper posts

soldered into the top of the evacuated chamber. They are also thermally anchored at 1 K both by sticking them with GE varnish to the outside of the pot, and by heatsunk electrical connectors in the sample stage base. To reduce any heat leak to a minimum, very long tightly coiled electrical leads are used for the connections between the 1 K heatsink and the thermometers.

2.2.2 The Stress Application System

Stress is applied to the sample by a stainless steel wire which runs along a central support tube from the top of the insert, into the evacuated chamber, and down to the base of the sample stage. At the top of the insert is the apparatus shown in Figure 2.2. The top of the stainless steel wire is attached to a brass rod which is a tight sliding fit in a rubber O-ring seal. This seal is essential as it maintains the vacuum in the sample area. The brass rod is attached to a piston shaped stainless steel piece which is used to compress a quartz load transducer situated in a brass cup. Load is applied to this cup via a screw wheel and threaded bar which incorporates a slot to prevent rotation. An alternative system capable of providing a continuously variable stress was developed by Mr B Hill and applies the load with a gas actuated piston.

The load applied to the sample is measured by a quartz washer. As the quartz load transducer is compressed the charge produced by the piezo-electric effect is amplified with a charge amplifier (Kistler Instruments 5007) and measured on an x-t chart recorder.

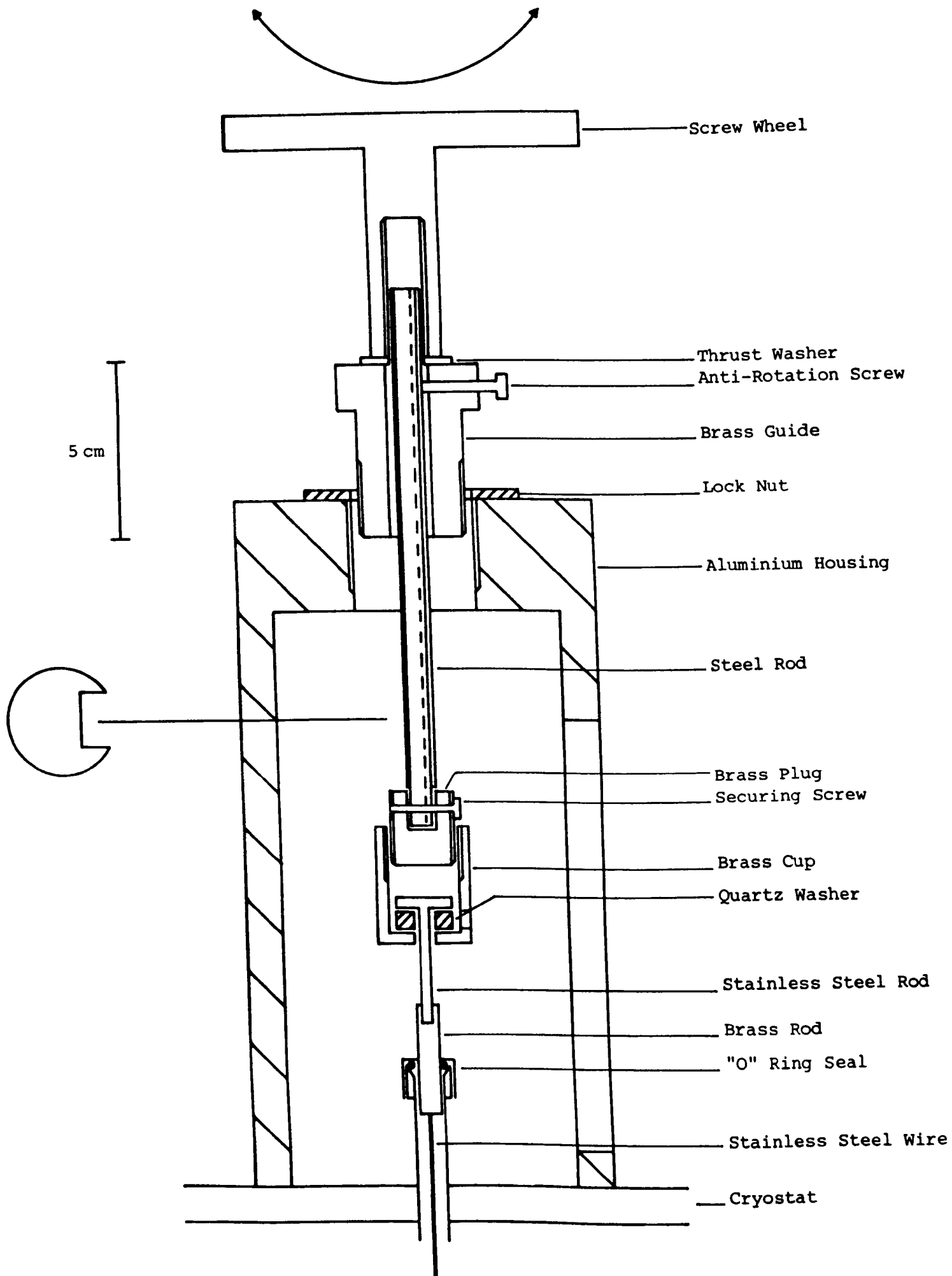


Figure 2.2: Schematic Diagram of the Stress Application Apparatus

2.3 DEVICE DESIGN

The devices used for this work were silicon MOSFETs fabricated using planar technology at Southampton University by Mr C M K Starbuck and his colleagues in the Department of Microelectronics and Information Engineering. I am indebted to Dr P A Russell for designing the devices.

A basic MOSFET consists of a silicon substrate with two highly doped regions, the source and drain, to which electrical contact is made. An insulating layer is grown on the substrate between these two contacts, and a metal film deposited on this insulating region to act as the gate electrode. This is shown schematically in Figure 2.3.

The device type used is designated PARSGD, see Russell (1988). It was fabricated on 1000 Ω cm p-type (boron doped) (100) surface orientation, 380 μ m thick, silicon wafers supplied by Wacker Chemtronic. The specification of the original wafers was very important due to the experimental requirements. The low boron concentration ($\sim 10^{13}$ cm⁻³) was required to restrict the effects of resonant phonon scattering from the strain split acceptor ground state. Carbon and oxygen impurities also increase the phonon scattering by introducing random strains which split the boron groundstate. The wafer manufacturers specified an upper limit for the carbon concentration of 2×10^{16} cm⁻³ and for oxygen of 1×10^{16} cm⁻³. See Chapter 4 for further details of phonon scattering by Si(B).

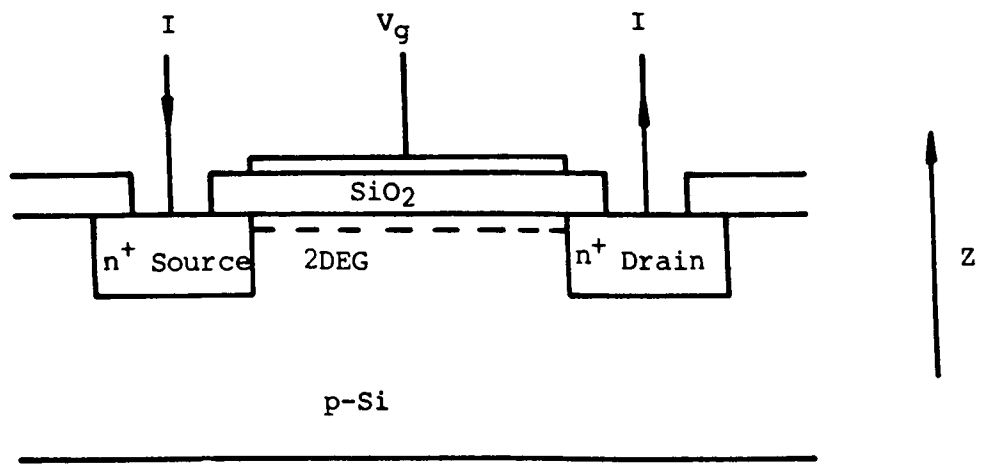


Figure 2.3: A Schematic Diagram of a Si MOSFET

The large active area of PARSGD, $1 \times 3 \text{ mm}^2$, is required to dissipate enough power in the 2DEG to develop a measurable temperature gradient along the sample without raising the electron temperature excessively by using high power densities. A consequence of such a large gate area is an increased probability of pin holes in the insulating oxide layer allowing the gate electrode to short out. To prevent this a substantially thicker oxide layer (nominally 800 nm) than usual was used, leading to correspondingly higher gate voltages.

The oxide layer contains two separate oxide regions produced under different growth conditions. A 650 nm layer, grown using normal wet oxidation, and a 150 nm layer of higher quality oxide produced with HCl present during growth. This layer, although much slower to grow, has a far lower concentration of electron trap states as the HCl reduces the impurities present in the oxide by a gettering action. The reduction in the density of electron traps in the oxide near the inversion layer increases the device mobility and lowers the threshold voltage.

2.4 SAMPLE MOUNTING AND THERMOMETER CONTACTS

The sample mounting is shown in Figure 2.4. The sample is glued, using Bostik Clear adhesive, into two copper jaws which are loosely pinned into two stainless steel tongue pieces. The tongues are shaped to allow several degrees of movement in all axes to prevent any random loading. Threaded stainless steel studs fit into the tongue pieces allowing the sample height to be adjusted. A

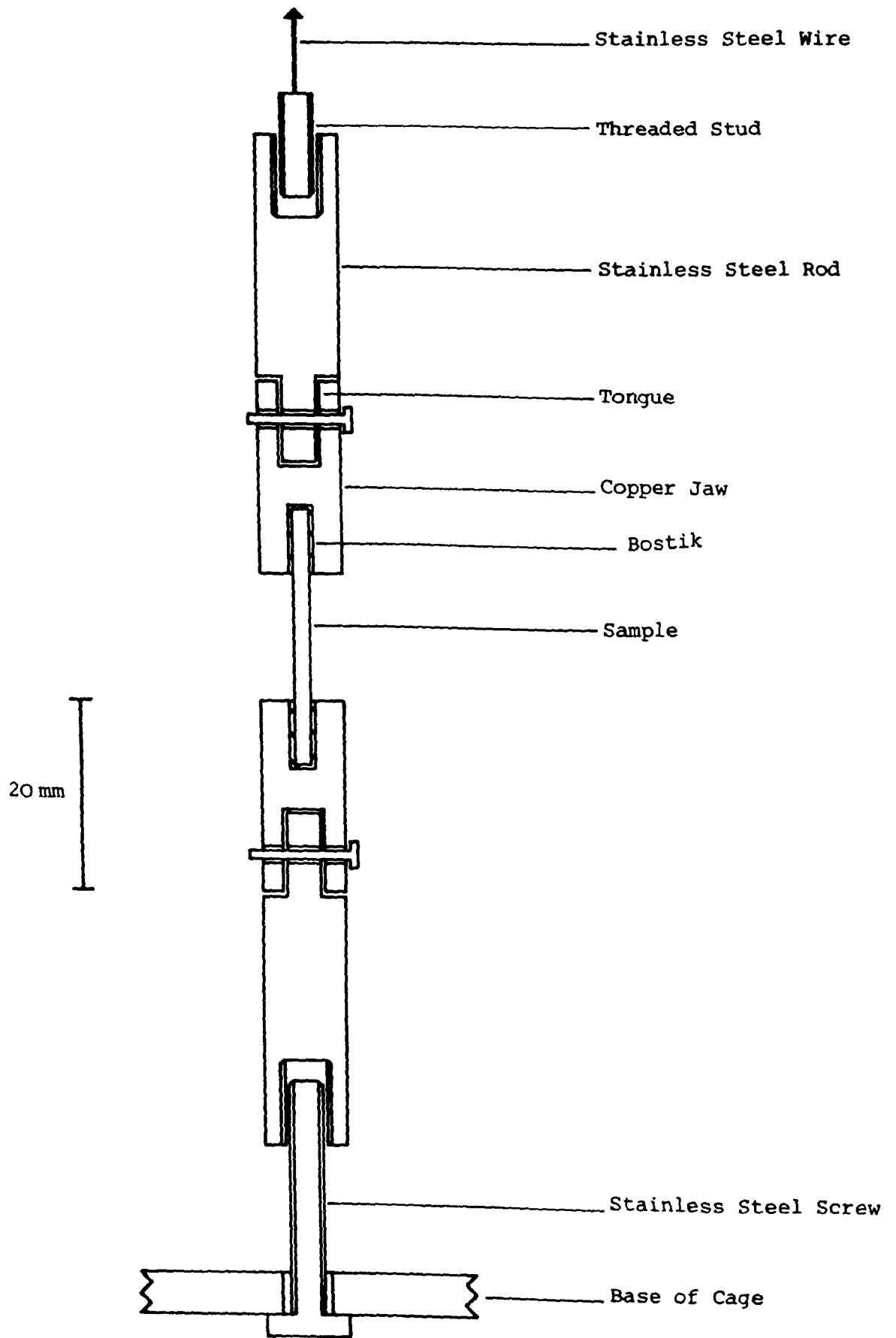


Figure 2.4: A Schematic Diagram of the Sample Mounting

thick copper braid connecting the lower jaw to the sample stage provides the heatsink for the sample.

Bostik Clear adhesive is used to secure the sample as it does not appear to produce stress in the sample around the jaws on cooling. At cryogenic temperatures more than 200 N force can be applied to the sample.

The thermometer contacts are made of silver foil strips, 0.05 mm thick, 99.95% pure, cut into 10 x 0.5 mm² strips (approximately). These are glued onto the sample with GE varnish, and are soldered to the thermal links with 'non-superconducting' solder. This type of contact appears to apply very little stress to the sample so that any additional splitting of the boron groundstate is minimal. The flexibility of the silver foil also allows the sample to move freely as stress is applied, virtually eliminating any random stress problems, and reducing the probability of the contacts separating from the sample. Additionally, the contacts can be cut to any size. I am very grateful to Mrs C Murray and Dr M N Wybourne for their help with these contacts. They have previously been used by Odoni et al (1983), Heraud (1985) and Russell (1988).

2.5 DATA COLLECTION

2.5.1 Thermometry

The resistance of the two Allen-Bradley carbon resistors is measured using an AC technique. A low noise inductive ratio-arm bridge supplied by Automatic Systems Laboratory Ltd, supplies an

excitation voltage to the resistors, and an out of balance signal and reference signal to an EG and G 9503SC phase sensitive detector. The bridge measures the ratio

$$f = \frac{R_a}{R_a + R_b} \quad (2.2)$$

Where R_a and R_b are the resistors being compared. The wiring of the inserts allows the selection of two ratios

$$f_1 = \frac{R_f}{R_f + R_1} \quad (2.3)$$

and

$$f_{12} = \frac{R_1}{R_1 + R_2} \quad (2.4)$$

R_1 is the thermometer nearest the heat sink and R_2 is nearest the main heater. R_f is a 1 k Ω reference resistor fixed to the 4.2 K heat sink.

f_1 and f_{12} were calibrated against a precalibrated germanium thermometer by supplying heat with the auxiliary heater. We can see from equations (2.3) and (2.4) that

$$R_1 = R_f \left(\frac{1}{f_1} - 1 \right) \quad (2.5)$$

$$R_{12} = R_1 - R_2 = R_1 \left(2 - \frac{1}{f_{12}} \right) \quad (2.6)$$

A least squares fitting procedure is then used with the interpolation formulae

$$T = \frac{C_0}{(R_1 - \Delta)} + C_1 \quad (2.7)$$

$$R_{12} = C_2 + C_3 \cdot R_1 + C_4 \cdot R_1^2 \quad (2.8)$$

with the constants Δ , C_0 , C_1 , C_2 , C_3 , and C_4 as fitting parameters.

Heat was then supplied by the main heater developing a temperature gradient, ΔT , between the thermometers. Challis (1961) gives

$$\Delta T = \frac{R_{12} - R_{12}^0}{\left\{ \frac{dR_1}{dT} - \frac{1}{2} \frac{dR_{12}^0}{dT} \right\}_{T_0}} \quad (2.9)$$

Where R_{12}^0 is the value of R_{12} at the mean temperature $T_0 = T + \Delta T/2$. ΔT and T_0 are calculated using an iterative procedure which terminates when the change in ΔT is less than 1 part in 10^4 .

2.5.2 Computerised Data Collection System

For the experiments reported in this thesis, ΔT is measured while either the magnetic field, or, the gate voltage is swept. For any useful conclusions to be drawn, the device must dissipate constant power throughout these sweeps even though the device resistance is changing dramatically. This is achieved using an Acorn Master 128 computer as the controller of an IEEE system

comprising a Keithley 224 current source and three Keithley 195a digital voltmeters (DVMs). The source-drain voltage of the device is monitored on one DVM and the required current calculated by the computer and supplied by the current source. This procedure forms a feedback system with two main parameters controlling the amount of feedback and the speed of the feedback. These parameters must have suitable values to prevent the system oscillating from excessive or too rapid feedback, or from failing to keep up with the device resistance changes with too little or slow feedback.

A complete schematic diagram for the data collection system is shown in Figure 2.5.

Any change in ΔT produced by a change in either magnetic field or gate voltage, alters the ratio $f_{1,2}$ and, hence, the out of balance signal from the bridge. If the bridge has been previously balanced, the out of balance signal after it has passed through the PSD, ΔV , is directly proportional to the change in ΔT as long as this change in ΔT does not change the mean temperature of the sample significantly. ΔV is taken to the y-axis of an x-y recorder, and to one of the DVMs allowing it to be recorded by the computer. Another DVM is used to record the swept quantity which is also fed to the x-axis of the chart recorder. For gate voltage sweeps the applied voltage is stored directly, while for magnetic field sweeps the voltage developed across a $0.75 \text{ m}\Omega$ shunt resistance in series with the magnet is recorded.

During sweeps the computer stores four quantities, the source-drain current, the source-drain voltage, the out of balance

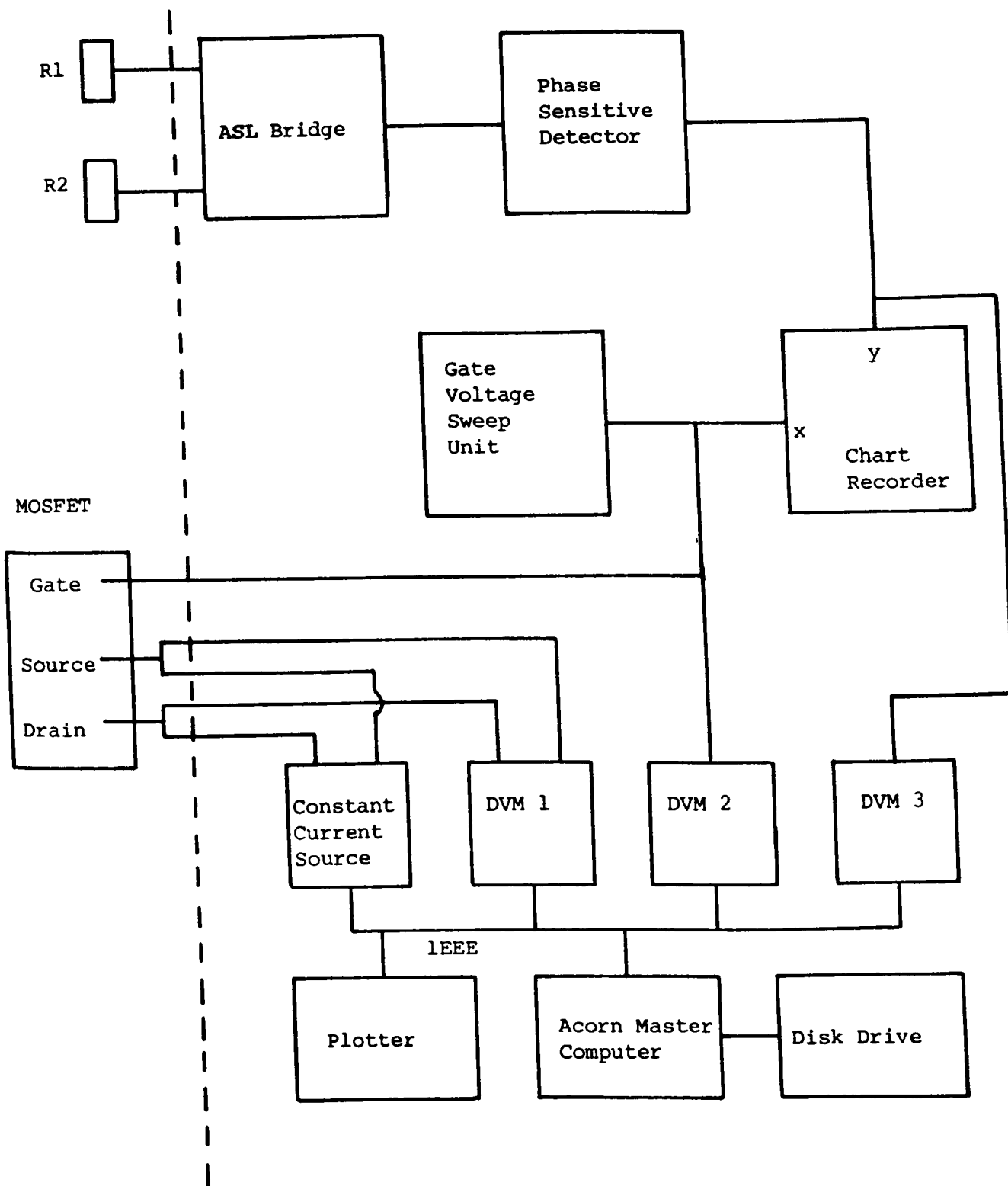


Figure 2.5: Schematic Diagram of the Data Collection System

signal and the swept quantity. With these data it is possible to calculate the device resistance, which is used to obtain the electron temperature, and the power dissipated, to check the constant power feedback system at each data point.

2.5.3 The Gate Voltage Sweep Unit

The thick oxide layer incorporated in the device design meant that to obtain a sufficient range of carrier concentrations gate voltages up to 250 V were required. Most commercial voltage sweep units only operate up to 10 V, so to overcome this a special sweep amplifier was constructed. Figure 2.6 shows the circuit diagram for this unit.

Three Farnell D100-1 power supplies provide a 300 V DC input. Part of this is used by the ICL7660 integrated circuit to produce a ± 12 V output to power the 741 operational amplifier. The rest is applied across an IRF830 power transistor (125 W, 500 V) in series with a 10 k Ω (20 W) resistor. With no gate voltage applied to the power transistor, all the voltage is applied to the output. If, alternatively, the gate voltage applied to the power transistor is sufficient to turn it fully on, all the voltage is dropped across the resistor, and the output voltage drops to zero. The power transistor gate voltage is provided by the 741 operational amplifier and is determined by the input from an 0 - 5 V Oxford Instruments PLC voltage sweep unit.

2.6 COMMISSIONING THE APPARATUS

2.6.1 Electrical Interference

Heraud (1985) experienced serious radio-frequency (rf) interference with a very similar apparatus. To overcome this the experiments were moved into a screened room supplied by Belling Lee Ltd with the mains supply passing into this room through rf filters (type Y20866). This should remove all interference above 10 kHz, and the first experiments confirmed that the interference was no longer present. In later experiments however, some electrical interference was observed, but this was originating from harmonics in the mains supply beating with the 375 Hz ac bridge excitation. To remove this noise it was necessary to renew the wiring connecting the ancillary equipment with the insert, paying great attention to the shielding and earthing. As a further precaution, the computer and digital electronic apparatus were removed completely from the screened room, connection being via screened cables. These measures reduced the electrical noise to a level significantly below other sources. Calculations suggest that the electrical noise levels should be around five times lower than the experimentally measured noise level.

2.6.2 Noise and Accuracy of the Technique

The major cause of the measured noise appears to be microphonic pickup by the Allen-Bradley resistors. Two main sources of vibrations were found, both connected with the Edwards ISC900 rotary pump. The first was actual vibrations of the pump being transmitted

by the pumping line. This was eliminated by securely bolting the pumping line to the wall of the laboratory. The second source is from the vibrating column of gas within the pumping line. To reduce this it will be necessary to include a large smoothing volume in series with the pot.

Typical noise levels in ΔT for the measurement system alone are $\pm 3 \mu\text{K}$. This rises to $\pm 8 \mu\text{K}$ with the constant power feedback system operating, though for low device powers (less than $30 \mu\text{W}/\text{mm}^2$) $\pm 6 \mu\text{K}$ is obtainable. The temperature gradients measured could have $\pm 1 \text{ mK}$ absolute errors due to day-to-day stability problems with the Allen-Bradley resistors used. To ensure that the data for each experimental run were consistent, all the initial temperature gradients for the sweeps performed were measured on one day. Absolute errors were also found to be a problem when magnetic fields were applied and this is discussed in section 2.6.3.

Long term temperature drifts due to the level of the liquid helium in the pot changing were not a problem with the experiments reported in this work. However, it is hoped to introduce a temperature controller supplied by Linear Research for later experiments.

2.6.3 Discussion of Design Compromises

The adaptation of the standard thermal conductivity apparatus to allow the application of large uniaxial stresses introduced several design compromises.

- 1 The sample is no longer free standing as the stainless steel loading wire forms an alternative heat path from the 'hot' end of the sample.
- 2 The main sample cage could not be made from spectroscopically pure copper rods as the joints required to form the long lengths needed would weaken the structure.
- 3 The sample could not be in intimate contact with the heatsink due to the flexible couplings required.

It is necessary to consider the heat path from the sample heater to the 1 K pot to assess the effect of these compromises. Heat introduced by the main heater (or device) will pass mostly down the sample creating a temperature gradient. A little may pass up the loading wire and this amount may vary with applied stress as any touching areas on the wire change. At either end, a temperature gradient across the glue fixing the sample into the jaws will be formed. The magnitude of this, and how magnetic field or stress may affect it, is unknown. The contact between the jaws and the tongue pieces, and between the lower tongue piece and the stress cage, will also be stress sensitive.

The main thermal path from the sample is through the lower jaw, copper thermal braid and the main stress cage which is also made with ordinary copper. An estimation of the effect of a magnetic field on the thermal conductivity of polycrystalline copper can be made from the data of Justi and Ascherman (1947) (reproduced by Olsen, 1962). Russell (1988) estimated that the ratio of the

resistivity at 300 K and 4 K, for the copper in our apparatus, is ~ 100 . Using this figure yields a change in the resistivity of ~ 100 in a magnetic field of 6 T. As the Lorentz number, the ratio of the thermal and electrical resistivities, is approximately constant for fixed temperature, we would expect the thermal resistivity to vary a similar amount. Changes of the thermal resistance between the sample and 1 K pot in a magnetic field can be seen in figure 2.7 as changes in the sample temperature. These temperature shifts will introduce errors into the measured ΔT s due to changes in the thermal conductivity of the substrate. To allow easy correction for this and for magnetothermal conductivity changes in the substrate, fixed magnetic fields were used and changes introduced by varying the gate voltage.

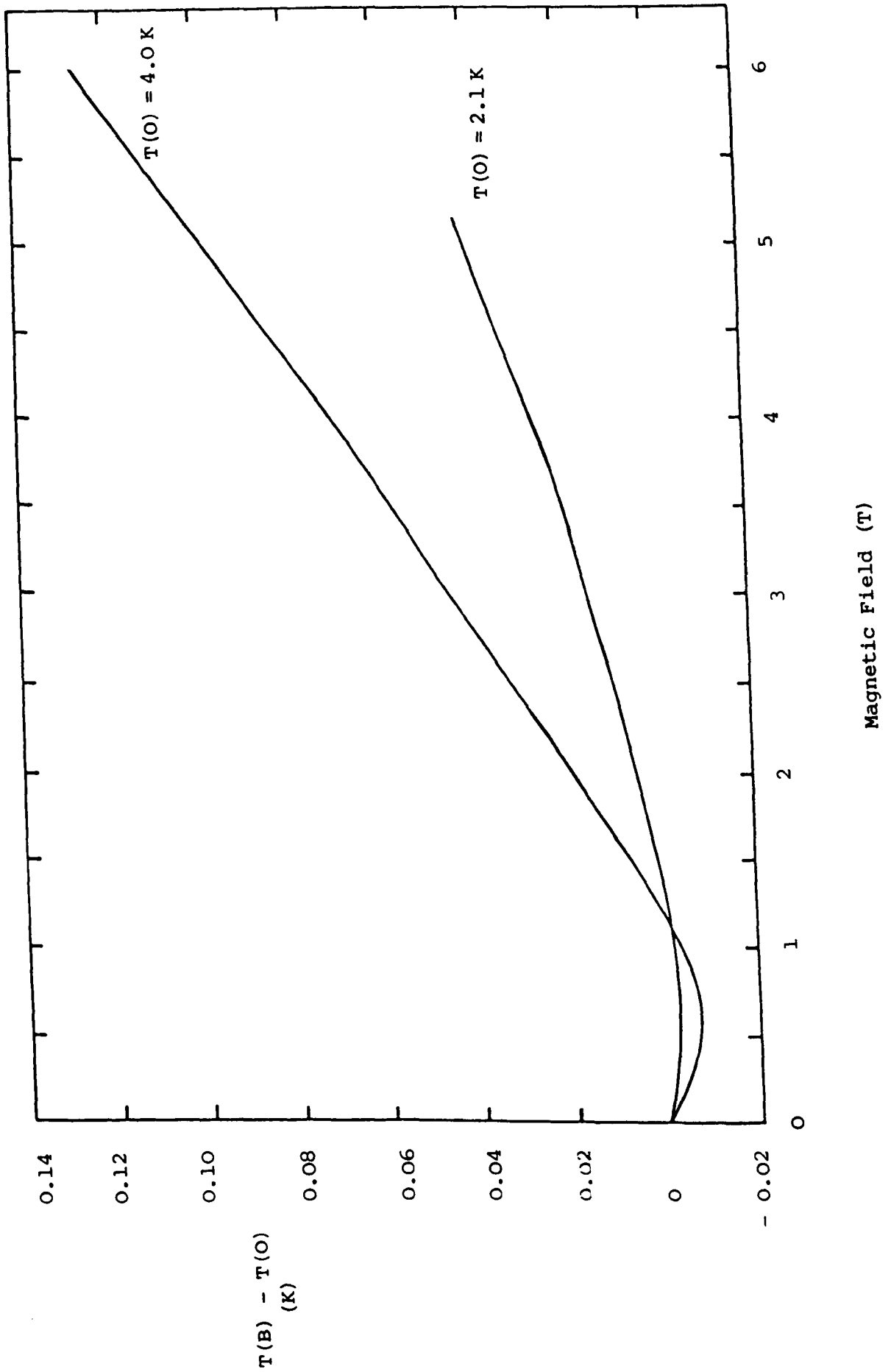


Figure 2.7: The Variation of Sample Temperature as a Function of Magnetic Field

CHAPTER 3

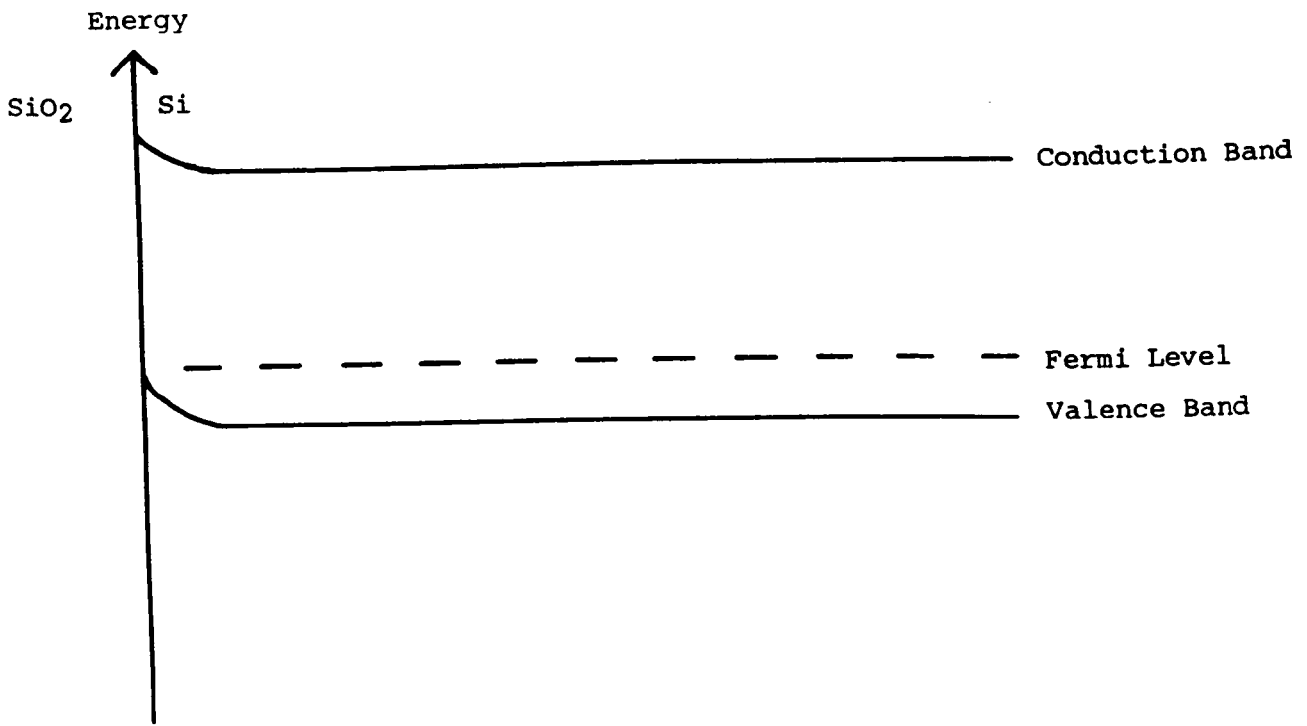
The Silicon Inversion Layer

3.1 INTRODUCTION

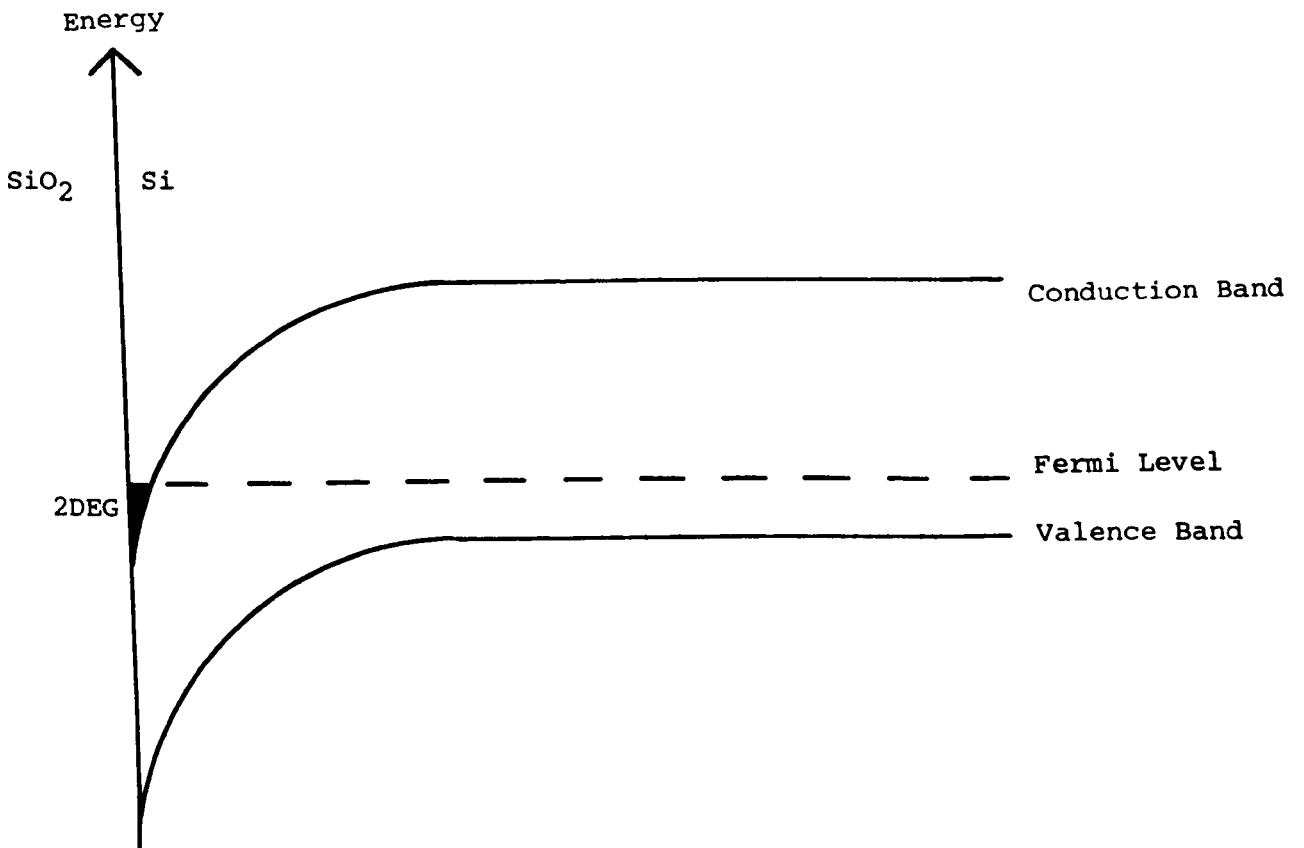
The MOSFET (shown in Figure 2.3) essentially has the form of a capacitor, the gate electrode forming the upper plate, the SiO_2 the dielectric and the p-type silicon the lower plate. The application of a positive voltage, V_g , to the gate induces a negative charge, Q , in the bottom plate. The conductivity of the silicon immediately under the gate can, thus, be significantly altered as the number of free carriers with no applied voltage is very low. This is the field effect, and was proposed as the basis of a useful device as early as 1930 by Lilienfeld (see Pepper 1977).

3.2 BAND BENDING

Figure 3.1 shows a cross section (not to scale) through the MOSFET for two different applied gate voltages. Figure 3.1(a) is with no applied gate voltage and exhibits slight bending of the conduction and valence bands at the oxide/silicon interface. This arises from a potential developed by the transfer of electrons to equalise the work functions of the different materials. There are also effects due to trapped charges and surface states. A positive voltage applied to the gate electrode, Figure 3.1(b), attracts electrons to the semiconductor surface and when the electron concentration is greater than the hole concentration in the bulk,



(a) $V_g = 0 \text{ V}$



(b) $V_g > 0 \text{ V}$

Figure 3.1: Schematic Diagram of the Band Bending in a Si MOSFET

the surface is said to be inverted. Electrons within this inversion region are confined in the direction perpendicular to the surface by a potential well formed by the oxide/silicon conduction bandgap (~ 3 eV) and the conduction band bending in the silicon. Schrieffer (1957) proposed that the electronic energy in this direction would be quantised leading to two-dimensional behaviour. At that time, however, it was thought that scattering would destroy this effect.

3.3 SILICON CONDUCTION BAND STRUCTURE

The constant energy surfaces of the conduction band minima in silicon have the form of six identical ellipsoids along the principal $\langle 100 \rangle$ directions. Their centres are positioned at $k = 0.85 k_0$, where k_0 is the distance between the centre and the edge of the Brillouin zone. The ellipsoidal shape results in a large anisotropy in the effective mass. For motion along the major axes the effective mass is given by $m_l = 0.916 m_0$ (m_0 = the free electron mass), while perpendicular to these axes $m_t = 0.19 m_0$. Thus, for motion in a potential well perpendicular to a (100) surface there will be two degenerate valleys corresponding to m_t , and four which correspond to the lighter mass m_l .

3.4 ELECTRIC QUANTISATION

The allowed energy levels for a "large" three-dimensional particle in a box form a quasi-continuum. The same problem, but with the particle confined to two dimensions, produces markedly different results as the allowed energy levels are a set of well defined separate sub-bands, with a quasi-continuum of levels within

the bands corresponding to motion in the two unconfined directions.

The symmetry of an inversion layer means that it can be treated as a one-dimensional electrostatic problem with the variation of the potential, V , in the z -direction given by Poisson's equation

$$\frac{d^2V}{dz^2} = - \frac{\rho(z)}{\epsilon_0} \quad (3.1)$$

where $\rho(z)$ is the charge density present and this can be written

$$\rho(z) = e[N_d - N_a + p(z) - n(z)] \quad (3.2)$$

where N_d , N_a , $p(z)$ and $n(z)$ are the concentrations of charged donors, charged acceptors, holes and electrons respectively.

The boundary conditions of the system are: (1) zero potential in the bulk at large distances from the gate and (2) the potential at the oxide/silicon interface is determined by the applied gate voltage. However, we must also solve Schrodinger's equation to obtain $n(z)$, and this is a function of the confining potential. Hence, it is necessary to solve Poisson's equation and Schrodinger's equation in a self-consistent manner to determine $V(z)$ and $\rho(z)$. Stern (1974) has done this and his results are shown in Figure 3.2. Two ladders of energy levels are present corresponding to the two different effective masses for the two-fold degenerate valleys, and the four-fold degenerate valleys. The levels shown are only for motion in the z -direction. Motion in the x and y

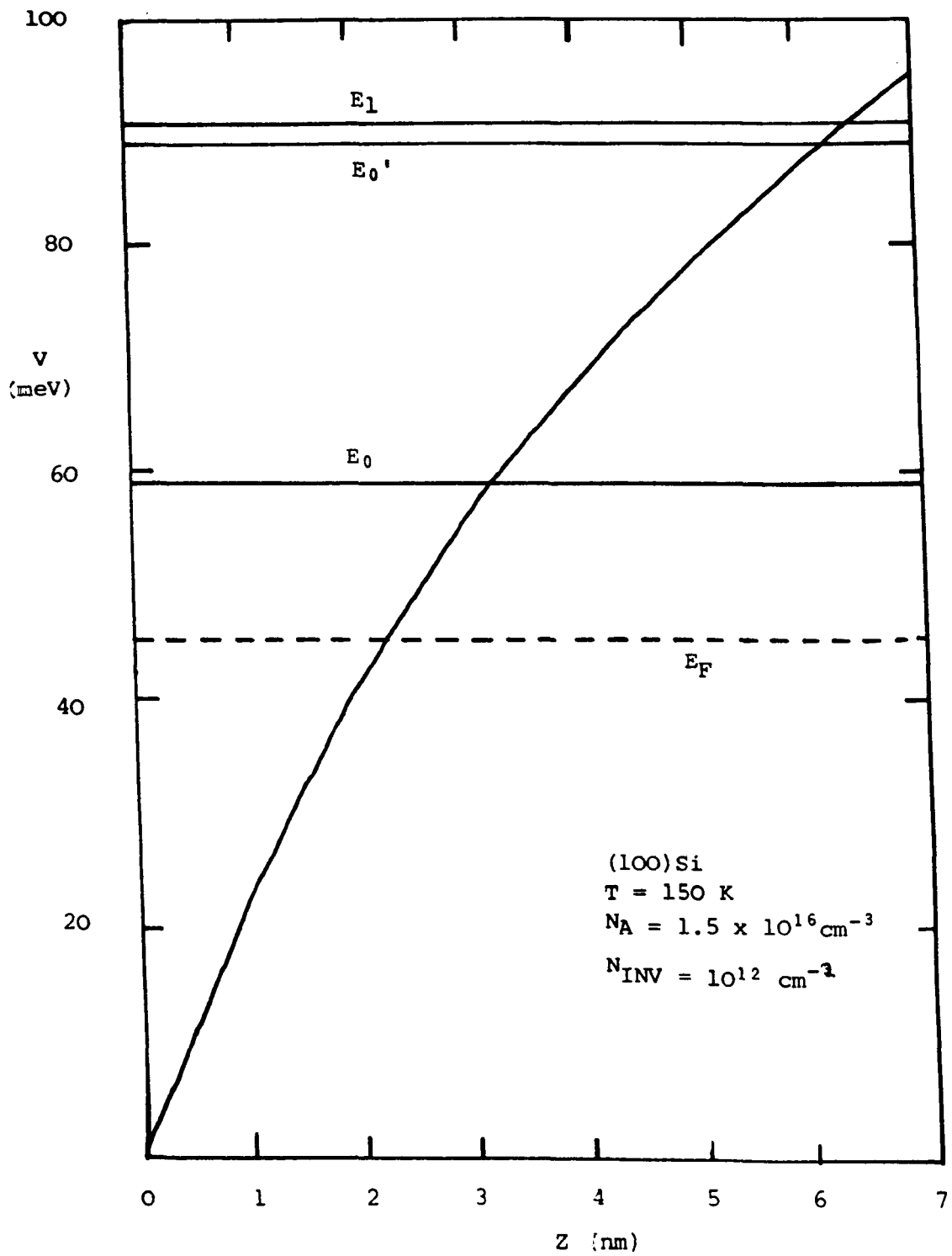


Figure 3.2: Subband Energies and Potential Well Produced by Self-Consistent Calculations (after Stern 1974)

directions is not confined and, hence, we have

$$E = \frac{\hbar^2 k_x^2}{2m_t} + \frac{\hbar^2 k_y^2}{2m_t} + E_i \quad (3.3)$$

where E_i is the energy of the i th sub-band.

For temperatures less than 50 K and carrier densities below $5 \times 10^{12} \text{ cm}^{-2}$ only the lowest sub-band will be occupied and no scattering can occur perpendicular to the interface. Hence, the electrons form a two-dimensional system. This is called the electric quantum limit.

The quantum mechanical treatment for the electrons confined within the inversion layer yields a completely different charge distribution in the well to that given by the classical calculations and this is shown in Figure 3.3. The dashes show the centres of the charge distributions, and it is of note that in the quantum mechanical case the majority of the charge lies well away from the oxide/silicon interface.

3.5 ELECTRICAL TRANSPORT PROPERTIES OF A 2DEG

3.5.1 Introduction

In two-dimensions the electronic density of states (DOS) per unit area per unit energy interval, can easily be shown to be

$$N(E) = \frac{g_s g_v m^*}{2\pi \hbar^2} \quad (3.4)$$

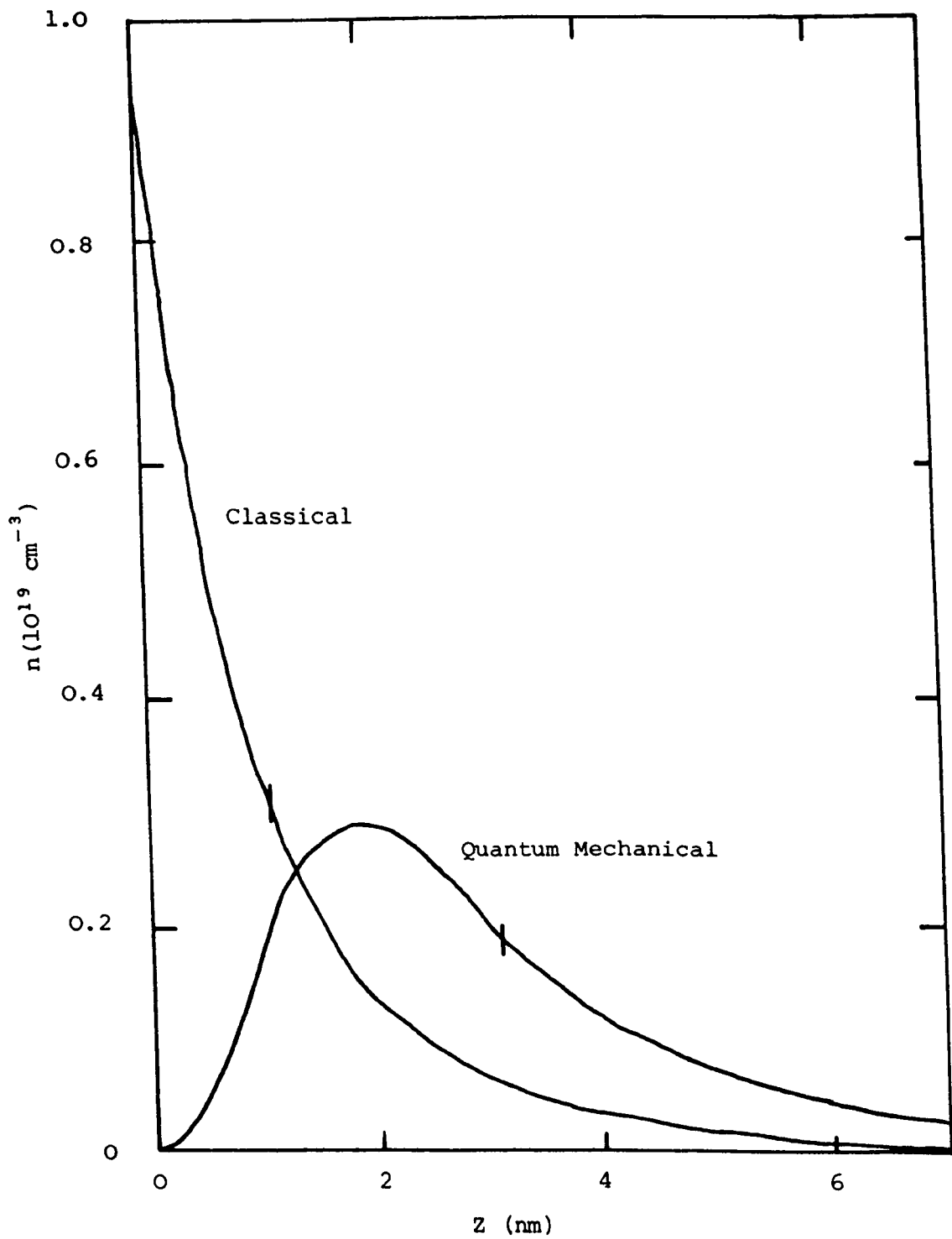


Figure 3.3: Charge Distribution in a Si MOSFET calculated self-consistently (after Stern 1974)

where m^* is the effective mass, g_s and g_v are the spin and valley degeneracies respectively ($g_s = g_v = 2$, and $m^* = m_t$ for (100) silicon in the electric quantum limit). This DOS is independent of energy unlike the three dimensional case where $N(E) \propto E^{\frac{1}{2}}$. However, steps occur at energies where electrons begin to occupy higher sub-bands.

At absolute zero all the states will be filled up to the Fermi level, E_F , so using equation (3.4)

$$E_F = \frac{h^2 n_s}{2\pi m^* g_s g_v} \quad (3.5)$$

The Fermi surface in 2D is a circle of radius, k_F , given by

$$k_F = \left(\frac{4\pi n_s}{g_s g_v} \right)^{\frac{1}{2}} \quad (3.6)$$

From electrostatics, the carrier concentration, n_s is given by

$$n_s = \frac{C_{ox}}{e} (V_g - V_t) \quad (3.7)$$

where C_{ox} is the oxide capacitance per unit area, and V_t is the threshold voltage (V_t is influenced by oxide quality and thickness, and by workfunction differences). We can see, therefore, that by varying the gate voltage we can alter the carrier concentration and, hence, k_F .

The idealised DOS described by equation (3.4) is shown by Figure 3.4(a). A more realistic analysis must consider disorder and this leads to the broadening shown in Figure 3.4(b). The shaded portion, at low energy, indicates the presence of localised states caused by the disorder. These states produce thermally activated behaviour at low carrier concentrations and this is described further in section 3.5.3.

The application of an accelerating electric field, E , causes the Fermi circle described by equation (3.6) to drift at a constant rate given by

$$\frac{\partial k}{\partial t} = - \frac{eE}{\hbar} \quad (3.8)$$

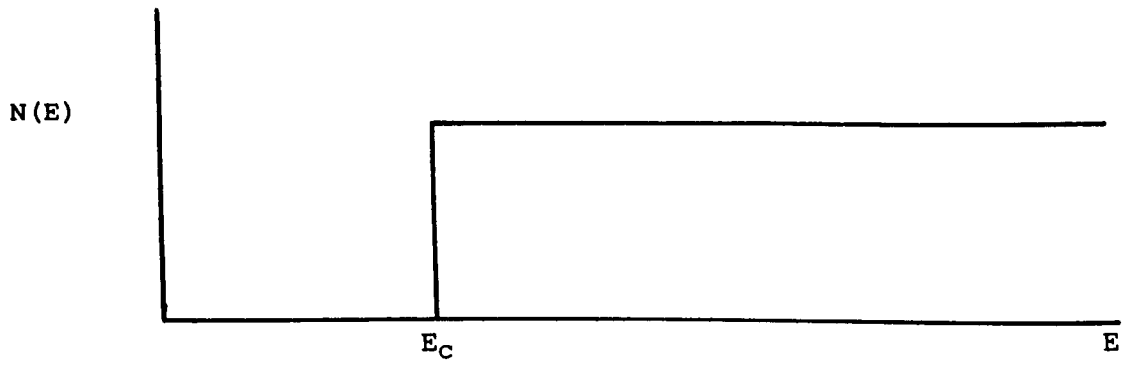
until electron scattering halts this drift. The final displacement of the Fermi circle is

$$\Delta k = - \frac{eE\tau}{\hbar}$$

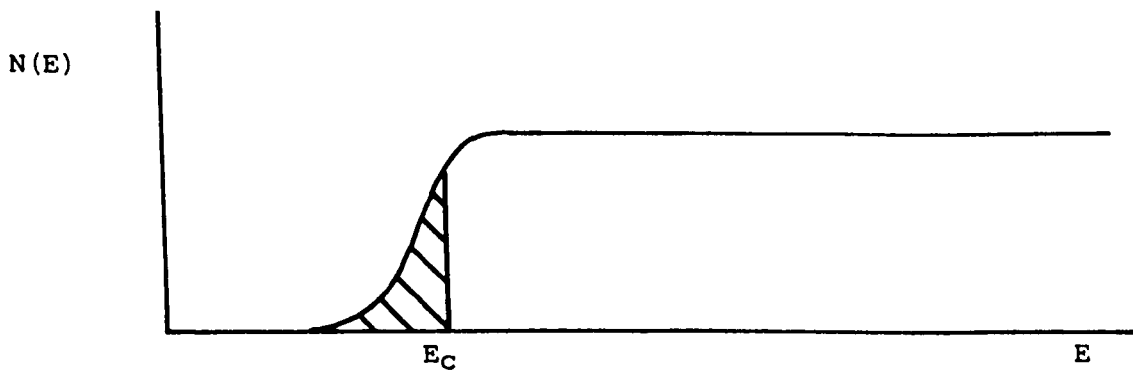
where $\frac{1}{\tau}$ is the total scattering rate.

3.5.2 Scattering Mechanisms

Scattering mechanisms in silicon inversion layers have received a considerable amount of attention. Many mechanisms exist, each having complicated dependencies on temperature, electric



(a) Idealised DOS



(b) DOS including some disorder

Figure 3.4: Schematic Diagram of the Density of States in Two Dimensions

field and carrier concentration. I shall only give a brief outline and comment on the importance of each. For more detail see Ando et al (1982).

Two inelastic scattering mechanisms can occur, electron-electron and electron-phonon, but only the electron-phonon interactions dissipate energy from the electronic system. The electron-electron scattering rate, $1/\tau_{ee}$ is typically of order 10^{11} s^{-1} whereas the electron-phonon scattering rate, $1/\tau_{ep}$, is approximately 10^6 s^{-1} . Therefore, it is valid to consider a characteristic electron temperature T_e .

Figure 3.5 shows, schematically, the major features of the variation of conductivity with carrier concentration, and illustrates the scattering mechanisms. At 300 K the conductivity is limited by phonon scattering. The saturation at high concentrations is due to surface roughness scattering as the gate voltage increases and moves the charge distribution closer to the oxide/silicon interface. With the temperature reduced to 77 K, much of the phonon scattering has been removed leading to higher conductivities and as n_s falls, the conductivity drops to zero at V_t , the threshold voltage. The reduction in the conductivity down to V_t is due to a reduction of the screening of long range Coulomb potentials from trapped charge. Reducing the temperature to 4.2 K appears to remove the phonon scattering.

A typical mobility versus carrier concentration plot is shown in Figure 3.6 for temperatures from 4 K to 1 K. The strong temperature dependence at low n_s arises from two mechanisms: the

Conductivity

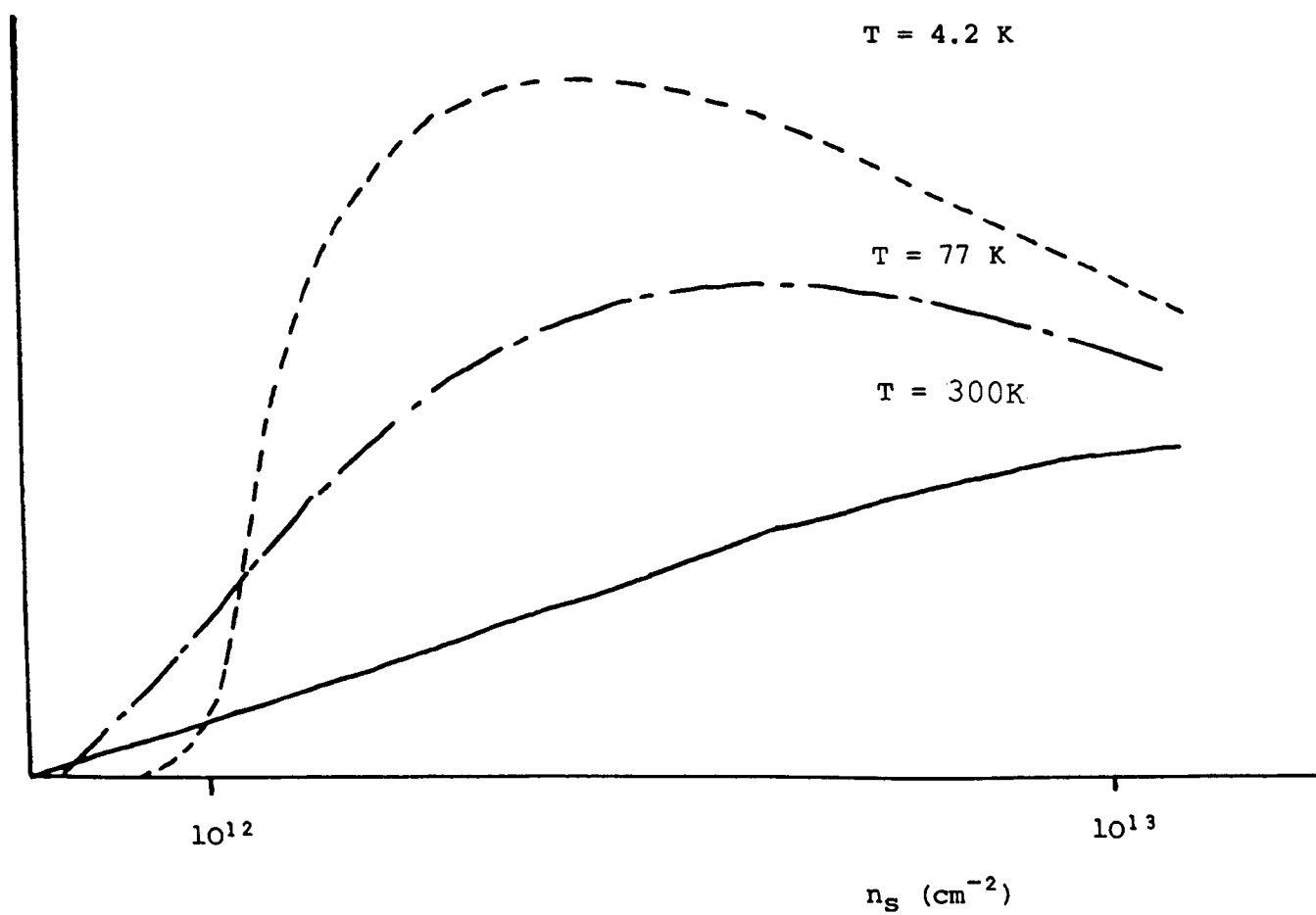


Figure 3.5: Schematic Diagram showing the Variation of Conductivity with Carrier Concentration

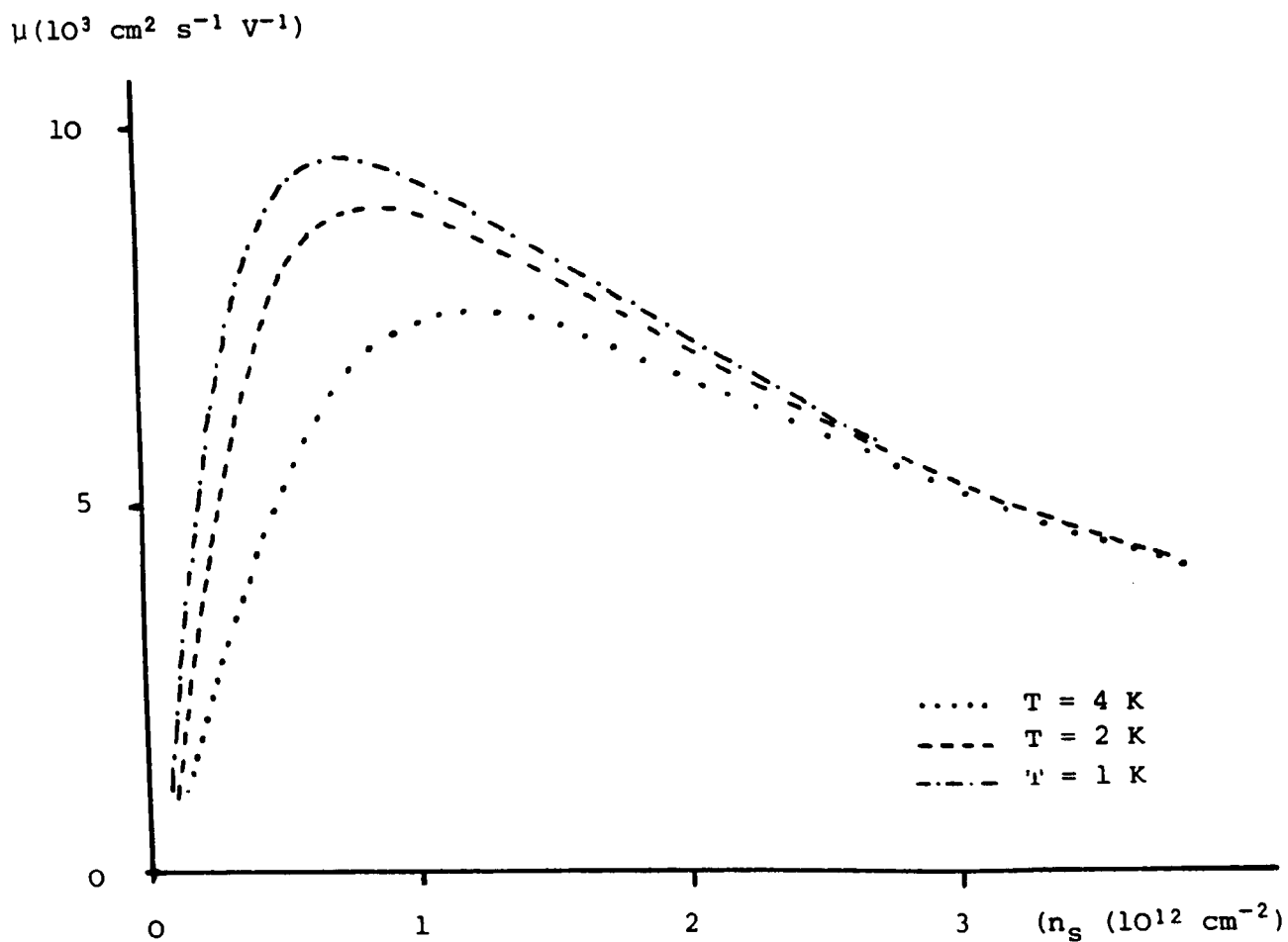


Figure 3.6: Schematic Diagram Showing the Variation of Mobility with Carrier Concentration

temperature dependence of the screening of Coulomb and surface roughness scattering, along with localisation which is discussed in section 3.5.3. The effect of screening has been investigated in high mobility ($\mu > 8000 \text{ cm}^2 \text{ V}^{-1} \text{ s}^{-1}$) silicon MOSFETs (see for example Smith and Stiles, 1985 and references therein) where the Dingle temperature, T_D , which defines the smearing of the Fermi circle due to disorder, is sufficiently low for the effect to become important.

3.5.3 Localisation

Thermal activation at low temperature and low n_S was first reported by Fang and Fowler (1968) and is a special case of Anderson localisation. Anderson (1958) considered a tight binding model consisting of a series of rectangular potential wells of random depth caused by disorder. The random variation in depth is described by a parameter, V_0 , such that the wells vary in depth by $\pm V_0/2$. Anderson showed that for values of V_0/W , where W is the fixed width of the well, less than a critical value, Bloch functions cannot be used to describe the electron wavefunctions and it is necessary to use exponentially decaying wavefunctions. These wavefunctions describe a localised electron. Mott et al (1975), and references therein, extend this argument. They show that for V_0/W greater than the critical value, the normal electronic energy bands consisting of extended states described by Bloch functions, are modified by the disorder. Now, only the central region of the band consists of extended states while the extremities consist of localised states described by exponentially decaying wavefunctions. The energy at which the extended states become localised is called the mobility

edge, and the ability to sweep the Fermi level, E_F , through the mobility edge, E_C , by varying the gate voltage has led to a great deal of work using silicon inversion layers to investigate localisation (see, for example, Pepper 1985 for a review). However, it should be noted that, in silicon inversion layers, strictly the mobility edge divides the strongly localised states from weakly localised states arising from coherent electron scattering.

With E_F below E_C two conduction mechanisms occur in parallel.

- (a) Conduction by electrons thermally excited above E_F into extended states.
- (b) Hopping conduction between localised states due to wave function overlap.

3.6 ELECTRICAL TRANSPORT IN A MAGNETIC FIELD

3.6.1 Introduction

The application of a magnetic field, B , to a 2DEG causes the continuum of energy levels with a constant density of states to split into Landau levels separated in energy by $\hbar\omega_C$, where $\omega_C = eB/m^*$. At absolute zero, if no disorder is present, the density of states of the Landau levels is a set of delta-functions. Disorder broadens these levels into bands and leads to localisation in the extremities of each band.

Sweeping the Fermi level through the Landau levels produces large oscillations in conductance. This is the Shubnikov-de Haas effect (SdH) and was first reported in inversion layers by Fowler et al (1966). A characteristic feature of two dimensional systems is the $1/B$ periodicity of the oscillations at fixed n_s . This is given by

$$\Delta \left(\frac{1}{B} \right) = \frac{g_s g_v e}{h n_s} \quad (3.9)$$

An alternative method is to work at a large fixed magnetic field and to sweep the gate voltage. Now conductance oscillations are seen with period

$$\Delta V_g = \frac{g_s g_v e B}{C_{ox} h} \quad (3.10)$$

3.6.2 A 2DEG in Crossed Electric and Magnetic Fields

Consider a 2DEG confined in the x-y plane with applied magnetic and electric fields, $\underline{B} = B\underline{k}$, and $\underline{E} = E\underline{j}$, where \underline{i} , \underline{j} , \underline{k} are unit vectors in the x, y and z directions respectively. We can write the Hamiltonian for the system (ignoring spin) as

$$H = \frac{1}{2m^*} (\underline{p} + e\underline{A})^2 + eE y \quad (3.11)$$

where \underline{A} is the magnetic vector potential given by

$$\underline{B} = \text{curl } \underline{A} \quad (3.12)$$

If we choose the Landau gauge

$$\underline{A} = B y \underline{i} \quad (3.13)$$

we can rewrite equation (3.11) as

$$H = \frac{1}{2m^*} [(p_y^2 + p_z^2) + (p_x + eBy)^2] + eEy \quad (3.14)$$

The choice of gauge will affect the resulting eigenfunctions but not the eigenvalues. The antisymmetric gauge in equation (3.13) is reasonable as the axes are unique due to the application of \underline{B} and \underline{E} .

Using the Schrodinger equation

$$H\Psi = \epsilon\Psi \quad (3.15)$$

we can substitute

$$p_x = -i\hbar \frac{\partial}{\partial x}, \quad p_y = -i\hbar \frac{\partial}{\partial y}, \quad p_z = -i\hbar \frac{\partial}{\partial z} \quad (3.16)$$

yielding

$$-\frac{\hbar^2}{2m^*} \left[\frac{\partial^2 \Psi}{\partial y^2} + \frac{\partial^2 \Psi}{\partial z^2} \right] + \frac{1}{2m^*} \left(-i\hbar \frac{\partial}{\partial x} + eBy \right)^2 \Psi + eEy\Psi = \epsilon\Psi \quad (3.17)$$

The electronic wavefunction, Ψ , consists of components for the x, y and z directions. In the z-direction the electron is described by a bound state wave function

$$\Psi_0(z) = \left(\frac{a^3}{2}\right)^{\frac{1}{2}} z e^{-az/2} \quad (3.18)$$

Here, a , is a quantity related to the average distance from the Si-SiO₂ interface, Z_0 , by $Z_0 = 3/a$. Hence, a suitable wavefunction for the problem is

$$\Psi = U(y) e^{ik_x x} \Psi_0(z) \quad (3.19)$$

We can substitute this into equation (3.17) along with the substitutions

$$V_d = \frac{E}{B}, \quad \omega_c = \frac{eB}{m^*}, \quad E_1 = -\frac{\hbar^2}{2m^*} \frac{\partial^2}{\partial z^2} \quad (3.20)$$

and

$$y' = y - Y_0 = y + \frac{\hbar k_x}{m^* \omega_c} + \frac{m^* E}{eB^2} \quad (3.21)$$

and obtain after some manipulation

$$H = \frac{1}{2m^*} \left(\underbrace{\hbar^2 \frac{\partial^2}{\partial y'^2}}_I + m^* \omega_c^2 y'^2 \right) + \underbrace{E_1}_{II} + \underbrace{eEY_0}_{III} + \frac{1}{2} m^* V_d^2 \quad (3.22) \quad \underbrace{\hspace{1.5cm}}_{IV}$$

Let us consider each of the terms in equation (3.22). Term I describes a simple harmonic oscillator centred at $y = Y_0$. Term II is a constant in the electric quantum limit. Term III is the potential energy at the orbit centre determined by the applied electric field. Term IV describes the kinetic energy of the motion in the x-direction.

We can now write down the eigenfunctions as

$$\Psi_n = C e^{ik_x x} U_n(y - Y_0) \Psi_0(z) \quad (3.23)$$

and the eigenvalues as

$$E_n = \left(n + \frac{1}{2}\right) \hbar\omega_c + E_1 + eEY_0 + \frac{1}{2} m^*V_d^2 \quad (3.24)$$

Where $n = 0, 1, 2, 3, \dots$, C is the normalising constant and $U_n(y - Y_0)$ are simple harmonic oscillator eigenfunctions.

Equations (3.22) and (3.24) indicate the effect of the applied magnetic field. The electron energy is quantised into discrete Landau levels with the energy determined by a given n and the energy separation of the levels being $\hbar\omega_c$. In the x -direction the electrons drift at a velocity V_d , but in the y -direction the electrons are bound to orbit centres by the harmonic oscillator potential. The potential energy of the orbit centres varies in the y -direction due to the applied electric field. The separation of the orbit centres, ΔY_0 , is determined by applying travelling wave boundary conditions in the x -direction. For a 2DEG of sides L_x, L_y we have

$$k_x = 0, \pm \frac{2\pi}{L_x}, \pm \frac{4\pi}{L_x}, \dots$$

and so

$$\Delta Y_0 = \frac{\hbar\Delta k_x}{eB} \quad (3.25)$$

Hence, substituting $l_B = (\hbar/eB)^{\frac{1}{2}}$, we obtain

$$\Delta Y_0 = \frac{2\pi l_B^2}{L_x} \quad (3.26)$$

The number of orbit centres in the 2DEG is thus

$$\frac{L_y}{\Delta Y_0} = L_x L_y \frac{eB}{h} \quad (3.27)$$

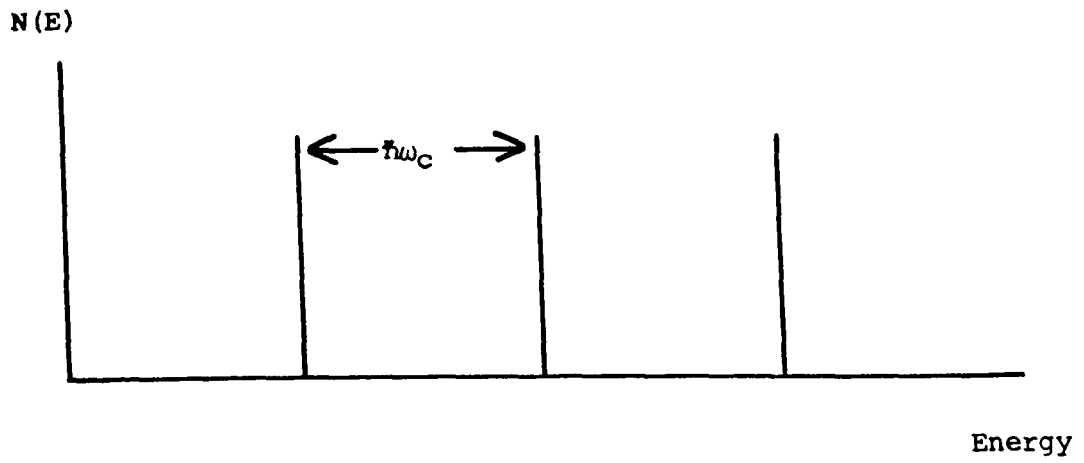
and the number of states per unit area, per unit Landau level (neglecting spin) is

$$g = \frac{eB}{h} \quad (3.28)$$

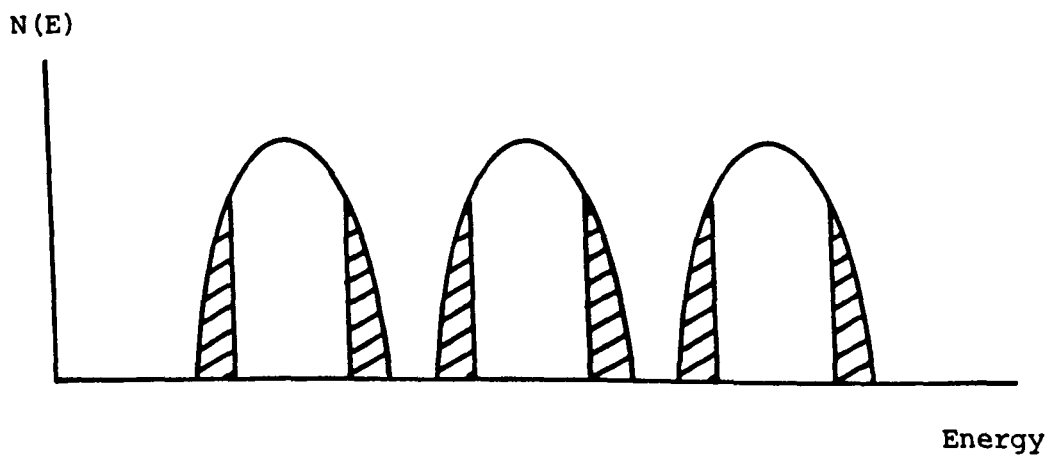
The argument presented above assumes no disorder or scattering and as a result produces a set of delta function Landau levels. This is shown in Figure 3.7(a). A consequence of this assumption is that no current can flow in the y-direction as the electrons are bound to the orbit centres. A more realistic treatment including disorder produces broadened Landau levels and these are shown in Figure 3.7(b). A current can now flow in the y-direction as electrons can scatter between adjacent orbits of the same energy. Another feature introduced by the disorder is localisation of the states in the band tails. This arises by the same argument as in the zero field case discussed in section 3.5.3.

3.6.3 The Quantum Hall Effect

Von Klitzing et al (1980) found that with high quality silicon inversion layers at low temperatures and high magnetic fields, the Hall resistance, R_H , has plateaux when the Fermi level



(a) Delta Function Landau Levels



(b) Landau Levels with some Disorder

Figure 3.7: Schematic Diagram of the Landau Levels

lies in the mobility gap between Landau levels. Furthermore, the measured value of R_H obtained with E_F just above the i^{th} Landau level is

$$R_H = \frac{h}{i e^2} \quad (3.29)$$

This can readily be understood in the case of no scattering and, hence, delta-function Landau levels, with E_F corresponding to i totally filled levels, as the current in the x-direction is given by

$$J_x = - neV_y = \frac{i e^2 E_y}{h} \quad (3.30)$$

Since the Hall resistance is defined as E_y/J_x , we obtain

$$R_H = \frac{h}{i e^2} \quad (3.31)$$

This is the required result but clearly we do not have this ideal situation since disorder and the low but finite temperature ($k_B T_e < \hbar \omega_c$) will broaden the Landau levels and produce localised band tails. Consider the situation of E_F at the centre of a Landau level. Empty, extended states exist within $k_B T_e$ of E_F and so normal scattering can occur. This allows a current to flow in the y-direction and power to be dissipated in the bulk of the sample as $\underline{J} \cdot \underline{E} \neq 0$. With E_F between Landau levels only localised electron states exist within $k_B T_e$ of E_F . Now, scattering of electrons in extended states is not possible so no current can flow in the y-direction, $\underline{J} \cdot \underline{E} = 0$, and we have dissipationless conduction within

the bulk of the sample with the resistivity in the x direction, ρ_{xx} , equal to zero.

Experimentally the measured values of R_H agree with those predicted to 1 part in 10^7 . To understand this accuracy Laughlin (1981) proposed the thought experiment shown in Figure 3.8. Here the conducting 2DEG is bent into a conducting ring with the Hall voltage measured across its edges. The magnetic field, B , is normal to the 2DEG around the ring, while an additional magnetic flux, ϕ_0 , threads through the loop. The application of this additional magnetic field induces a current to flow around the ring which is given by Faraday's law of induction (assuming no energy loss from the system) as

$$I = \frac{\partial U}{\partial \phi_0} \quad (3.32)$$

where U is the internal energy of the system. We can rewrite this for small changes as

$$I = \frac{\Delta U}{\Delta \phi_0} \quad (3.33)$$

where $\Delta \phi_0 = h/e$, the flux quantum.

For no disorder the effect of threading an extra flux quantum through the ring can be seen from equation (3.21) to move each eigenstate in the y-direction until they map exactly into each other. Thus, one state is transferred from one edge of the ring to the other. We can calculate the current by considering the number

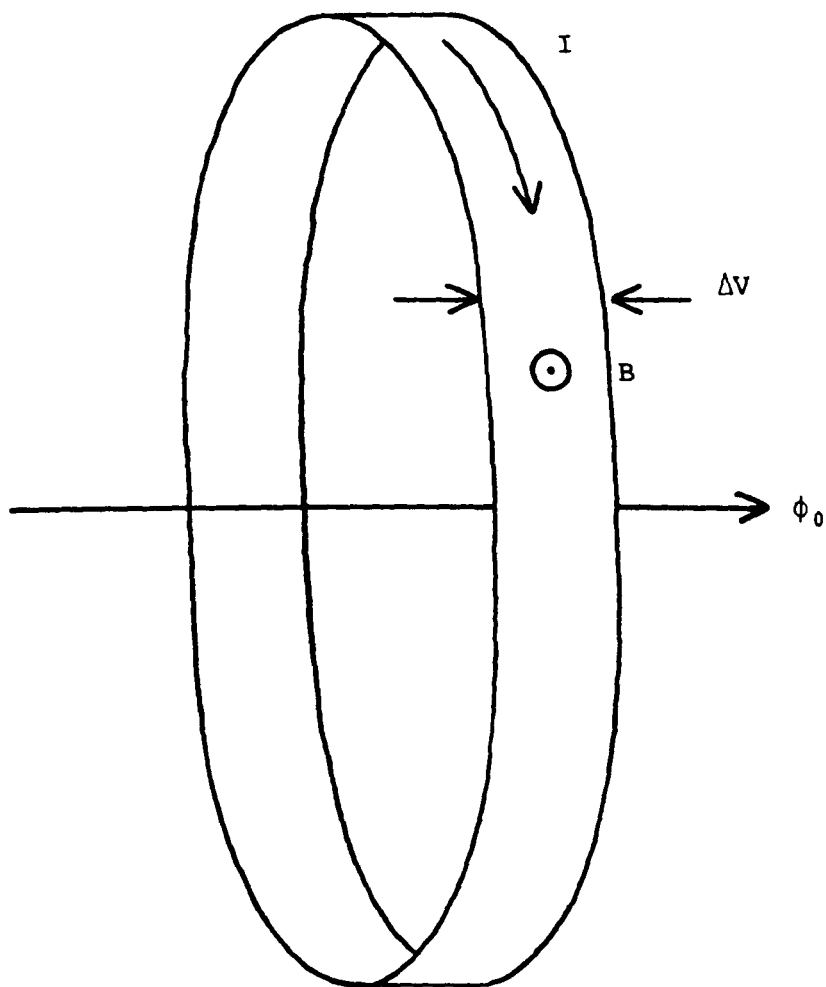


Figure 3.8: Laughlin's Thought Experiment

of electrons transferred and the energy gained by each. Hence, for E_x just above the i th Landau level

$$I = \frac{(i)(e V_H)}{h/e} = \frac{(i) e^2 V_H}{h} \quad (3.34)$$

This is for the ideal system. However, the presence of localised states will not change this argument as the effect of changing the flux threading the ring on these states is just to map them into themselves in some complicated manner. Hence, as the change in flux is adiabatic, and localised and extended states cannot exist at the same energy, the only mechanism involved is the transfer of charge as in the ideal case.

3.6.4 The Current Distribution in the Quantum Hall Effect

In the QHE with E_F between Landau levels we have dissipationless conduction and so no electric field can exist in the x -direction. However, we have the Hall voltage across the sample and since the source and drain contacts are good conductors there is considerable distortion in the resulting equipotentials and, hence, the current distribution near the ends of the sample. This is shown in Figure 3.9. Away from the source and drain contacts the current will run along the equipotentials with $J \cdot E = 0$ and, hence, dissipationless conduction. At the source and drain contacts $J \cdot E \neq 0$ and dissipation will occur. In these regions the QHE has broken down. Increasing the current will increase the size of these regions until they include the entire sample completely destroying the QHE.

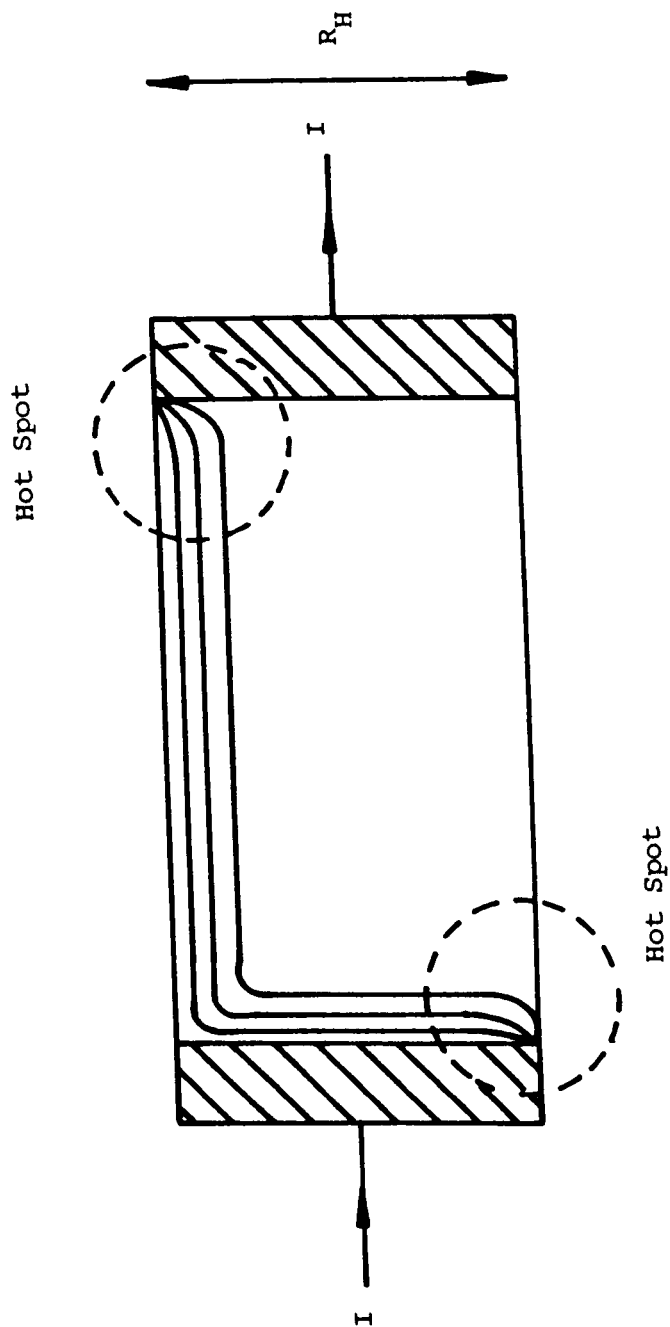


Figure 3.9: Schematic Diagram Showing Some of the Current Paths in the Quantum Hall Regime

It can be seen in Figure 3.9 that the corner regions have very high electric field gradients. These produce hot electrons no longer in thermal equilibrium with the lattice. Von Klitzing et al (1985) has detected far infra red (FIR) emission from a sample in the QHE and shown that it can no longer be detected with the corner regions covered. Another consequence of the very large electric field gradient is to allow scattering between SHO states of different energy due to wave function overlap. Eaves and Sheard (1986) showed that this quasi-elastic inter Landau level scattering (QUILLS) mechanism explained the results of Bliok et al (1986) who measured the breakdown of the QHE in samples with small constrictions.

CHAPTER 4Theory of Phonon Emission from a Heated 2DEG4.1 INTRODUCTION

The theory presented here follows closely that of Toombs et al (1987) and Challis et al (1987) for phonon emission. The effect of phonon scattering and phonon focussing on the predicted phonon emission, arising from this theoretical treatment, will then be discussed, and previous theoretical and experimental work reviewed.

4.1.1 The Electron-Phonon Interaction

The passage of an acoustic phonon through the lattice immediately surrounding a 2DEG affects the energy of the electrons in the 2DEG by adding a slowly varying potential to the periodic potential of the lattice. Bardeen and Shockley (1950) showed that as the change in potential, over one atomic spacing is small, the problem can be treated by considering the motion of the electrons in the slowly varying potential alone, with the effect of the lattice taken into account by using an effective mass. Herring and Vogt (1956) extended this deformation potential model to cover many-valley semiconductors, and wrote the potential felt by the electrons as

$$V_{ep}(\underline{r}) = \bar{m}_d \nabla \cdot \underline{u} + \bar{m}_u \frac{\partial u_z}{\partial z} \quad (4.1)$$

here Ξ_d and Ξ_u are the deformation potential constants. The displacement, $\underline{u}(\underline{r})$, of the silicon lattice due to the passage of a phonon can be expressed as

$$\underline{u}(\underline{r}) = \left(\frac{\hbar}{2\rho V \omega_{qs}} \right)^{\frac{1}{2}} (a_{qs} e^{i\mathbf{q}\cdot\mathbf{r}} + a_{qs}^{\dagger} e^{-i\mathbf{q}\cdot\mathbf{r}}) \underline{\epsilon}_{qs} \quad (4.2)$$

where ρ is the density, ω_{qs} is the angular frequency of a phonon of wavevector \underline{q} in mode s , V is the crystal volume, a_{qs} and a_{qs}^{\dagger} are the creation and annihilation operators and $\underline{\epsilon}_{qs}$ is the polarisation vector.

We can now write the Hamiltonian for phonon emission as

$$V_{ep}(\underline{r}) = -i \left(\frac{\hbar}{2\rho V \omega_{qs}} \right)^{\frac{1}{2}} \Xi_u (q_z \epsilon_{qs,z} - D \underline{q} \cdot \underline{\epsilon}_{qs}) a_{qs}^{\dagger} e^{-i\mathbf{q}\cdot\mathbf{r}} \quad (4.3)$$

where $D = -\Xi_d/\Xi_u$.

Introducing $\chi_s^{\frac{1}{2}}(\theta) = (q_z \epsilon_{qs,z} - D \underline{q} \cdot \underline{\epsilon}_{qs})/q$, we can choose to align the polarisation of the two transverse acoustic (TA) modes either within or perpendicular, to the plane defined by \underline{q} and the z -axis. This allows us to simplify $\chi_s(\theta)$ for the longitudinal acoustic (LA) and TA modes, giving

$$\begin{aligned} \chi_L^{\frac{1}{2}}(\theta) &= \cos^2\theta - D && \text{LA} \\ \chi_T^{\frac{1}{2}}(\theta) &= \sin\theta \cos\theta && \text{TA (in plane)} \\ \chi_T^{\frac{1}{2}}(\theta) &= 0 && \text{TA (out of plane)} \end{aligned}$$

where θ is the angle between \underline{q} and the normal to the plane of the 2DEG.

Now equation (4.3) can be written as

$$V_{ep}(\underline{r}) = -i \left(\frac{\hbar}{2\rho V v_s^2} \right)^{\frac{1}{2}} \equiv_u \chi_s^{\frac{1}{2}}(\theta) a_{qs}^+ \quad (4.4)$$

where v_s is the velocity of sound in mode s .

The emitted phonon power, P , is

$$P = \sum_{qs} \hbar \omega_{qs} \frac{\partial n_{qs}}{\partial t} \quad (4.5)$$

where n_{qs} is the Bose-Einstein function for the number of phonons with wavevector q in a mode s . Considering an electronic transition $\underline{k} \rightarrow \underline{k}'$, with the emission of a phonon q , we can use Fermi's Golden rule to write the transition rate as

$$\frac{\partial n_{qs}}{\partial t} = g_s g_v \sum_{kk'} f_k (1 - f_{k'}) (n_{qs} + 1) \quad k'qs \quad (4.6)$$

$$\text{with } W_{\underline{k}}^{\underline{k}'qs} = \frac{2\pi}{\hbar} |M_{\underline{k}}^{\underline{k}'qs}|^2 \delta(E_{\underline{k}} - E_{\underline{k}'} - \hbar\omega_{qs}) \quad (4.7)$$

$$\text{and } M_{\underline{k}}^{\underline{k}'qs} = \langle \underline{k}' | v_{ep} | \underline{k} \rangle$$

$f_{\underline{k}}$ and $f_{\underline{k}'}$ are the Fermi-Dirac distribution functions, and we have assumed a well defined electron temperature, T_e .

Assuming free electron motion in the plane of the 2DEG, and using the bound state wavefunction defined in equation (3.18) for motion in the z-direction, we can write the electronic wavefunctions as

$$\Psi(\underline{r}) = (L_x L_y)^{-\frac{1}{2}} e^{ik_x x} e^{iky y} \Psi_0(z) \quad (4.8)$$

The matrix elements, $M_{\underline{k}}^{\underline{k}'qs}$, are the product of three integrals. Those over x and y and, hence, in the plane of the 2DEG, require the conservation of wave vector in the plane, i.e. $\underline{k} = \underline{k}' + \underline{q}_{\parallel}$ (where $q_{\parallel} = q \sin\theta$, and θ is the angle between \underline{q} and the normal to the 2DEG) while that over z gives

$$F(q_z) = \int_0^{\infty} \Psi_0^2(z) e^{-iq_z z} dz$$

This is the Fourier transform of the bound state, $\Psi_0(z)$, and so

$$|F(q_z)|^2 = (1 + q_z^2 a^2)^{-3} \quad (4.9)$$

Equation (4.9) shows that a cut-off exists limiting the

maximum q_z to $q_z - 1/a$, in line with the Uncertainty Principle. As discussed in section 3.4, the width of the 2DEG requires extensive self-consistent calculations to determine, and as it dependent on the substrate doping and carrier concentration, the q_z cut-off will also be dependent on these parameters.

In the plane of the 2DEG, conservation of momentum gives

$$k'^2 = k^2 + q_{\parallel}^2 - 2kq_{\parallel}\cos\phi \quad (4.10)$$

where ϕ is the angle between q_{\parallel} and k' . Energy conservation requires $E_k - E_{k'} - \hbar\omega_q = 0$, and these two conditions can only be satisfied for

$$q_{\parallel} \leq 2k_F - \frac{2m^*v_s}{\hbar \sin\theta} \quad (4.11)$$

Thus, except for very small θ , we have

$$q_{\parallel} \leq 2k_F \quad (4.12)$$

This is the so called $2k_F$ cut-off, and is interesting experimentally as k_F can be controlled by simply adjusting the gate voltage, V_g , in silicon MOSFET samples.

After some manipulation we can now write an expression giving the power emitted per unit area into phonons in the frequency range $\omega \rightarrow \omega + d\omega$, in a solid angle $d\Omega$ as

$$P = \frac{m^* g_V \Xi^2}{8\pi^2 \rho \hbar v_S^3} \cdot \frac{\chi_S(\theta) |F(q_z)|^2 \omega^3}{\sin\theta} \int_{k_0}^{\infty} \frac{f_k (1 - f'_k) k \, dk}{(k^2 - k_0^2)^{\frac{1}{2}}} \quad (4.13)$$

where $k_0 = \frac{q_{\parallel}}{2} + \frac{m^* v_S}{\hbar \sin \theta}$

To proceed further it is necessary either to make approximations to simplify equation (4.13), or to evaluate it numerically.

4.1.2 Emission in a Quantising Magnetic Field

The application of a quantising magnetic field prohibits the use of the eigenfunctions in equation (4.8). Instead it is necessary to use those in equation (3.19) where

$$\psi_n = L_x^{-\frac{1}{2}} U_n(y - Y_0) e^{ik_x x} \psi_0(z)$$

The method for determining the phonon emission using these eigenfunctions is essentially the same as for zero magnetic field (section 4.1.1). The transitions involved, however, are between Landau levels, so instead of scattering described by

$$k \rightarrow k' + q$$

we have

$$\lambda \rightarrow \lambda' + q$$

where λ represents the quantum number pair n, k_x . The matrix elements for these transitions are

$$\begin{aligned}
 M_{\lambda}^{\lambda', qs} &= \langle \lambda' | V_{ep} | \lambda \rangle \\
 &= \left(\frac{\hbar}{2\rho V \omega_{qs}} \right)^{\frac{1}{2}} \Xi_u i(q_z \epsilon_{qs, z} - D \underline{q} \cdot \underline{\epsilon}_{qs}) \int \psi_{\lambda'}^* e^{-iqr} \psi_{\lambda} d^3r
 \end{aligned}
 \tag{4.14}$$

Considering the matrix element integrals, it is apparent that those over x and z are unchanged, producing conservation of momentum in the x -direction, and the bound state form factor (equation (4.9)) respectively. The integral over y is

$$\int_{-Ly/2}^{Ly/2} U_n'(y - Y_{k_x'}) e^{-iqyY_0} \cdot U_n(y - Y_{k_x}) dy
 \tag{4.15}$$

As the SHO states are localised the integration limits can be extended to $\pm \infty$. The separation of the orbit centres is

$$Y_{k_x'} - Y_{k_x} = \ell_B^2 (k_x - k_x') = \ell_B^2 q_x
 \tag{4.16}$$

and by moving the origin to the orbit centre Y_{k_x} , we can rewrite equation (4.15) as

$$I_{nn'}(q_x, q_y) = \int_{-\infty}^{\infty} U_n'(y) e^{-qyY_0} U_n(y + \ell_B^2 q_x) dy
 \tag{4.17}$$

This integral can be evaluated using the generating function for Hermite polynomials.

The final form for the matrix elements is

$$|M_{\lambda}^{\lambda',qs}|^2 = \left(\frac{\hbar}{2\rho V\omega_{qs}}\right) \equiv_u^2 q^2 \chi_s(\theta) |I_{nn'}(q_x, q_y)|^2 |F(q_z)|^2 \delta_{k_y, k_y+q_y} \quad (4.18)$$

and now we can write down the net power emitted into a phonon mode q, s as

$$P = \sum_{\lambda, \lambda'} \hbar\omega_{qs} \left\{ \frac{e^{\hbar\omega_{qs}/k_B T} - e^{-\hbar\omega_{qs}/k_B T}}{e^{\hbar\omega_{qs}/k_B T} - 1} \right\} \cdot f_n^0 (1 - f_{n'}^0) W_{\lambda}^{\lambda',qs} \quad (4.19)$$

with

$$W_{\lambda}^{\lambda',qs} = \frac{2\pi}{\hbar} |M_{\lambda}^{\lambda',qs}|^2 \delta(E_n - E_{n'} - \hbar\omega_{qs}) \quad (4.20)$$

For $T_e \gg T$ the factor $\{\}$ is of order unity and we obtain

$$P(\omega_{qs}, \theta) = \frac{g_s g_v \equiv_u^2 \omega_{qs}^4 \chi_s(\theta)}{16\pi^3 \ell_B^3 \rho v_s^5} |I_{nn'}(q_x, q_y)|^2 |F(q_z)|^2 f_n^0 (1 - f_{n'}^0) \quad (4.21)$$

where $P(\omega_{qs}, \theta)$ is the power emitted per unit area, per unit solid angle into modes $\omega_{qs} = (n - n')\omega_c$, at an angle θ to the normal to the 2DEG.

4.1.3 Discussion of the Main Theoretical Results

The theoretical treatment in zero magnetic field produces two main features. Conservation of momentum in the plane of the 2DEG leads to the $2k_F$ cut-off, while the function $|F(q_z)|^2$ limits the phonon momentum that can be emitted normal to the 2DEG. Both of these mechanisms will act together to limit the maximum phonon momentum that can be emitted, and make the cooling of the warm or

hot electrons inefficient if the peak of the electron energy distribution ($\sim 3.8 k_B T_e$) is above this combined cut-off.

The $2k_F$ cut-off will confine the emitted phonons to a cone of half angle θ . It is apparent from equations (3.5) and (3.6) that by varying the gate voltage, V_g , we can alter this cone of emission. For large V_g , the $2k_F$ cut-off will have little effect and the phonons will be emitted in all directions. Reducing V_g will limit the emission of phonons to a cone of reducing half angle θ , and for very low V_g , the phonons will be emitted almost normal to the 2DEG. Limiting the channels available to dissipate energy in this way will raise the temperature of the electronic system. If the $F(q_z)$ cut-off is unimportant, this rise in electron temperature will cause the average energy of the emitted phonons to rise. If the $F(q_z)$ is limiting q , however, the number of lower energy phonons will have to increase to allow the electronic system to dissipate the same amount of energy. A complication is that the $F(q_z)$ cut-off is also dependent on V_g due to the self-consistent nature of the confining potential in the z -direction. For low V_g the electrons are not tightly confined, and so the $F(q_z)$ cut-off is a more important restriction on the emission of the phonons.

The application of a quantising magnetic field leaves the $F(q_z)$ cut-off unchanged. The $2k_F$ cut-off, however, is replaced by restrictions imposed by the SHO overlap term $I_{nn'}(q_x, q_y)$. This term is a function of the general form

$$|I_{nn'}(q_x, q_y)|^2 \sim (\xi^2)^{n-n'}. \text{ (polynomial in } \xi^2 \text{ of degree } n). e^{-\xi^2/2}$$

(4.22)

where $\xi = ql_B \sin\theta$.

This has a maximum for $\xi^2 = 2(n - n')$ and, thus, gives

$$\sin\theta = \frac{\sqrt{2(n - n')}}{ql_B} \quad (4.23)$$

If we assume that the dominant phonons are arising from $n = 1 \rightarrow n' = 0$ transitions, for a phonon in modes $q = \omega_C/v_S = eB/m^*v_S$, and we obtain $\sin\theta \propto B^{-\frac{1}{2}}$. In addition, $|I_{nn'}|^2 = 0$ for $\xi = 0$, and so the emitted phonons are confined to a cone shaped shell which becomes progressively tighter as B is increased. The mean emission angle, θ_m , is given roughly by $\sin\theta_m = \sqrt{2}/q l_B$, yielding

$$\sin\theta_m = m^*v_S / \left(\frac{1}{2} eBh\right)^{\frac{1}{2}}$$

This is an approximate treatment as the maximum in $P(\omega_{qs}, \theta)$ is also affected by $\chi_S(\theta)$ and, $|F(q_z)|^2$.

The transition from the zero magnetic field situation to the magnetic field situation can be understood by considering low magnetic fields. For a reasonable n_S we are populating many Landau levels so n and n' are large. With $k_B T_e \ll E_F$ all the transitions take place close to the Fermi level, and $n \approx n' \approx \bar{n}$, where \bar{n} is the mean number of filled levels giving $E_n = (\bar{n} + \frac{1}{2})\hbar\omega_C$. Classically the amplitude of motion for a SHO, A_n , is given by $A_n = (2n + 1)^{\frac{1}{2}} l_B$.

and we can see $I_{nn'} = 0$ if twice this amplitude is less than the separation of the orbit centres, ie $2A_n \leq \ell_B q_x$. This produces the condition $q_y \leq 2k_F$ which generalises to $q_{\parallel} \leq 2k_F$ if q_x is non-zero.

The theoretical results presented here include certain assumptions to simplify the problem. These are:

- (1) $T_e \gg T$ and so phonon absorption by the electron gas can be neglected.
- (2) The 2DEG is situated within a bulk silicon lattice when in fact it is very close to the oxide/silicon interface.
- (3) The only transitions in the magnetic field case are inter Landau level transitions.
- (4) Phonon focussing is not present.
- (5) The deformation potentials are not screened by the electrons in the 2DEG and are, thus, independent of n_s .

These assumptions will be discussed further in Chapter 6. However, even with these simplifications the complexity of the expressions obtained means that they can only be evaluated numerically. Further complications arise when phonon focussing is included in the theory.

4.2 PHONON SCATTERING IN Si(B)

4.2.1 Introduction to Phonon Scattering

Heat transport in non-metallic crystals is predominantly due to crystal lattice vibrations. The energy of these vibrations is quantised and the quanta are termed phonons. The heat current carried by phonons is the product of the number of phonons in that mode, the energy carried by each phonon and the group velocity, \underline{V}_s . The total heat current is, thus

$$\underline{h} = \sum_{q,s} n_{qs} \hbar \omega_{qs} \underline{V}_{qs} \quad (4.25)$$

In thermal equilibrium $n_{qs} = n_{-qs}$ and \underline{h} is zero. The application of a temperature gradient to the sample causes n_{qs} to depart from its equilibrium distribution giving a net heat current. The departure of n_{qs} from equilibrium is opposed by scattering processes which limit \underline{h} . To solve the Boltzmann equation, Klemens (1955) and Callaway (1959) used the relaxation time approximation which assumes that scattering processes restore the phonon distribution to the equilibrium distribution at a rate proportional to the departure of the distribution from equilibrium. In this approximation the scattering times, which are functions of frequency and temperature, are characterised by relaxation times, τ_1 . The total scattering rate, τ_t^{-1} , is obtained by assuming the individual scattering rates,

ie

$$\tau_t^{-1} = \sum_j \tau_j^{-1} \quad (4.26)$$

Assuming a linear dispersion relation (the Debye model) of the form

$$\omega_{qs} = v_s q \quad (4.27)$$

it can be shown that the phonon density of states is proportional to ω^2 . Using these assumptions Klemens calculated the thermal conductivity of a non-metallic crystal as

$$K(T) = \frac{k_B^4 T^3}{2\pi^2 \bar{v} \hbar^3} \int_0^{\theta/T} \frac{x^4 e^x}{(e^x - 1)^2} \tau_t dx \quad (4.28)$$

Here \bar{v} is the phonon velocity averaged over all modes, $x = \hbar\omega/k_B T$ and θ is the Debye temperature.

4.2.2 Scattering Mechanisms

To evaluate equation (4.28) it is necessary to consider the individual scattering mechanisms present. These fall into two types: Intrinsic processes, which are a property of the pure crystal, and extrinsic processes, which arise from impurities both naturally occurring in, and deliberately added to, the crystal.

4.2.2a Intrinsic Processes

At low temperatures the dominant process limiting the phonon mean free path is boundary scattering. Casimir (1938) calculated

the boundary scattering rate, τ_B^{-1} , to be

$$\tau_B^{-1} = \bar{V}/L_C \quad (4.29)$$

where L_C is the Casimir length. For an infinitely long rod of circular cross-section, L_C is simply the diameter, but for a rectangular cross-sectioned bar of sides l_1 , l_2 , it is given by

$$L_C = \frac{2}{\sqrt{\pi}} (l_1 \times l_2)^{\frac{1}{2}} \quad (4.30)$$

Casimir assumed that the scattering was perfectly diffuse, and the surfaces act as perfect black-bodies. Berman et al (1953) extended this treatment to include finite sample length and specular reflection in their sample.

Point defect scattering of phonons arises from a difference in mass, volume or interatomic binding forces in the vicinity of a defect. Klemens (1955) showed that for phonon wavelengths large in comparison to the defect size, the scattering involved is Rayleigh scattering. This gives a scattering rate

$$\tau_I^{-1} = A\omega^4 \quad (4.31)$$

A is a constant determined by the type of the defect involved. Uncertainty about the exact nature of the defects means that calculations can only be performed for isotopes of the host lattice. This is termed isotope scattering, and is generally only important

for high frequency phonons.

Phonon-phonon scattering is another intrinsic process arising from non-linear binding forces between atoms. However, in the temperature range 1 K - 4 K this process can be neglected.

4.2.2b Extrinsic Processes

Extrinsic processes arise from the presence of impurities in the host lattice and fall into two categories, direct and Raman. The mechanism by which they occur is the modulation of the electrostatic potential at the impurity site by the passage of a phonon through the neighbouring lattice.

The direct process is a one phonon process with a phonon, q , causing a transition between two states $|a\rangle$ and $|b\rangle$. After the spin-spin relaxation time, the system de-excites by emitting a virtual photon. This is shown in Figure 4.1.

The Raman process is a two phonon process. The spin system undergoes a transition from an initial state $|i\rangle$ to an intermediate state $|m\rangle$, by the absorption of a phonon q , and then from $|m\rangle$ to a final state $|f\rangle$ by the emission of another phonon q' . This process is termed coherent (or elastic) when the energies of the initial and final states are equal, and inelastic when they differ. These two cases are shown in Figure 4.2 and Figure 4.3 respectively. Kwok (1966) identified two inelastic processes for two states separated in energy by $\hbar\omega_0$.

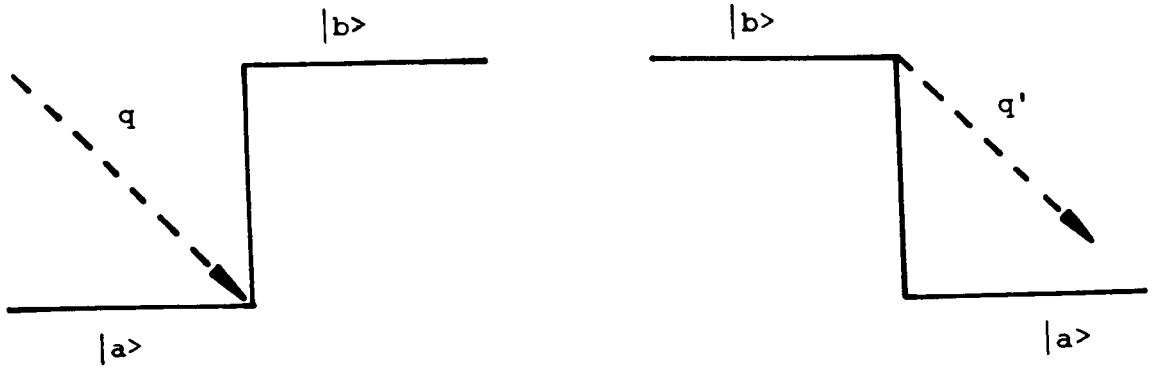


Figure 4.1: The Direct Process

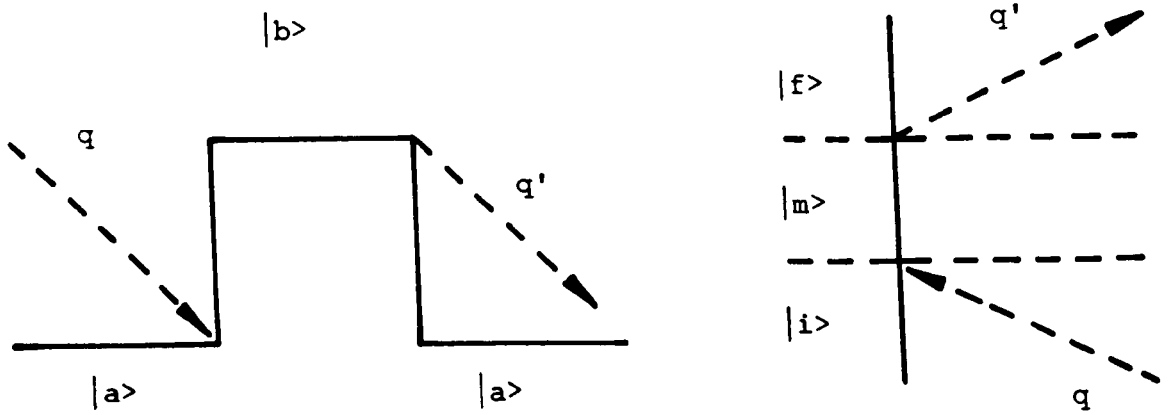
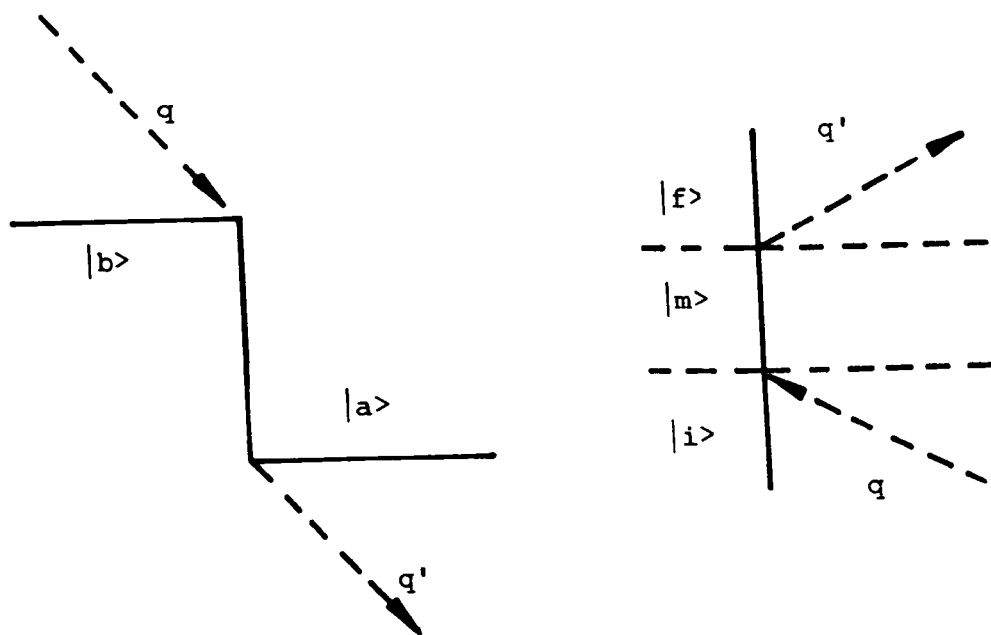


Figure 4.2: The Coherent Process

(a)



(b)

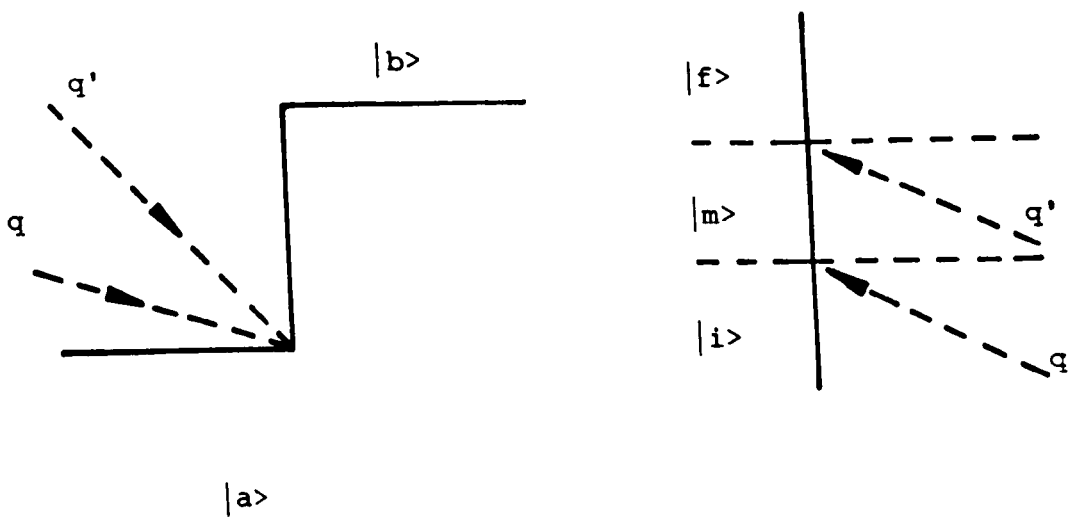


Figure 4.3: Inelastic Scattering Processes

- (1) A phonon q scattering into a phonon q' causing the spin system transition from a state $|b\rangle$ to a state $|a\rangle$ of different energy.
- (2) A phonon q with energy $E_q < \hbar\omega_0$, assisted by a thermal phonon causing the transition from a state $|a\rangle$ to a state $|b\rangle$ of different energy.

4.2.3 The Boron Acceptor in Silicon

The boron acceptor in silicon directly substitutes for a silicon atom and, thus, sits at a site of tetrahedral symmetry. As it is a group III element we have a vacancy in the covalent bonding which may be filled by an electron from the valence band. This leaves a hole in the valence band which is free to move when the temperature, T , is sufficient that $T > E_b/k$, where E_b is the hole-acceptor binding energy. At low temperatures, however, the hole is bound to the acceptor.

The effective mass approximation (EMA) assumes a Coulombic binding potential given by

$$V = \frac{e}{4\pi\epsilon\epsilon_0 r} \quad (4.32)$$

where ϵ is the dielectric constant of silicon. The system is analogous to the hydrogen atom but with the binding force screened by the silicon lattice. The periodicity of the silicon lattice changes the mass of the hole from its free space value, m_0 , to an effective mass, m^* . This approximation will break down for small

values of r when the potential ceases to be Coulombic, and so cannot be used for tightly bound holes (or electrons). For Si(B) the binding energy is 44 meV (for hydrogen it is 13.6 eV) and so the orbit is large (~ 2 nm).

Shallow acceptor states in silicon are constructed from states from the top of the valence band. These states are situated at the centre of the Brillouin zone and are six-fold degenerate. This degeneracy is lifted by the spin-orbit interaction into a four-fold degenerate $J = \frac{3}{2}$ state and a two-fold degenerate $J = \frac{1}{2}$ state. The $J = \frac{3}{2}$ state lies 33 meV above the valence band edge and is termed in group theory notation, Γ_6 . The $J = \frac{1}{2}$ states cannot interact with phonons as the transition involved is forbidden, and will be neglected. External perturbations such as magnetic field or stress will raise the degeneracy of these levels.

The effect of lattice strains (phonons) on holes in the valence band can be treated with the deformation potential method introduced in section 4.1.1. Kleiner and Roth (1959) wrote the Hamiltonian as

$$H_V = D_d(e_{xx} + e_{yy} + e_{zz}) + \frac{2}{3} D_u [(J_x^2 - \frac{1}{3} J^2)e_{xx} + \text{c.p.}] + \frac{1}{3} D_u' [(J_x J_y + J_y J_x)e_{xy} + \text{c.p.}] \quad (4.33)$$

where c.p. denotes cyclic permutation, \underline{J} is the angular momentum vector, D_d , D_u and D_u' are the valence band deformation potentials and e_{xx} , e_{yy} , e_{zz} and e_{xy} are components of the strain tensors (for

example, e_{xx} refers to uniaxial strain along the x-axis). As D_d refers to a volume dilatation of the lattice uniformly shifting the energy of the whole band, it will be neglected. D_u and $D_{u'}$ describe the effect of uniaxial stress applied along the [001] and [111] directions respectively. The Hamiltonian describing the splitting of the acceptor states is, thus,

$$H_V^a = \frac{2}{3} D_u^a \left[(J_x^2 - \frac{1}{2} J^2) e_{xx} + \text{c.p.} \right] + \frac{1}{3} D_{u'}^a \left[(J_x J_y + J_y J_z) e_{xy} + \text{c.p.} \right] \quad (4.34)$$

D_u^a and $D_{u'}^a$ are different from D_u and $D_{u'}$ to take account of the departure of the acceptor groundstate from the hydrogenic model.

Suzuki and Mikoshiba (1971a) (SM theory) demonstrated that phonon scattering by the Γ_6 groundstate explained the data of Carruthers et al (1957) and Holland and Neuringer (1962). They calculated the averaged single mode scattering rates for this process, and then including boundary scattering and isotope scattering develop an expression for the thermal conductivity.

The application of a magnetic field causes the degeneracy of the acceptor groundstate to be lifted. The Hamiltonian describing this is

$$H = - \mu_B (\underline{l} \cdot \underline{B} + 2 \underline{s} \cdot \underline{B}) - \frac{1}{2} m^* \mu_B^2 [r^2 B^2 - (\underline{r} \cdot \underline{B})^2] \quad (4.35)$$

where \underline{l} is the angular momentum vector, \underline{s} is the spin angular

momentum, μ_B is the Bohr magneton and \underline{r} is the position operator. In silicon with $B \leq 6$ T the second order terms in equation (4.35) can be ignored, Russell (1988).

Bhattacharjee and Rodriguez (1972) write the Hamiltonian for the interaction between a magnetic field and a Γ_6 level as

$$H = \mu_B g'_1 (\underline{B} \cdot \underline{J}) + \mu_B g'_2 (B_x J_x^2 + B_y J_y^2 + B_z J_z^2) \quad (4.36)$$

where g'_1 and g'_2 depend on the unperturbed wavefunctions of the Γ_6 level. With the magnetic field parallel to a major axis, for example the z-axis, the eigenvalues of the Hamiltonian are

$$E_\mu = \mu_B (g'_1 \mu + g'_2 \mu^3) B \quad (4.37)$$

where $\mu = 3/2, 1/2, -1/2, -3/2$

In the conventional notation we obtain the g-factors

$$g_{\frac{1}{2}} = g'_1 + \frac{9}{4} g'_2$$

$$g_{\frac{3}{2}} = g'_1 + \frac{1}{4} g'_2$$

which with equation (4.37) show we have energy splittings

$$\Delta_{12} = \Delta_{34} = \frac{1}{2} (3g_{\frac{3}{2}} - g_{\frac{1}{2}}) \mu_B B$$

$$\Delta_{13} = \Delta_{24} = \frac{1}{2} (3g_{\frac{1}{2}} + g_{\frac{3}{2}}) \mu_B B$$

$$\Delta_{14} = 3g_{\frac{3}{2}} \mu_B B$$

and

$$\Delta_{23} = g_{\frac{1}{2}} \mu_B B$$

Here the levels labelled 1, 2, 3 and 4 correspond to $m_j = 3/2, 1/2, -1/2$ and $-3/2$ respectively.

Thus, the application of a magnetic field allows two additional phonon absorption processes which resonantly scatter phonons over two narrow frequency ranges centred at

$$\nu_{12} = \Delta_{12}/h = 16.4 \text{ B GHz/Tesla}$$

$$\nu_{13} = \Delta_{13}/h = 31.5 \text{ B GHz/Tesla.}$$

Suzuki and Mikoshiba (1971b) calculated the single mode scattering rates, and the full expressions are given in Heraud (1985).

The application of uniaxial stress will also raise the degeneracy of the level via the Hamiltonian in equation (4.33). This equation simplifies for stress parallel to the [100] and [111] directions, but for stress parallel to the [110] axes, the Kramers doublets formed are admixtures of the $m_j = \pm 3/2$ and the $m_j = \pm 1/2$ states. Russell (1988) considers this situation and rewrites the Hamiltonian in equation (4.33) for stress parallel to the [110] axes. Russell calculates the resulting energy splitting for an applied stress T , as

$$\Delta = \frac{2}{3} T [D_u^2 (s_{11} - s_{12})^2 + \frac{3}{4} D_u^2 s_{44}]^{\frac{1}{2}} \quad (4.38)$$

where s_{11} , s_{12} and s_{44} are the elastic stiffness constants, and then calculates the single mode scattering rates.

An interesting result of these calculations is that the energy splitting, Δ , is linearly dependent on stress, and that the width of the "hole" burned in the phonon spectrum increases as Δ^2 .

4.3 PHONON FOCUSING

Phonon focussing arises from a material having anisotropic elastic constants. This anisotropy produces a non-spherical constant frequency surface in k-space. As the energy flux associated with ballistic phonons is parallel to the group velocity, which is a vector normal to the constant frequency surface given by

$$\underline{v}_g = \frac{\partial \omega(\underline{k})}{\partial \underline{k}} \quad (4.39)$$

the non-spherical constant frequency surface causes the energy flux to be concentrated along certain directions. Thus, for a point source producing an isotropic distribution of k-vectors, the phonon energy is concentrated, or focussed, along directions for which the curvature of the constant frequency surface is small. McCurdy et al (1970) first explained this focussing of phonon energy.

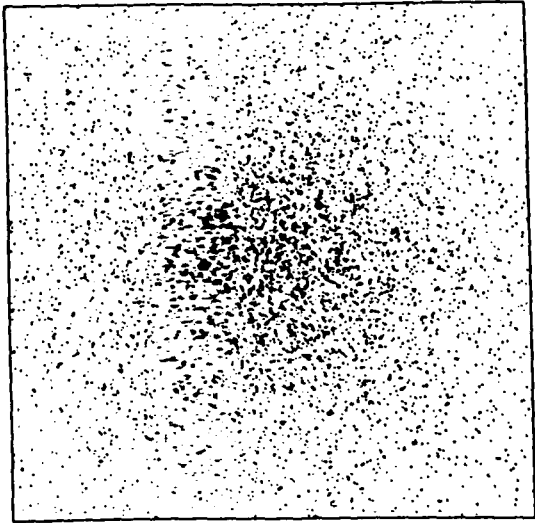
To calculate the phonon focussing effects in silicon, it is necessary to calculate the constant frequency surface from the elastic stiffness constants. These are available from ultrasonic experiments, and Marx and Eisenmenger (1982) have performed Monte-Carlo simulations showing the focussing patterns produced in silicon. Their results for an isotropic point heat source, are reproduced in Figure 4.4 .

4.4 REVIEW OF PREVIOUS WORK

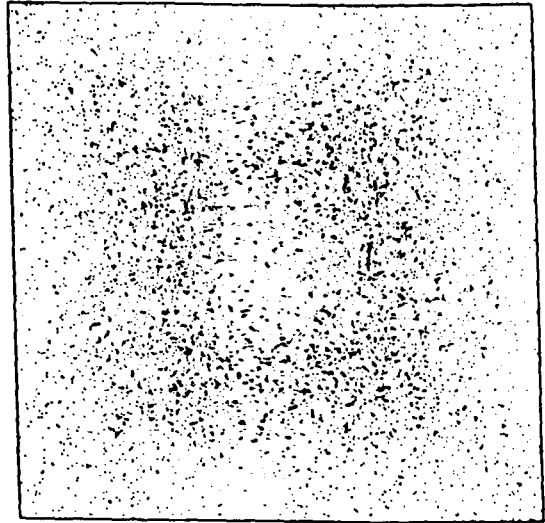
4.4.1 Zero Magnetic Field

The theory presented in section (4.1) allows the phonon emission from a hot 2DEG to be evaluated numerically. Challis et al (1987) have done this and the results show the expected strong forward coning of the emission produced by the $2k_F$ restriction on $q_{||}$. The calculations performed neglect the q_z restriction as it was assumed that the 2DEG thickness, a , was 1 nm, and also did not include phonon focussing. For low electron temperatures the theory predicts that as the cut-off occurs at much higher frequencies than can be emitted thermally, the power emitted depends only on the phonon distribution function. This leads to $P \propto (T_e^5 - T^5)$. An alternative situation is that the electron temperature is so high that the peak of the electron distribution ($\approx 3.8 k_B T_e$) is above the cut-off producing $P \propto (T_e - T)$.

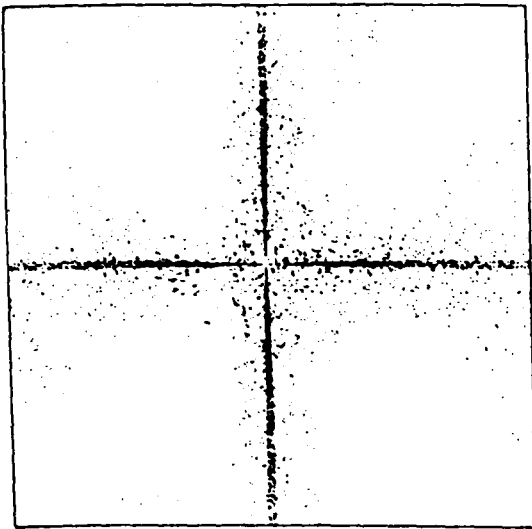
Several other authors have calculated energy loss rates. Shinba et al (1982) calculated energy loss rates in silicon MOSFETs and found $P \propto (T_e - T)$ for $T > 10$ K. This agreed with Nakamura



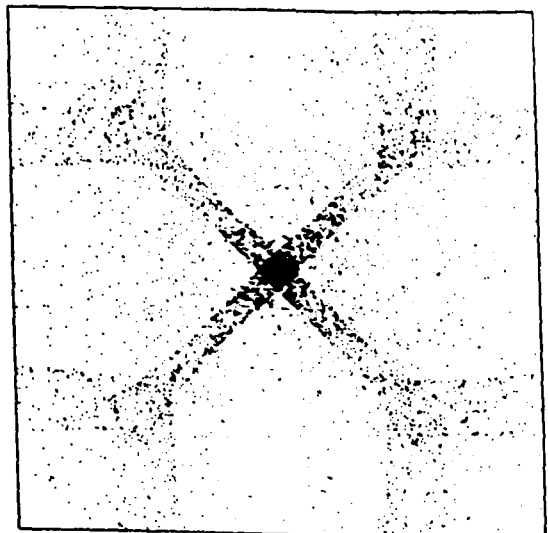
(a) Isotropic Media



(b) Silicon - Longitudinal Mode



(c) Silicon - Fast Transverse Mode



(d) Silicon - Slow Transverse Mode

Figure 4.4: Phonon Focussing Patterns (after Marx and Eisenmenger 1982)

(1976) who performed identical calculations for $T = 300 \text{ K}$ and $T = 77 \text{ K}$. For $T \ll 1 \text{ K}$, however, Shinba found that $P \propto T^4 E_F^{-\frac{3}{2}}$. Their experimental results, in the range $1 \text{ K} \leq 10 \text{ K}$, lay between these two predictions.

Payne et al (1983) carried out an experimental investigation at very low temperatures ($T = 0.17 \text{ K}$) on silicon MOSFETs using the localisation correction to the conductivity to measure T_e . The low sample temperatures lead to very long phonon mean free paths and they introduced a correction into the theory to account for the phonon mean free path being far larger than the electron mean free path, λ_e . This correction multiplied all the matrix elements by $q\|\lambda_e$, producing $P \propto (T_e^6 - T^6)$.

The first direct experimental evidence for the interaction of acoustic phonons with a 2DEG was reported by Hensel et al (1983a). They investigated the absorption of a heat pulse by a cold 2DEG using an Al tunnel junction bolometer. The geometry of the experiment meant that the heat pulse passed through the 2DEG twice and was reflected off the oxide-silicon interface once on its way to the detector. Their results showed far greater absorption than was expected and this was explained by Hensel (1983b) who considered interference effects between the phonons reflected from the 2DEG and from the oxide/silicon interface.

Phonon emission from a heated 2DEG was first investigated by Chin et al (1984) using GaAs/AlGaAs heterostructures. They used an Al tunnel junction bolometer to detect the phonons emitted from

pulse heating the 2DEG with different applied electric fields. For low electric fields ($E \sim 1 \text{ Vcm}^{-1}$) a very clear TA pulse was seen, when the electric field was increased, however, another peak was seen which for high electric fields ($E > 12 \text{ Vcm}^{-1}$) dominated. By comparing their data with the mobility versus temperature dependence of their samples, and calculating T_e using $P/n_s = (T_e - T)$, they attributed the low electric field results to piezoelectric coupling emitting TA phonons, and the high electric field results to the emission of polar longitudinal optic (LO) phonons which down-convert to slow TA phonons. They also reported results for a hole gas and demonstrated that holes are more strongly coupled to phonons.

Rothenfusser et al (1986) performed a more detailed study of phonon emission using large area ($1 \times 1 \text{ mm}$) silicon MOSFETs fabricated on 3 mm thick substrates ($300 \Omega\text{cm}$). The 2DEG was pulse heated capacitively, and the resulting phonon emission detected by either Pb or Al tunnel junction bolometers. The Al bolometers have a detection "window" with a lower limit of 100 GHz, while for the Pb bolometers the lower limit is 650 GHz. As isotope scattering limits the phonon frequencies passed to $\sim 800 \text{ GHz}$, the Pb bolometers only detect phonons in a 150 GHz band. By using several detectors, the angular dependence of the emission was measured. Their results agreed well with the theoretical analysis given which included screening of the deformation potential. Anomalous effects were seen for $n_s > 4 \times 10^{12} \text{ cm}^{-2}$ which they ascribed to population of the second subband. The $2k_F$ cut-off was seen clearly, as were phonon drag effects when the current in the device was reversed.

Kent et al (1987) also used heat pulse techniques to

investigate the phonon emission from a heated 2DEG, but with CdS bolometers. These bolometers are broadband phonon detectors, but are not as sensitive as the tunnel junction detectors. They used three bolometers, two situated on the opposite face of the sample, and one on a face perpendicular to the plane of the 2DEG. They only detected signals with the bolometer directly opposite the 2DEG, implying that the emission was cut-off for $\theta \sim 40^\circ$. Rothenfusser obtained signals at $\theta \sim 54^\circ$ by working with higher electron densities and using the more sensitive tunnel junction detectors.

The angular dependence of phonon emission was also investigated by Dietsche (1986) who used an extended 6 x 4 mm tunnel junction detector. By illuminating the tunnel junction with a focussed laser spot, a small area of the detector could be "turned on" allowing detection of phonons. Raster scanning the laser spot allowed the production of a "phonograph" of phonon emission. The main feature of their data was a dominant peak at $\theta \sim 0^\circ$. This is expected if phonon focussing is taken into account as the TA phonons are strongly focussed in the forward direction (see Figure 4.4).

The heat pulse work has shown that the predominant phonon emission process is by TA phonon emission. Newton (1987) performed some heat pulse measurements with varying n_3 showing the proportion of the phonons emitted in the TA and LA modes. Although he did not analyse these results it is clear from his data that at low n_3 a greater proportion of the phonons emitted are in the LA mode.

4.4.2 Quantising Magnetic Field

The first report of the direct interaction of electrons and phonons in a quantising magnetic field was by Eisenstein et al (1986). They used the conductivity, ρ_{xx} , of a Corbino geometry device to detect phonons transmitted into their samples through a thin layer of liquid ^4He . The frequency dispersion of ^4He allows phonons below a critical frequency, ν_0 , to be transmitted ballistically, while those above ν_0 are down converted to less than 20 GHz. ν_0 can be reduced by applying hydrostatic pressure. By operating at high magnetic fields and low heater powers they investigated intra-Landau level absorption and, as expected, saw a decrease in the absorption of phonons by the device with increasing pressure (less low frequency down converted phonons). Another feature of their data was that the effect was more pronounced at low fields and this was ascribed to greater localisation arising from the increased separation of the SHO states.

Wixforth et al (1986) investigated the interaction of surface acoustic waves (SAWs) with a 2DEG in a GaAs/AlGaAs heterostructure. They saw oscillations in the absorption of the SAWs by the 2DEG corresponding to the SdH oscillations in the resistivity, ρ_{xx} , of their device.

Rampton et al (1987) propagated heat pulses through a 2DEG in a silicon MOSFET and detected the signal with a CdS bolometer situated on the gate electrode. They observed heat pulse attenuation, while sweeping n_s that, for $B < 5$ T, was out of phase with the electrical SdH oscillations. However, for $B > 5$ T the attenuation

was in phase with the SdH oscillations. They proposed that the dominant phonon absorption mechanism was changing from inter-Landau level to intra-Landau level absorption. At low fields with $\hbar\omega_d \gg \hbar\omega_c$ (where ω_d is the dominant phonon frequency) the maximum absorption occurs when E_F is within a Landau level. For $\hbar\omega_d < \hbar\omega_c$, the maximum absorption occurs when E_F is between Landau levels. Thus a change of phase occurs when $\hbar\omega_d \sim \hbar\omega_c$.

Kent et al (1987) investigated heat pulse absorption by a cold 2DEG by utilising the change in resistance of the silicon MOSFETs they were using that occurs as the electrons are heated by the phonons. They found that for low pulse powers, the absorption oscillations were in phase with the SdH oscillations. However, when the heat pulse power was increased another set of oscillations arose between the peaks of the first set, which were exactly out of phase with the SdH oscillations. They proposed that this was evidence for an increasing proportion of the phonons being absorbed by inter-Landau level transitions as the heater power and, hence, the peak in the phonon energy distribution, was increased.

Eisenstein et al (1988) used a Searle's bar geometry, thermal conductivity apparatus, to investigate the transport of phonons along a GaAs sample with a multiple quantum well GaAs/AlGaAs structure grown along the entire top face. Heat was injected into the sample with a resistive heater, and removed by a heat sink whose temperature varied in the range $0.1 \text{ K} \leq 2 \text{ K}$. The temperature was measured at two points along the sample with carbon resistance thermometers mounted directly onto the sample. The samples were $50 \mu\text{m}$ thick with highly specular surfaces ($\sim 75\%$ specular reflec-

tion), so the phonons passed ballistically through the 2DEG several times between each thermalising scattering event at a boundary. Thermal conductance oscillations were observed as E_F was swept through the successive Landau levels and attributed to the variation of the electron-phonon scattering rate. Eisenstein et al suggested that the dependence of the electron-phonon scattering rate upon $q_{\parallel} \ell_B$ could be obtained from measuring the amplitude of the oscillations and presented data for consecutive Landau levels.

Kent et al (1987) looked at the phonon emission from a pulse heated silicon MOSFET in magnetic fields up to 7 T. The MOSFETs were fabricated on thick (5 mm) substrates to allow time-of-flight methods to be employed. The thickness of the wafers lowered the isotope scattering threshold to ~ 800 GHz and they utilized this as a low pass phonon filter to probe the amount of phonon emission at the cyclotron frequency. For power inputs above 1 Wmm^{-2} , they observed considerable phonon emission at the cyclotron frequency, and the proportion of phonons at the cyclotron frequency increased with the power dissipated in the 2DEG.

CHAPTER 5Computer Modelling5.1 INTRODUCTION

In Chapter 6 measurements of the temperature gradient developed along a Si(B) substrate are presented. Heat is injected into the substrate in three ways.

- (1) From a resistive heater situated at the end of the sample.
- (2) From a resistive heater situated on the top face of the sample directly above one thermometer.
- (3) From a heated 2DEG situated as in (2).

The resistive heaters will inject heat isotropically if we neglect focussing effects. The phonon emission theory for a heated 2DEG in Chapter 4, however, makes it clear that the 2DEG heater will inject phonons confined to a cone, with the half angle, θ , of the cone determined by the gate voltage applied.

To enable quantitative analysis of the results presented in Chapter 6 it is necessary to know how the three methods of injecting heat affect the temperature profile along the sample.

5.2 THEORY

Russell (1988) calculated the phonon scattering rates for the Si(B) substrates used in this work using the theory of Suzuki and Mikoshiba (1971a), with a correction developed by Wybourne et al (1984) to allow for the large sample aspect ratio. For a boron concentration of approximately 10^{13} cm^{-3} ($\rho \sim 1000 \text{ cm}$), and an aspect ratio of $\sim 20:1$, Russell found that the boundary scattering rate was three orders of magnitude higher than the elastic scattering rate from the Γ_8 . At low temperatures, $< 4 \text{ K}$, the isotope scattering can also be neglected, therefore, it is a reasonable assumption to ignore totally any phonon scattering within the bulk of the substrate. If we also assume that the surface is perfectly black, ie it absorbs all the phonons falling upon it and re-emits them in a frequency distribution determined solely by the local temperature, we can follow the method of Eddison and Wybourne (1985) to calculate the energy flux, dH , received by a small element of surface dA_1 , from another element dA_2 . They give

$$dH = QT_2^4 \cos\phi \, dA_2 \, d\Omega \quad (5.1)$$

with

$$Q = \frac{\pi^4 k_B^4}{15h^3} \sum_i \frac{1}{v_i^2}$$

where $d\Omega$ is the solid angle subtended by dA_1 , ϕ is the angle between the normal to dA_2 , \hat{n}_2 , and a line linking the centres of the two surface elements and v_i are the longitudinal and transverse phonon

velocities. The geometry of the problem is shown in Figure 5.1 in a simple two-dimensional projection neglecting the displacement of the two elements in the y-direction. By defining $\underline{R} = |\underline{R}|\hat{R}$, and considering the elements to be long strips extending in the y-direction with \underline{R}_{xz} as the projection of \underline{R} in the x-z plane, we can simplify equation (5.1) and obtain,

$$dH = QT_2^2 dA_1 dA_2 \cos\theta' \cos\phi \frac{|\underline{R}_{xz}|^2}{|\underline{R}|^4} \quad (5.2)$$

Considering two strips, the total phonon intensity received by any point on strip 1, I_1 , from the whole of strip 2, is

$$I_1 = \frac{1}{dA_1} \int dH = QT_2^2 l_2 \cos\theta' \cos\phi |\underline{R}_{xz}|^2 \int_{-\infty}^{\infty} \frac{dy}{|\underline{R}|^4} \quad (5.3)$$

where $dA_2 = l_2 dy$.

The integral is evaluated by writing $|\underline{R}|^4 = (x^2 + y^2 + z^2)^2$, and then simplified by using, $|\underline{R}_{xz}| = (x^2 + z^2)^{\frac{1}{2}}$. This gives

$$I_1 = QT_2^2 l_2 \cos\theta' \cos\phi \frac{\pi}{2|\underline{R}_{xz}|} \quad (5.4)$$

From Figure 5.1

$$\delta\theta' = \frac{l_2 \cos\phi}{|\underline{R}_{xz}|}$$

and so substituting $\delta\theta'$, and generalising for the intensity received

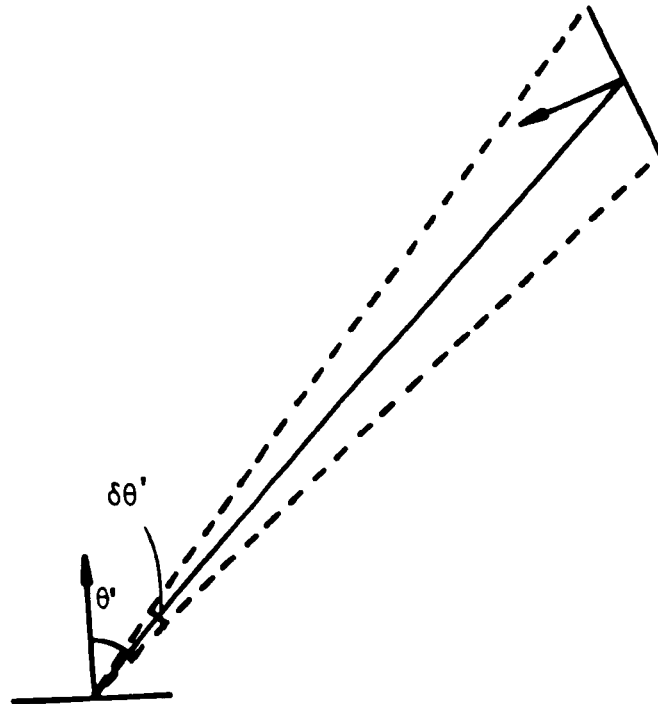
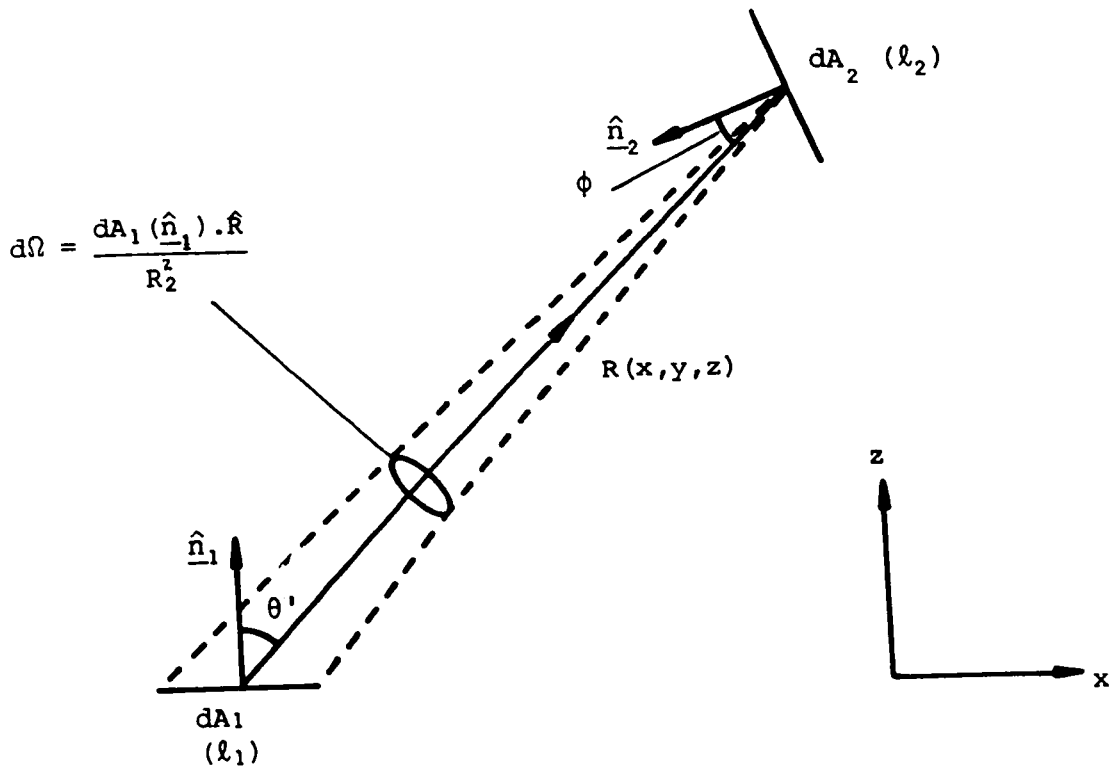


Figure 5.1: Schematic Diagram of the Geometry

by a strip i , from a strip j ,

$$I_{ij} = \frac{\pi}{2} QT_j^* \delta\theta'_{ij} \cos\theta'_{ij} \quad (5.5)$$

For a prism of complicated cross-section in the x - z plane and with the heat flow pattern independent of the y -direction, we can divide the surface into a large number of strips and consider the phonon intensity received by each strip per unit length. Thus, for the i th strip

$$P_i(\text{in}) = \sum_{j \neq i} l_i \frac{\pi}{2} QT_j^* \delta\theta'_{ij} \cos\theta'_{ij} \quad (5.6)$$

We can also write the phonon intensity emitted from the i th strip

$$P_i(\text{out}) = \sum_{j \neq i} l_i \frac{\pi}{2} QT_i^* \delta\theta'_{ij} \cos\theta'_{ij} \quad (5.7)$$

Thus, for a strip i , which is not itself a source or sink of heat, the phonon intensity into the strip must equal the phonon intensity out of the strip and we can equate equations (5.6) and (5.7). Generalising to take account of any sources or sinks by including a term S_i , yields

$$\sum_{j \neq i} T_j^* \delta\theta'_{ij} \cos\theta'_{ij} + S_i = \sum_{j \neq i} T_i^* \delta\theta'_{ij} \cos\theta'_{ij} \quad (5.8)$$

If we assume that the temperatures, T_i , only vary slightly from a temperature T_0 , we can perform a Taylor expansion and write

$$(T_0 + T_i)^* = T_0^* + 4T_0^3 T_i + \dots \quad (5.9)$$

Neglecting terms higher than linear in T_i and substituting this into equation (5.8) gives

$$T_i = \frac{\sum_{j \neq i} T_j \delta\theta'_{ij} \cos\theta'_{ij}}{\sum_{j \neq i} \delta\theta'_{ij} \cos\theta'_{ij}} + \frac{S_i}{\sum_{j \neq i} \delta\theta'_{ij} \cos\theta'_{ij}} \quad (5.10)$$

If we define

$$W_{ij} = \frac{\delta\theta'_{ij} \cos\theta'_{ij}}{\sum_{j \neq i} \delta\theta'_{ij} \cos\theta'_{ij}} \quad j \neq i$$

$$= 0 \quad j = i$$

and

$$K_i = \frac{S_i}{\sum_{j \neq i} \delta\theta'_{ij} \cos\theta'_{ij}}$$

we can now rewrite equation (5.10) as

$$T_i = \sum_j W_{ij} T_j + K_i \quad (5.11)$$

5.3 METHOD OF SOLUTION

Two possible methods exist for solving equation (5.11). The first uses matrix inversion to solve the M linear equations produced by equation (5.11) for M strips of unknown temperature. It was thought that this method would be very time consuming for the 100-200 strips required to simulate the experimental situation. The second method uses an iterative technique. All the strips of unknown temperature are initially assigned a uniform temperature. The sources are assigned a higher temperature, and the sinks are

assigned zero temperature. Then an iterative loop calculates each strip temperature using equation (5.11) until the temperatures converge. Throughout this iteration the source and the sink temperatures are kept fixed.

An annotated listing of the computer program used to perform this iterative procedure is given in Appendix A. This program is written in Fortran 77 for the Acorn Cambridge Workstation.

5.4 RESULTS

To simplify the computing the initial modelling was performed using 108 elements on a sample 5 mm in length rather than the actual 10 mm length of the samples used in the experiments. This is a reasonable simulation for the experiments with the heater in the centre of the sample, as the heater to heat sink distance is still correct (the additional 5 mm in the real sample is situated "upstream" of the heater and the heat sink). The 1 mm wide isotropic heater is positioned on the top face of the sample 3 mm away from the heat sink. The first calculations assumed $T = 0$ K for the heat sink, and $T = 1$ K for the heater, while the initial temperature of the other elements was $T = 0.5$ K. Figure 5.2 shows the results obtained for the front and back faces.

A more realistic model for an isotropic heater yields the results shown in figure 5.3 for the front and back faces. This model allows each of the surface elements that comprise the heater, to have a temperature determined by the phonon flux falling on them from the other elements, as well as the phonon flux generated by the

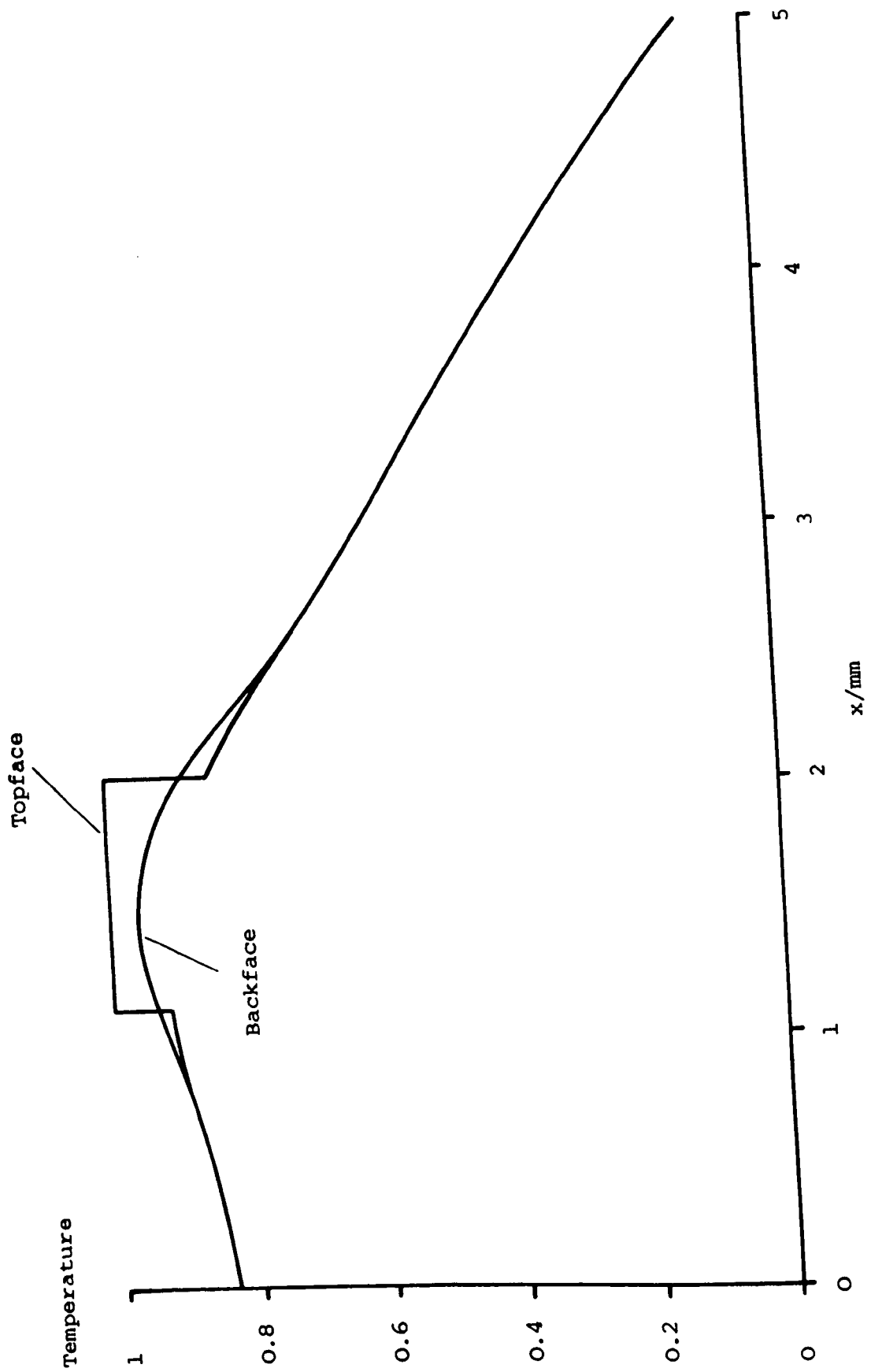


Figure 5.2: Temperature Profile with the Heater Temperature Fixed

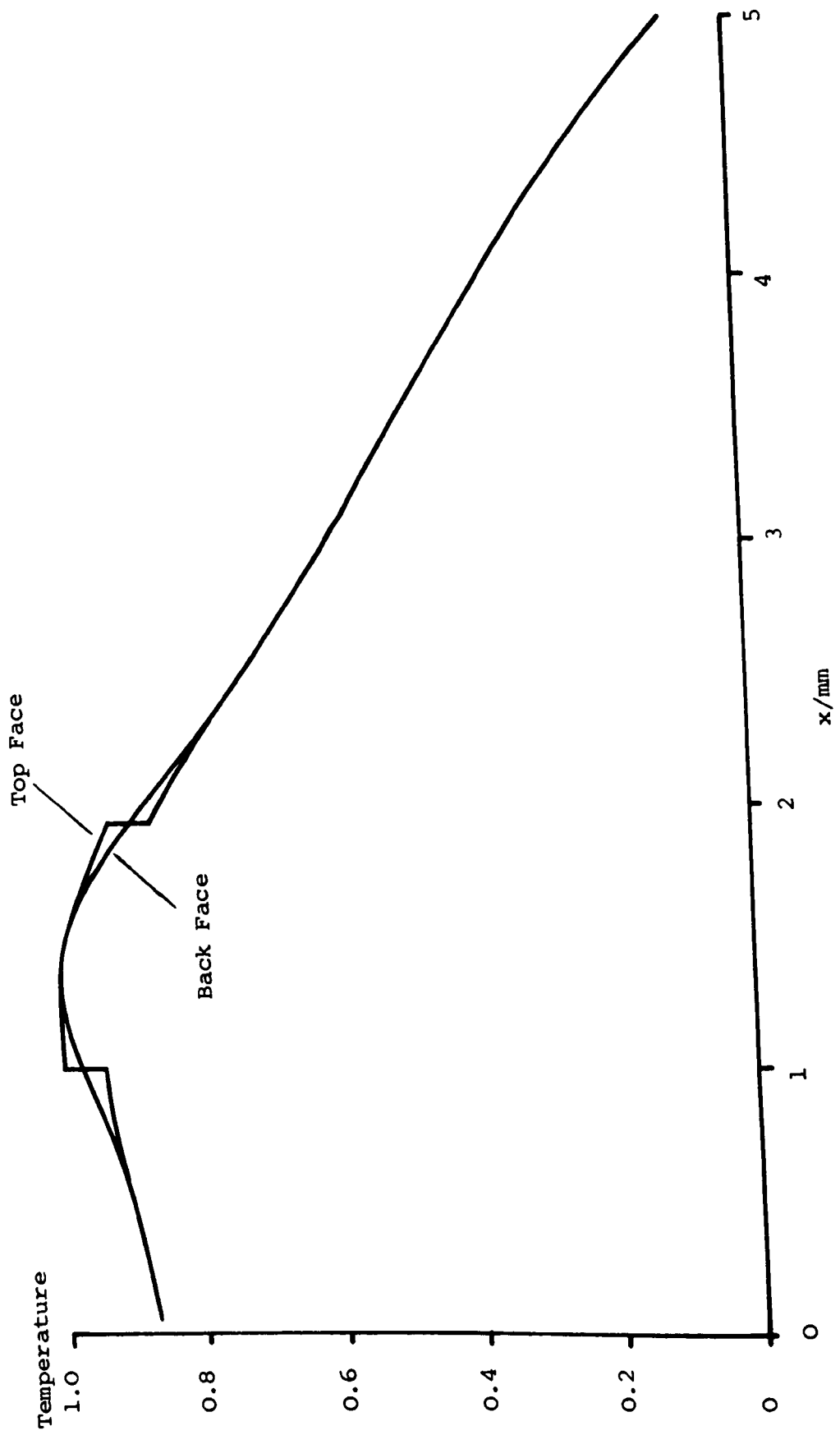


Figure 5.3: Temperature Profile with the Heater Temperature allowed to vary.

heater. Thus, in the model these heater elements have a minimum temperature set by the heater, and are then included in the iterative loop to calculate their final temperature. This model is valid for the 2DEG heater which is actually separated from the surface by ~ 1 nm, and only absorbs a very small percentage of the phonon flux passing through it. It is also valid for the resistive heater mounted on the surface of the sample and passing a uniform phonon flux into the sample. In this new model the sink temperature is still kept fixed at zero.

Figure 5.4. compares the temperature profile on the back surface obtained with isotropic heat input and with heat input restricted to a beam of $\pm 30^\circ$ to the normal. The temperature is evidently larger opposite the heater for the restricted beam.

5.5 DISCUSSION

From Figure 5.2 it is clear that temperature discontinuities exist at the edges of the heater and the heat sink. These discontinuities are still present in Figure 5.3 where the surface elements are in effect slightly removed from the heater, and their temperature is determined by all the phonon flux impinging on them. Although increasing the number of elements would probably smooth the discontinuity, it is clear that the temperature increases by approximately 10% in a 0.2 mm region at the edge of the heater. This sharp increase probably arises from the high aspect ratio of the samples as elements directly opposite each other subtend a large solid angle. No conduction occurs in the surface of the sample between neighbouring elements so the temperature of an element is

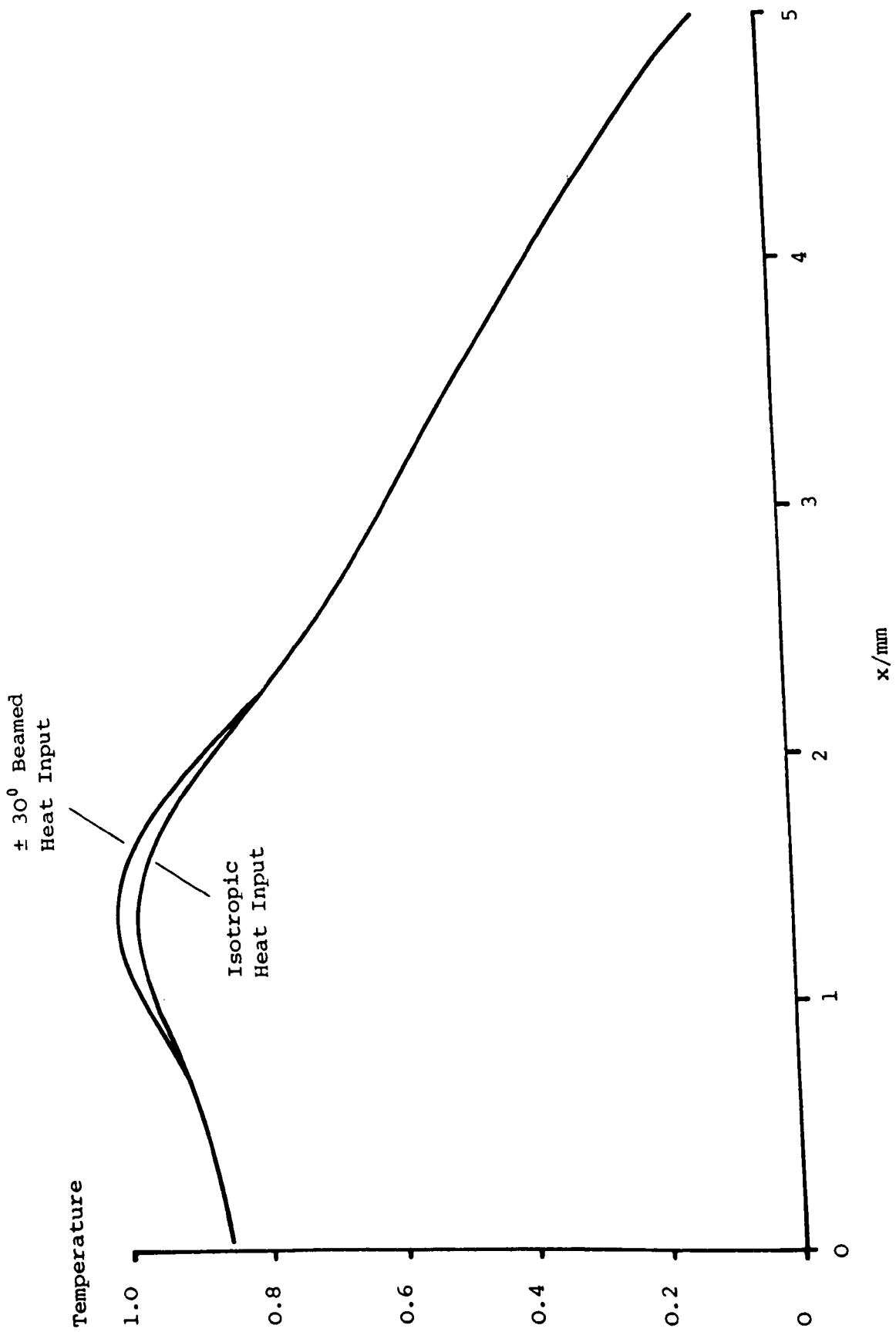


Figure 5.4: Temperature Profile on the Back Face for Isotropic Heat Input and Heat Input Restricted to a $\pm 30^\circ$ beam

largely determined by a few elements directly opposite.

The temperature gradient developed for a sample with the heater at one end, and a heat sink at the other is known to be linear when it is measured in a region well away from the source and sink. This is seen in the modelling results for the region $2.7 \text{ mm} < x < 4.5 \text{ mm}$, and presumably changing either the heat flux along the sample, or the length of the sample, will just change the gradient in this region. For both faces it is apparent that for $x > 4.5 \text{ mm}$ an end effect increases the temperature gradient (although a discontinuity exists at the heat sink), and for $1 \text{ mm} < x < 2.7 \text{ mm}$ the "hot spot" near the heater also increases the temperature gradient.

We next consider the region, $0 \text{ mm} < x < 1 \text{ mm}$. It at first seems surprising to find a temperature gradient in this region as there is no net heat flow in this direction since it is away from the heat sink. The temperature gradient found in this region can be attributed to the boundary scattering regime which is assumed by this model producing a situation analagous to radiant heat flow between surfaces at different temperatures situated in a vacuum. Clearly, the very high aspect ratio of the samples modelled leads to the temperature of an element being determined almost entirely by the few elements directly opposite as they occupy such a large proportion of the solid angle concerned. However, if any specular reflection is occurring at the surfaces, the temperature of an element will also be influenced by elements on its own face and by elements situated further away. This indicates that the 'upstream' region of the sample may be very interesting experimentally as it

could yield information about the amount of specular reflection occurring. This information is useful as it can indicate what surface defects and irregularities are present in a sample. Unfortunately the temperature gradient in this region will also be sensitive to phonon focussing and it may be necessary to model the focussing effects accurately to allow qualitative analysis.

The effect of changing from an isotropic heat input to an anisotropic heat input is shown clearly in Figure 5.4. To quantify the effect we measure the temperature difference between an element directly underneath the heater and an element in the linear temperature gradient region. This duplicates the experimental geometry used and will allow direct comparison with the results presented in Chapter 6. Comparing the temperature gradient obtained from an isotropic heat input with an anisotropic heat flux restricted to $\pm 30^\circ$ to the normal, and then with flux restricted to be entirely normal to the surface we find an increase of 1.4% and 1.5% respectively. This indicates that the increase in temperature of the hot spot directly under the device occurs quite rapidly as the "beaming" begins, and then slows down only increasing 0.1% between a beam of $\pm 30^\circ$, and a beam normal to the surface. This again shows the effect of the large aspect ratio of the samples. With the heat input restricted normal to the surface the temperature discontinuities shown in Figure 5.3 for the top face, appear on the bottom face as well.

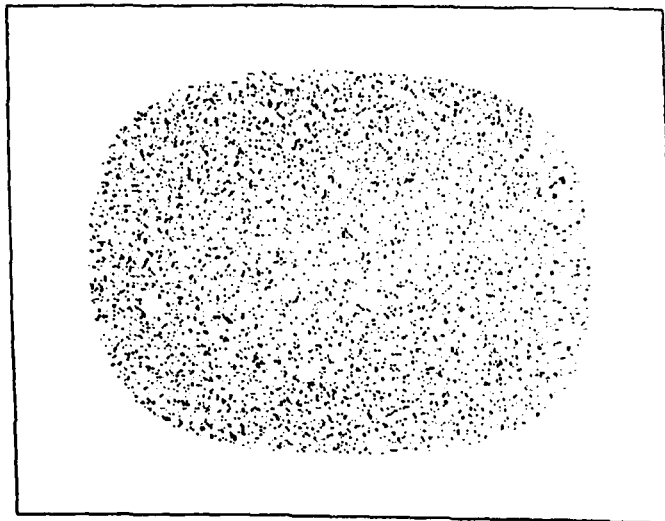
The results presented so far have not included any consideration of the phonon focussing effects. It is clear from Figure 4.3 that this will be an important effect, especially when simula-

ting emission from a 2DEG as the phonon emission is predominantly by TA phonons. As an approximate treatment of phonon focussing, an enhancement factor was introduced multiplying the phonon flux falling on an element if the emitting element was within a certain angle. To ensure that the total phonon flux emitted from each element was the same with and without this focussing enhancement, the coefficients linking the elements were normalised after the enhancement was included. Thus, for elements outside the focussing angle the phonon flux is reduced.

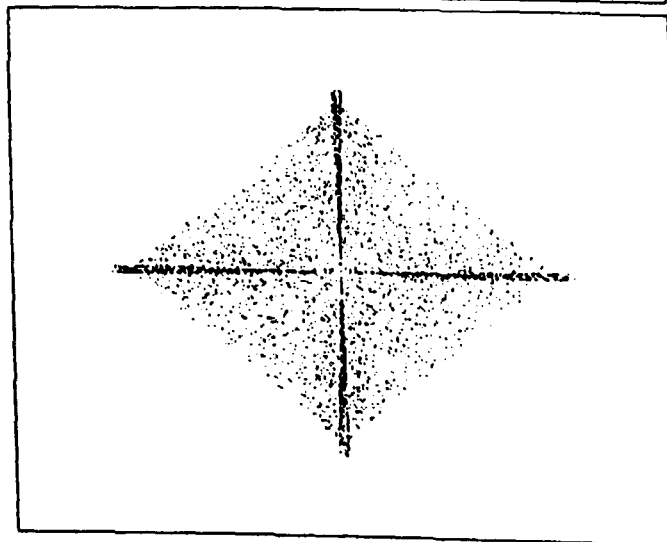
The first model to include the focussing approximation was for a heated 2DEG situated above one thermometer, emitting phonons restricted to a $\pm 30^\circ$ beam. The focussing enhancement used was to increase by a factor of 4 for elements within an angle of $\pm 30^\circ$ of each other. This gave a temperature gradient increase of 1.4% over that obtained for the same geometry without focussing. Comparing the same 2DEG heater with an isotropic heater both with the same focussing enhancement shows the temperature gradient for the device to be only 1.2% greater. This result shows the problem of using such a simple focussing treatment; the focussing enhancement has simply turned the isotropic heater into a partially beamed heater mimicing the 2DEG, and reducing the difference between them.

Hardy (1989) has performed phonon focussing calculations similar to those of Marx and Eisenmenger (1982) but rather than using an isotropic point heater, Hardy uses a point source emitting phonons in a $\pm 30^\circ$ cone. This produces the intensity patterns reproduced in Figure 5.5. Comparing the TA pattern (Figure 5.5c) with the TA pattern in Figure 4.3d, it is clear that the effect of

(a) Longitudinal



(b) Fast
Transverse



(c) Slow
Transverse

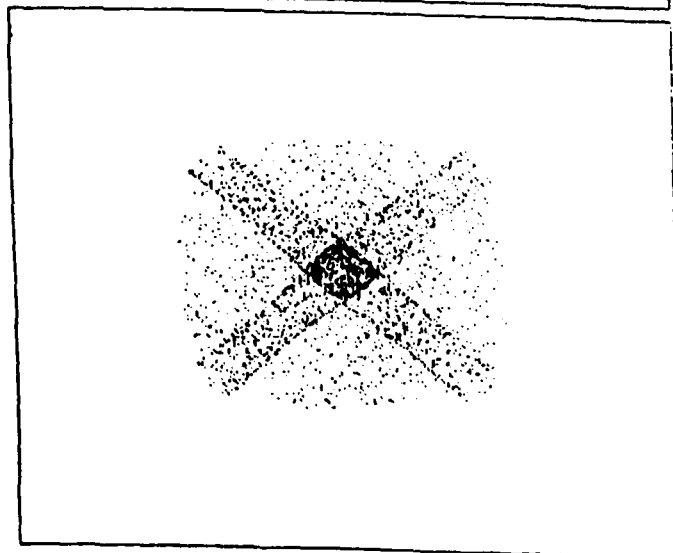


Figure 5.5: Focussing Patterns Resulting from a $\pm 30^\circ$ Beamed Heat Input (After Hardy 1989. The box edges correspond to $\pm 45^\circ$.)

the cone of phonon emission, along with the phonon focussing, directs all the phonon flux into a cone of approximately $\pm 20^\circ$. This probably means that the model with the phonon flux from the 2DEG heater directed normal to the surface and with no focussing included, most closely simulates the experimental situation for a 2DEG with phonon emission limited to a cone. For an isotropic heater, however, the simple focussing enhancement will not be adequate as we have to consider all three phonon modes. Another factor is that with no restriction on the phonon emission, we will have similar focussing patterns along the other principal axes. In our samples the principal axes are arranged as shown in Figure 5.6, and these other focussing directions will have the effect of channelling heat away from the thermometer situated directly underneath the heater. If, for simplicity, we consider the TA modes hot spots are formed where the principal axes intersect a sample face. This channelling will completely remove the y-axis symmetry assumed in the model and any attempt to adapt the model would be very complicated.

For a resistive heater situated at the far end of the sample, well away from the thermometers and the heat sink, the complications introduced by focussing effects will not be a problem as any hot spots will be situated at the far end of the sample. This situation can, thus, be considered with the simple model neglecting heat flow in the y-direction. It is also interesting to consider the effect of the simple focussing treatment on the temperature profile, as this may simulate the decrease in thermal conductivity which arises when one of the principal focussing directions lie along the length of the sample. To facilitate this, we developed a new model which simulates the experimental situation more closely.

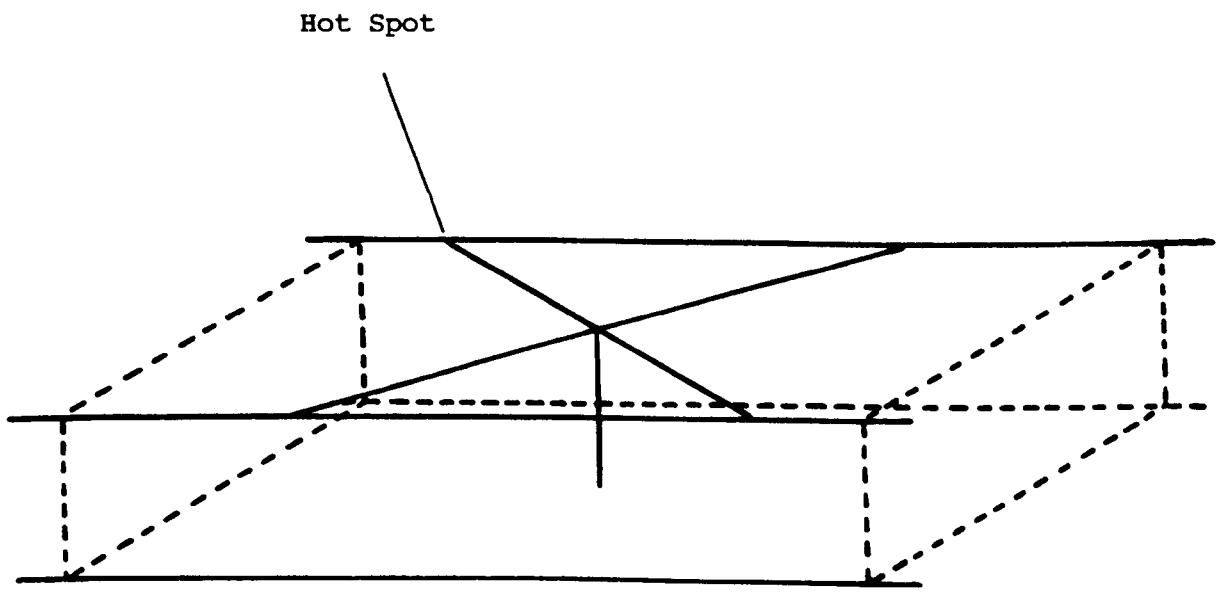


Figure 5.6: Principal Axes in the Samples used Showing Potential "Hot Spots"

This model has a sample 10 mm long and uses 208 elements so that the elements are the same size as in the previous model. Two heaters are used: a 1 mm wide isotropic heater on the top face of the sample at the very end, or alternatively, a 1 mm wide 2DEG emitting phonons into a $\pm 30^\circ$ beam on the top face of the sample, directly above one thermometer. The results from this model show that the temperature gradient produced by the isotropic heater at the end of the sample is 36% lower than that for the 2DEG in the centre of the sample. If we introduce a focussing enhancement of 10 times for elements within an angle of $\pm 30^\circ$ of each other, the temperature gradient due to the 2DEG increases by 2.7%, while that from the resistive heater rises by 5.6%. This shows that focussing may reduce the percentage difference in the temperature gradient between the isotropic heater and the anisotropic heater because of the thermal conductivity changes which will affect both equally.

5.6 FUTURE WORK

The results presented show that changing from an isotropic heater to a heater with a $\pm 30^\circ$ cone of phonon emission increases the temperature of a thermometer situated opposite by 1.5%, while any further restriction has only a very small effect. It would be interesting to use the model to determine the variation of the temperature of the thermometer as a function of the cone angle, θ . This would allow quantitative comparison to the restriction on the phonon emission from a 2DEG imposed by the $2k_F$ cut off presented in Chapter 6.

The simple focussing treatment presented is inaccurate as

the two-dimensional simplification used in the model means that the enhancement used links the strips (in the y-direction) when they are within a certain angle. A more realistic treatment would link elements when ϕ (the angle between the normal to the emitting element and $\underline{R}(x, y, z)$) was less than a certain angle. This will require a three-dimensional model increasing the computing involved considerably.

The model has shown that the region situated "upstream" of the heater and heat sink may be very interesting experimentally for investigations into specular reflection. It may be possible to extend the model to include specular reflection by using an effective phonon mean free path allowing the variation of the temperature gradient in this region to be determined as a function of the surface specularly.

In conclusion we note that the computer model described in the Chapter was initially set up by Professor A G Every (SERC Visiting Fellow) and has been extended in the ways described.

CHAPTER 6Experimental Results6.1 THERMAL CONDUCTIVITY

To form a baseline for the results presented later in this Chapter thermal conductivity measurements were performed on the Si(B) substrates as received from Wacker Chemtronic. The substrates used have a very low boron concentration $\sim 10^{13} \text{ cm}^{-3}$, and from the calculations of Russell (1988) it is expected that elastic phonon scattering by the Γ_1 groundstate will not have an appreciable effect on the measured thermal conductivity in the absence of magnetic field or stress. The results obtained are shown in Figure 6.1 with the line shown corresponding to a T^3 dependence. Except at low temperatures, the experimental points show a very good fit to this line indicating that the phonon mean free path is constant and, hence, that the boron is having very little effect on the thermal conductivity. The T^3 dependence arises from the temperature dependence of the lattice specific heat which would be present in a completely pure silicon sample.

For $T < 1.8 \text{ K}$ the experimental points deviate from the T^3 dependence. This is assumed to be due to specular reflection occurring at the surfaces of the sample, which increases the average phonon mean free path and, thus, increases the thermal conductivity. Specular reflection occurs when the phonon

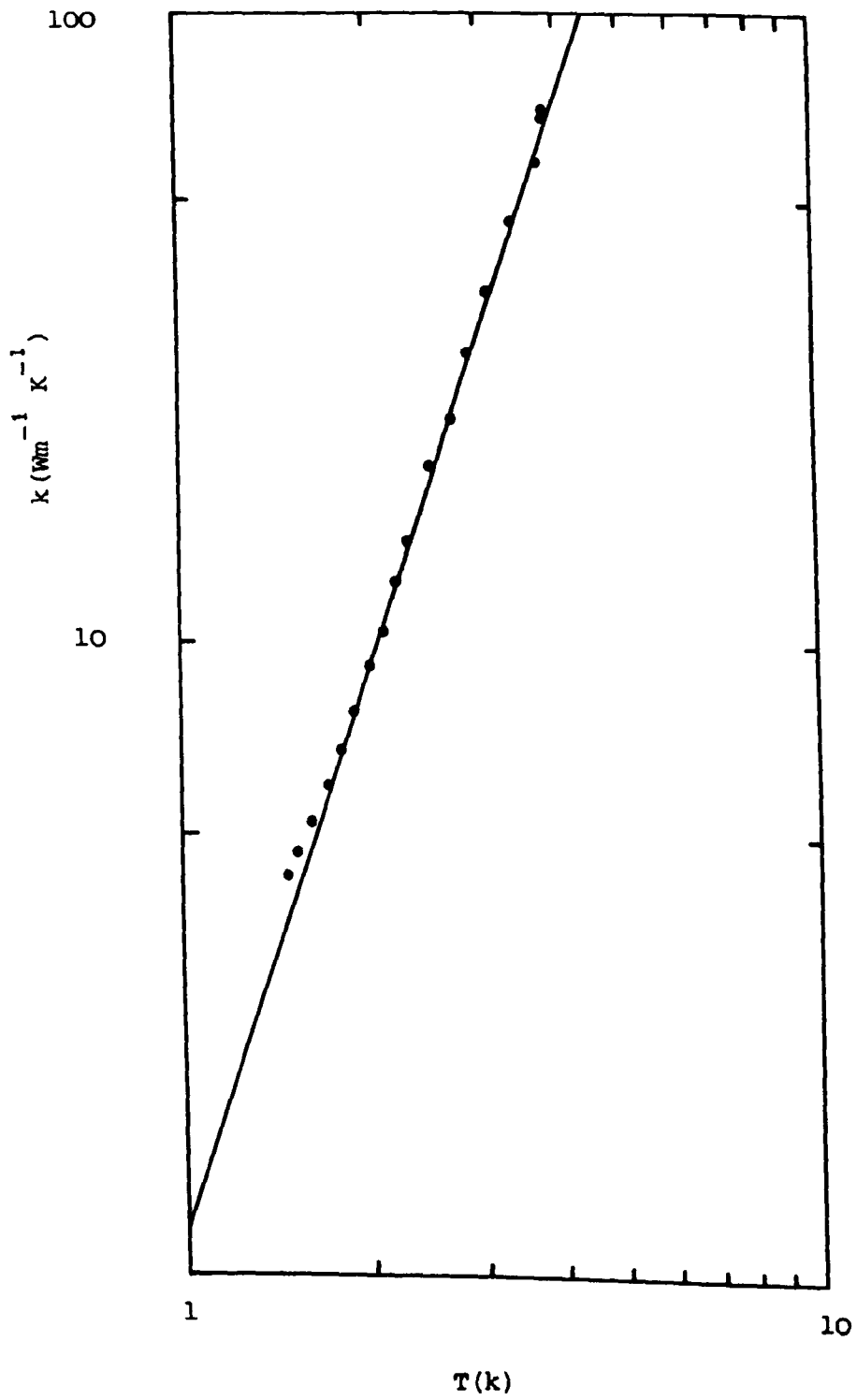


Figure 6.1: Thermal Conductivity of Si(B) in the range 1.0 - 4.2 K

wavelengths become larger than the length scale associated with the surface roughness and/or defects present in the surface. This is a difficult problem to treat theoretically due to the many types of defects that can be present in the surface of the samples. For the samples used the difficulty is increased by the different treatments received by the surfaces. The upper face is etched to a very shiny finish to allow the fabrication of good defect free devices, the lower face has a matt face produced from cutting the substrate from the boule, and the edges are very rough from dicing the samples from the substrate. Thus, it can be assumed that as the temperature is decreased (increasing the average phonon wavelength) specular reflection of the phonons begins to occur on the upper face initially and then eventually on the lower face.

The presence of some specular phonon reflection will reduce the validity of the model presented in Chapter 5 for $T < 1.8$ K as it assumed totally black surfaces with no specular reflection. The results it produced showed that the temperature of an element was strongly determined by the temperature of the few elements directly opposite. With specular reflection occurring, elements further away, and elements on the same face will also affect the final temperature obtained. This will not affect the comparative results presented in Chapters 5 and 6 as the experiments were performed with a substrate temperature of 1.75 K and so specular reflection can be neglected.

6.2 DEVICE CHARACTERISATION

To enable analysis of the results obtained using a 2DEG

heater it was necessary to measure the threshold gate voltage, V_t , of the 2DEG and to determine the variation of carrier concentration as a function of gate voltage. V_t was obtained at $T = 77$ K from measurements of the variation in the conductivity as a function of V_g . Figure 6.2 shows a typical result and the threshold voltage is clearly visible. All the devices used had $V_t = 0.6 \pm 0.1$ V.

To determine the variation of n_s as a function of V_g measurements were made of the source-drain resistance as a function of V_g in a large constant magnetic field. Figure 6.3a shows the resulting SdH oscillations for $B = 6$ T. The adjacent peaks in the SdH oscillations give ΔV_g , and by using equation (3.10) the value of C_{OX} can be obtained. This value is used in equation (3.7) to give an expression relating n_s to V_g . To check the results, measurements were made at several magnetic fields leading to the fan diagram of the SdH oscillation peaks shown in Figure 6.3b. This diagram essentially plots the movement of the Landau levels with magnetic field and by extrapolation to zero field provides an alternative method of obtaining V_t . The results obtained this way give $V_t = 0$ V \pm 2 V. From C_{OX} and ϵ_r (SiO_2) we obtain the thickness of the oxide layer to be 800 nm \pm 50 nm agreeing well with the nominal value of 800 nm.

6.3 ZERO MAGNETIC FIELD RESULTS

6.3.1 Phonon Emission Experiments

Figure 6.4 shows a schematic diagram of the experimental arrangement. In the first experiments heat was introduced into the

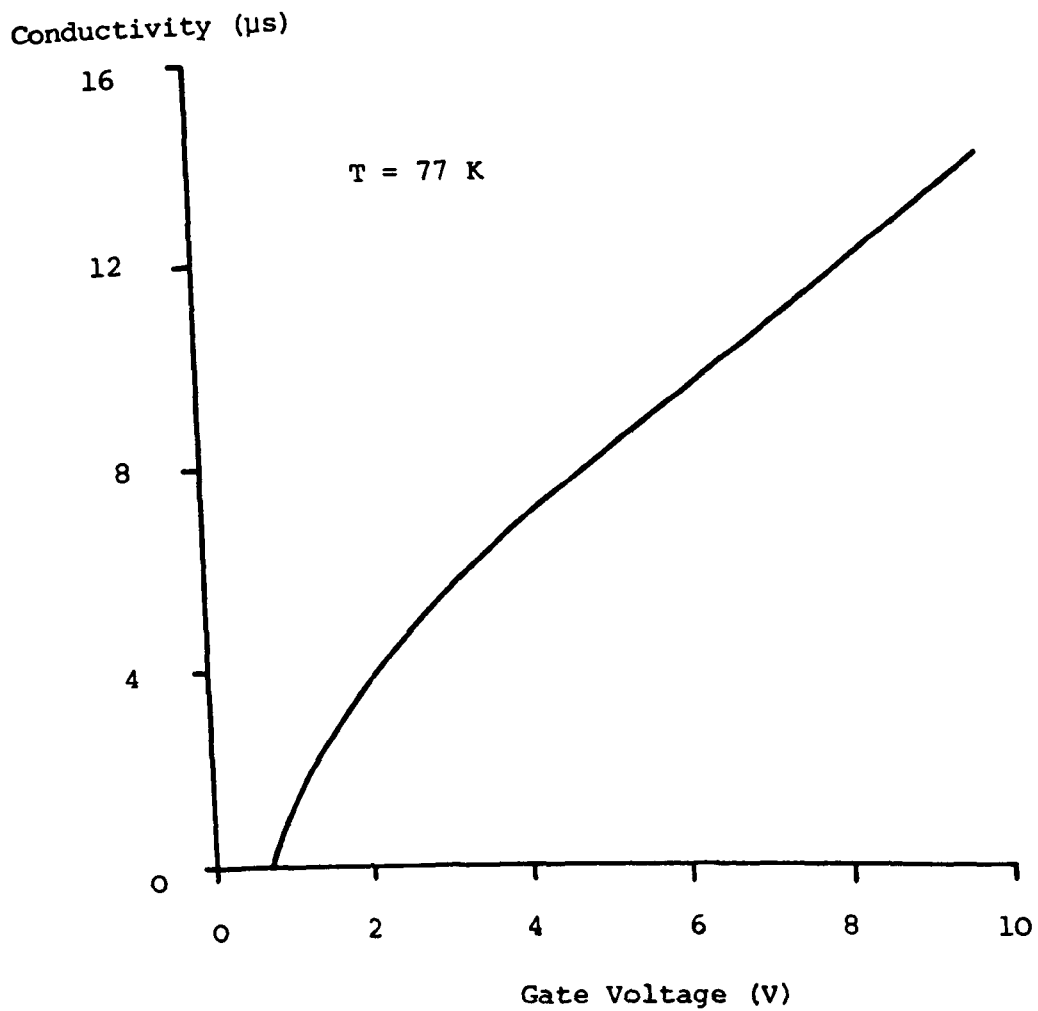


Figure 6.2: Device Conductivity as a Function of Gate Voltage

Resistance per square (Ω)

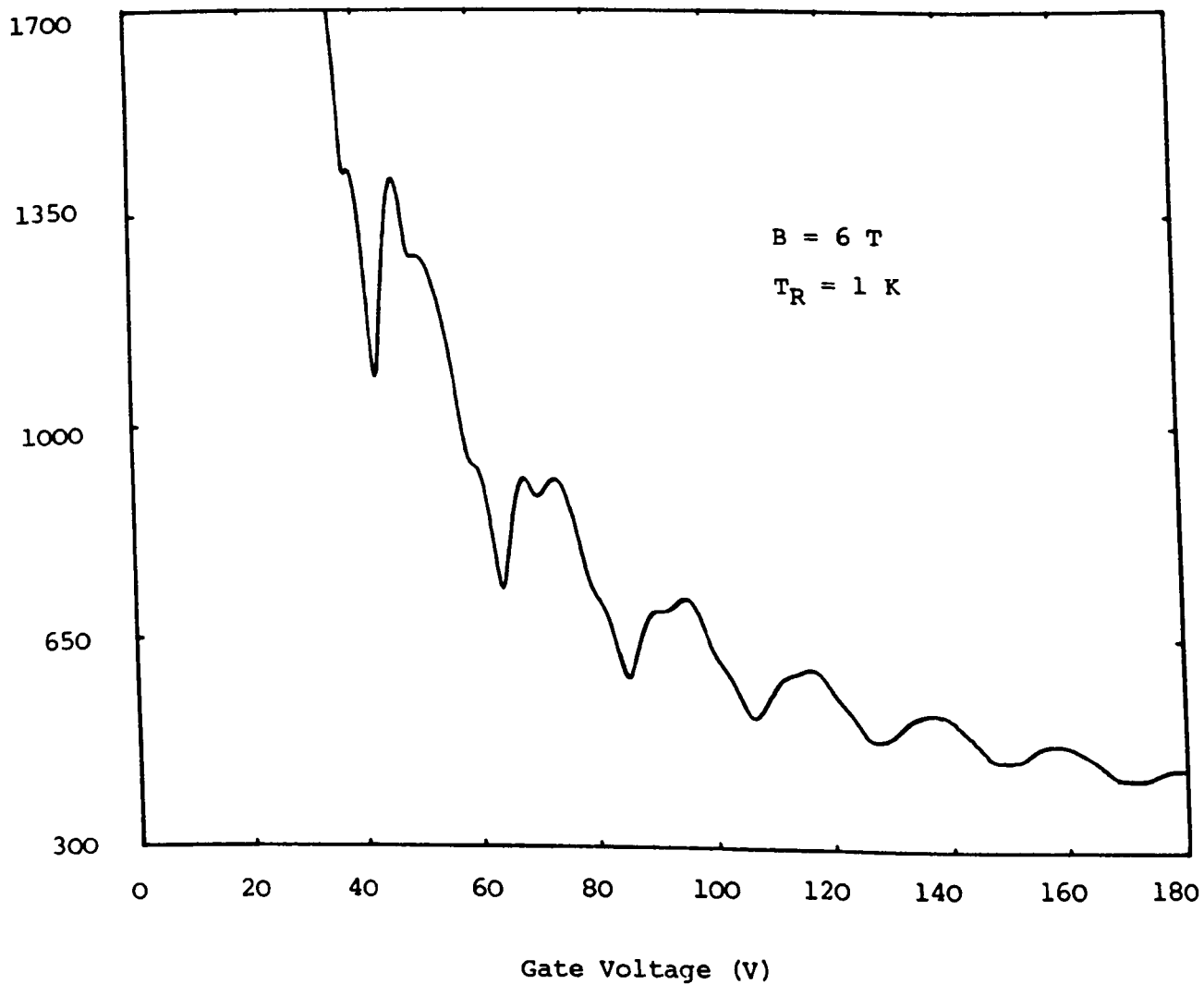


Figure 6.3a: Typical Shubnikov-de-Haas Data

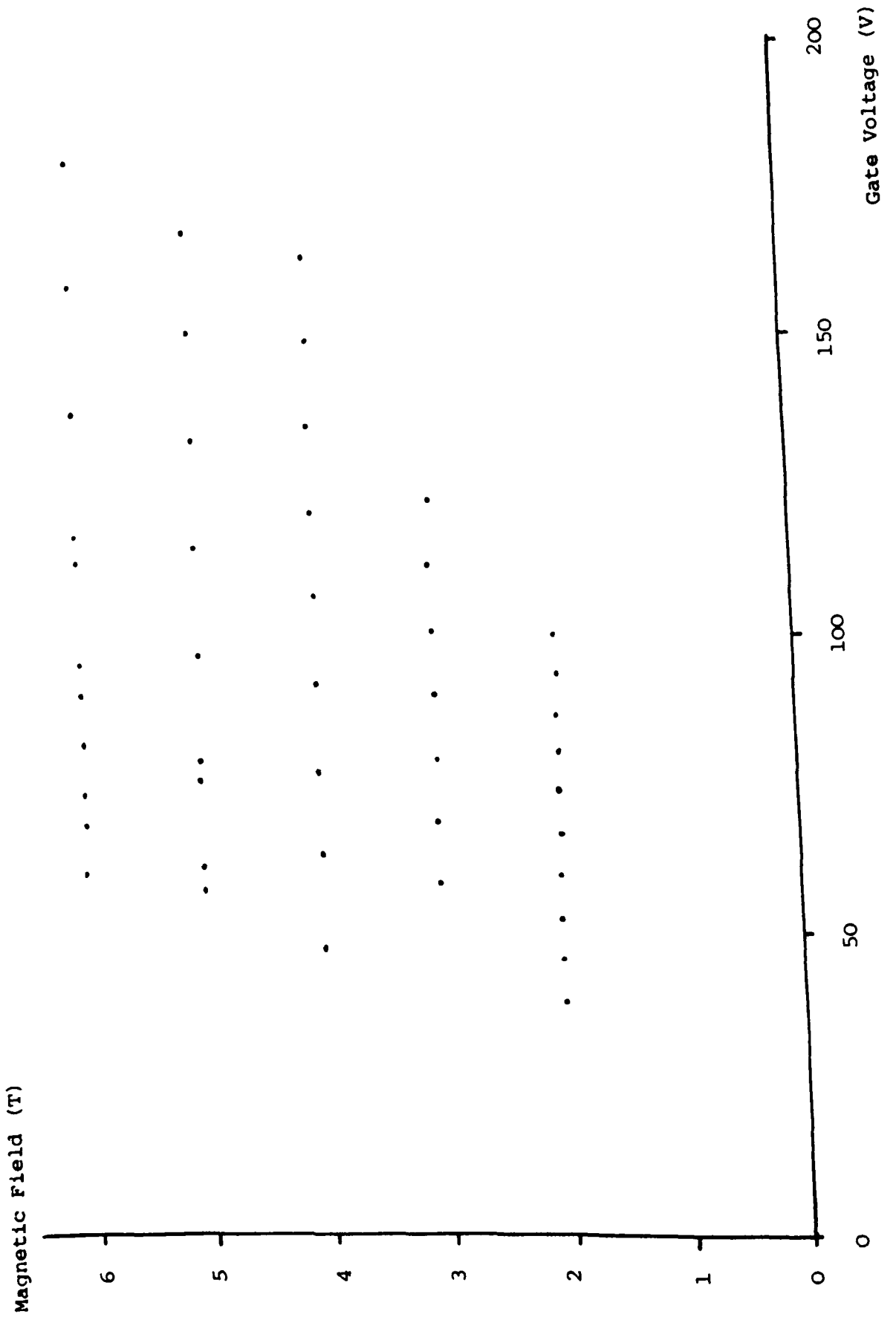


Figure 6.3b: Fan Diagram showing position of Landau Levels

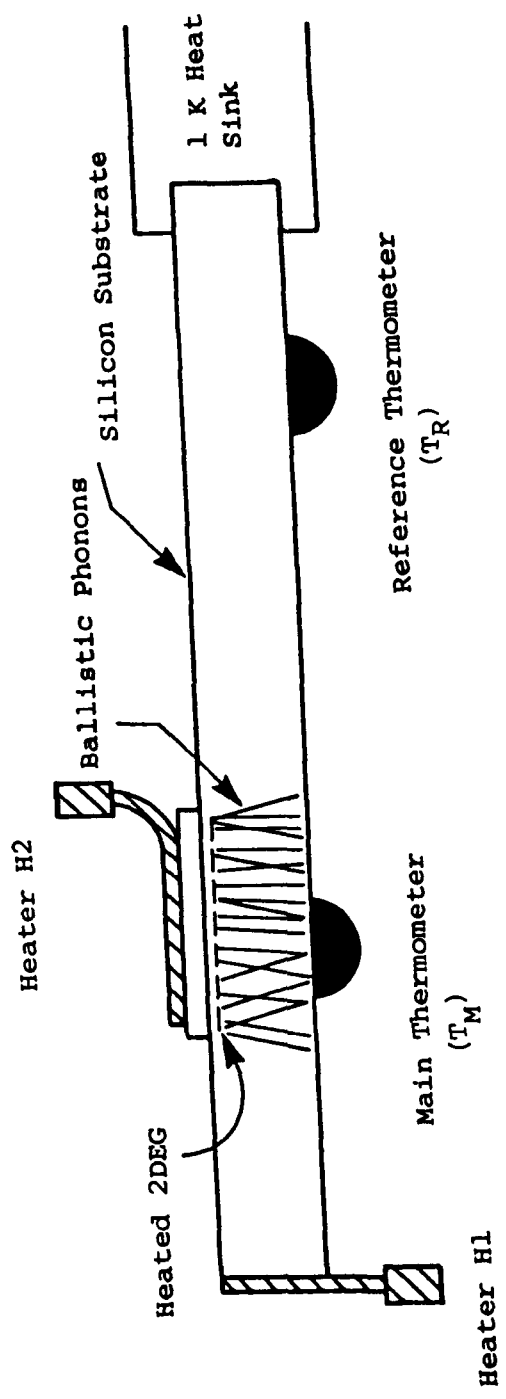


Figure 6.4: Schematic Diagram of Experimental Arrangement

sample either by the 2DEG situated in the centre of the sample, or by a resistive heater (H1) situated at the end of the sample. Using H1, values of the thermal conductivity were obtained which were identical within the experimental error to those of the "as received" substrates. This shows that the processing required for the fabrication of the MOSFETs did not significantly alter the phonon scattering in the substrate.

Comparing the temperature difference, ΔT , between T_M and T_R developed for identical power inputs into H1 and the 2DEG, it was found that for the 2DEG, ΔT was 30% greater. This compares well with the difference of 36% predicted by the computer simulation (this depends to a small degree on the angular phonon emission from the 2DEG assumed). In a later experiment with a resistive heater (H2) situated on the gate of the device, the temperature difference for heat injected via the 2DEG was again 30% greater. This does not agree with the computer simulation which predicted a difference of a few percent between a completely isotropic heater and a heater with tightly coned emission. As discussed in Chapter 5, this discrepancy arises from the inability of the model to cope with phonon focussing in this situation due to the heat flow in the y-direction. For the isotropic heater, heat energy will be channelled in the favoured directions to produce the focussing patterns shown in Figure 4.4 along each of the principal $\langle 100 \rangle$ axes. Figure 5.6 shows that this will predominantly channel heat along the $[001]$ direction towards the thermometer situated directly underneath, in the $[100]$ and $[010]$ directions away from the heat sink, and in the $[\bar{1}00]$ and $[0\bar{1}0]$ directions towards the heat sink. The heat that is channelled towards the heat sink will effectively "miss" the thermometer

situated directly underneath and reduce the measured temperature gradient. In a very crude approximation, with the heat flux split evenly among the principal axes, and T_M collecting all the heat directed towards it, 30% of the phonon flux will "miss" the thermometer.

The difference quoted above between the temperature gradients developed by the resistive heaters and the 2DEG actually depend upon the gate voltage applied to the 2DEG. Figure 6.5 shows the variation in the temperature of T_M (measured relative to $T_R = 1.75$ K) with gate voltage for three different power inputs to the 2DEG (T_R is kept constant for the three different power inputs to the 2DEG by using the auxiliary heater on the sample stage). As V_g is varied the power dissipated in the 2DEG is kept constant by the computer controlled feedback system. The results show three distinct regions. Considering region B, it is apparent that reducing the gate voltage from 180 V to 40 V causes the temperature of T_M to rise by 1.9% for $P = 67 \mu\text{W mm}^{-2}$. This agrees well with the increase in the temperature of T_M predicted by the computer simulation in Chapter 5 where a comparison between an isotropic heater and a heater only emitting phonons normal to the surface predicted an increase in T_M of 1.5%. To calculate the half angle, θ , for the cone of phonon emission in the experiments, it is necessary to know the energy of the phonons emitted. If we assume that the majority of the phonons emitted correspond to the energy of the peak in the electron energy distribution, and that $T_e = 6$ K (obtained from the electrical measurements presented later in this Chapter), we can calculate the variation of θ as a function of gate voltage for TA and LA phonon emission, and this is shown in Figure 6.6.

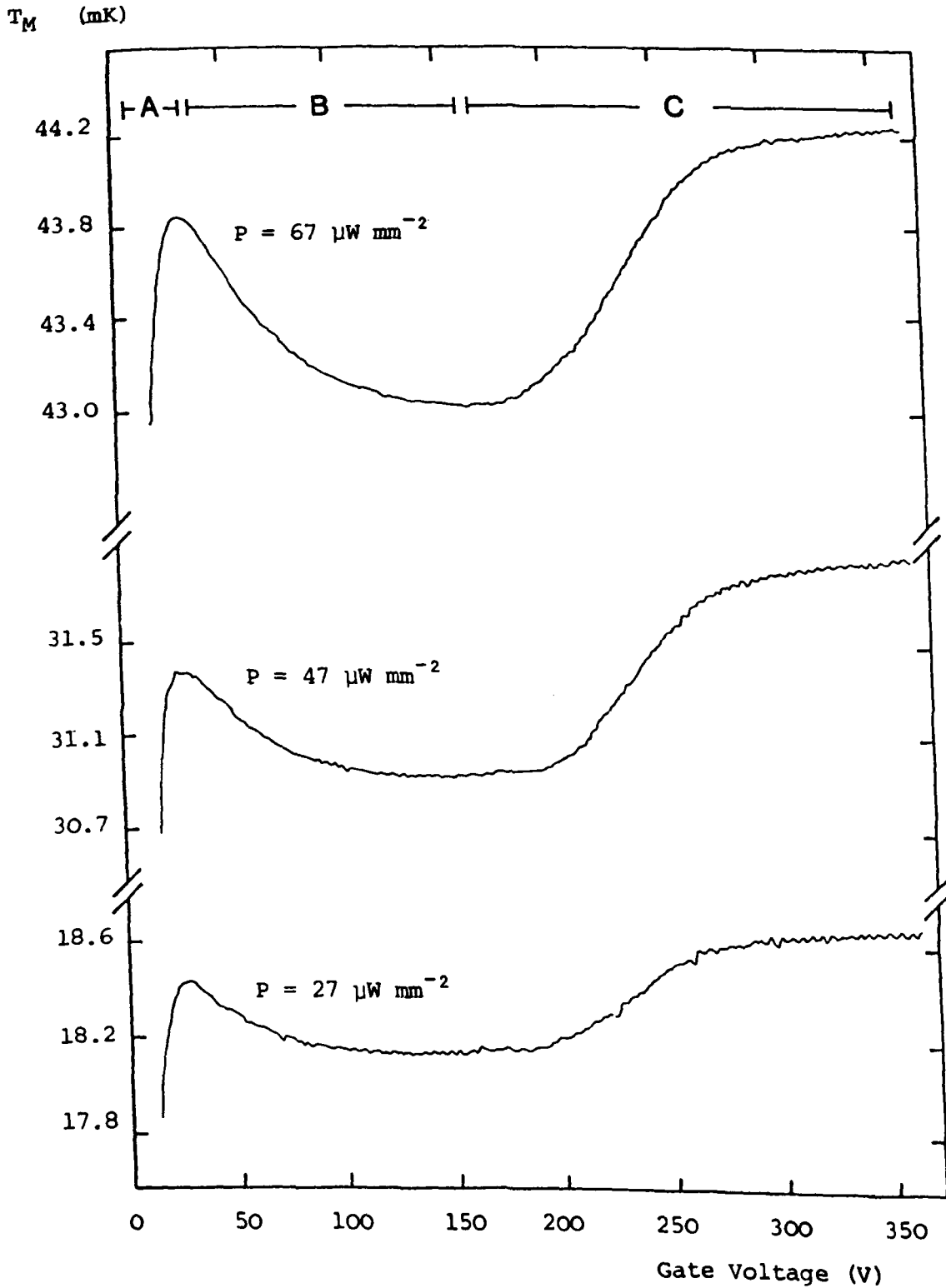


Figure 6.5: Variation of the Temperature of T_M (measured relative to $T_R = 1.75$ K) as a function of gate voltage.

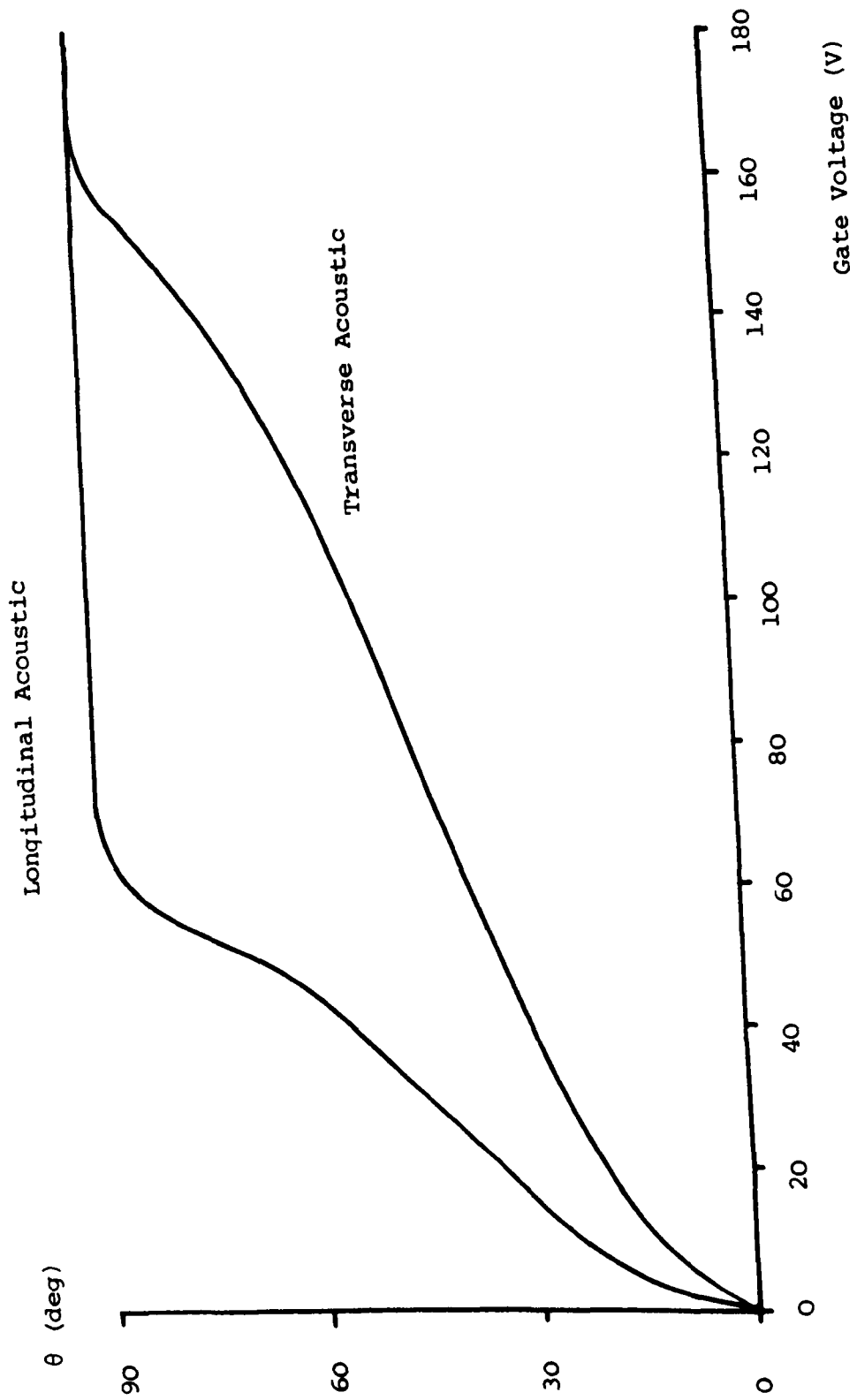


Figure 6.6: Phonon Emission Angle Imposed by $2k_F$ Cut-off as a Function of Gate Voltage

Altering the gate voltage also has the effect of changing the width (thickness), a , of the 2DEG and from equation (4.9) it is apparent that this will alter the restriction on q_z . Ando et al (1982) use a variational method to obtain a , and by following their calculations for $\rho = 1000 \text{ } \Omega\text{cm}$, we obtain the results shown in Figure 6.7. The surprisingly large change in the width of the 2DEG arises from the very low depletion charge concentration for these high resistivity samples. This also produces a depletion layer thickness approximately ten times larger than for samples with $\rho = 10 \text{ } \Omega\text{cm}$. The increase in the width of the 2DEG with decreasing gate voltage will restrict q_z with the cut-off given approximately by $q_z \sim a^{-1}$. Thus, at low gate voltages q_z is restricted by two mechanisms and these two restrictions combined give a maximum phonon momentum that can be emitted. We can write this maximum phonon momentum as

$$q_c^2 = q_z^2 + q_{\parallel}^2 \approx a^{-2} + (2k_F)^2 \quad (6.1)$$

and converting this into a frequency cut-off, ν_c , using the phonon velocities $v_l = 9.33 \times 10^3 \text{ ms}^{-1}$ (LA) and $v_t = 5.4 \times 10^3 \text{ ms}^{-1}$ (TA) (Suzuki and Mikoshiba 1971a), we can calculate the variation of ν_c as a function of gate voltage. This is shown in Figure 6.8. Comparing this with the dominant phonon frequency of 480 GHz for $T_e = 6 \text{ K}$, it is apparent that for $V_g < 50 \text{ V}$ the TA phonon emission is being severely constrained.

Region A in Figure 6.5 shows that the increase in the temperature of T_M relative to T_R as a function of gate voltage

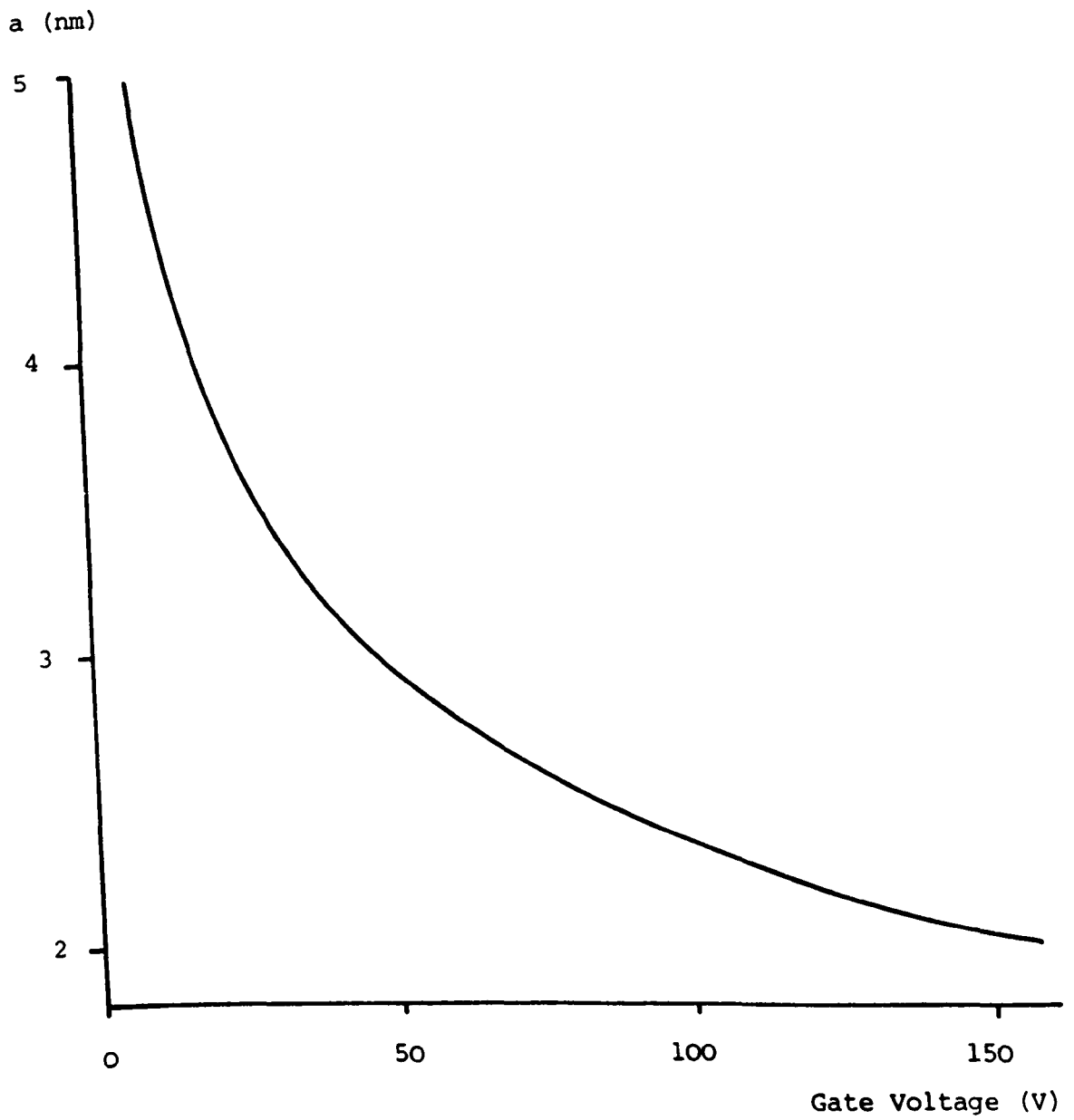


Figure 6.7: Variation of the 2DEG Width as a Function of Gate Voltage

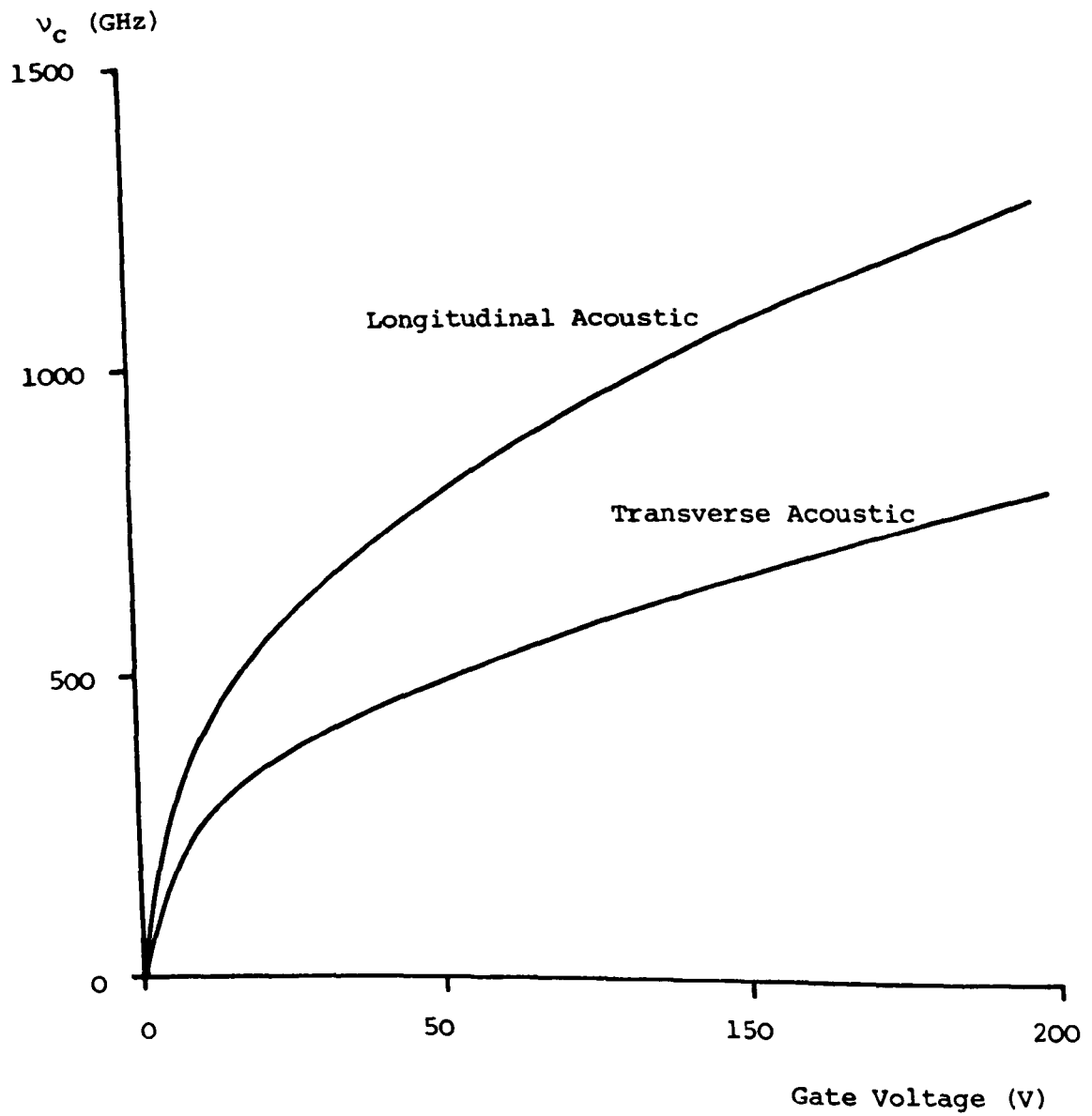


Figure 6.8: Variation of the Frequency Cut-off Imposed by the $2k_F$ Cut-off and the a^{-1} Cut-off as a Function of Gate Voltage

reaches a maximum, and then falls rapidly. This is a surprising result if only the $2k_F$ cut-off is considered as it would be expected that T_M would continue to rise, or perhaps saturate at some value of V_g when all the phonon emission is restricted to angles very close to the normal to the plane of the 2DEG. An explanation of this effect is that for low gate voltages the $2k_F$ cut-off is reducing the ability of the 2DEG to cool by limiting the phonon modes available. Thus, for constant input power the electron temperature will rise with decreasing V_g , increasing the dominant frequency of the emitted phonons. If the rise in electron temperature was sufficient, isotope scattering, which becomes important for $\nu > 1500$ GHz in this sample, could begin to scatter an increasing proportion of the phonons emitted, so reducing T_M . However, Figure 6.8 shows this cannot occur because the inclusion of the q_z restriction limits the maximum phonon frequency emitted to well below the isotope scattering regime. It also has the effect of further reducing the cooling efficiency of the 2DEG, and so quite modest input powers will heat the electrons significantly at low values of n_s .

The electrical data presented in section 6.3.2 produces an electron temperature of $T_e \approx 6$ K for $P = 67 \mu\text{W mm}^{-2}$ at $V_g = 150$ V. Since the experiments are performed at constant power we know that the area under the emitted phonon energy distribution must remain constant. By noting that equation 4.21 can be rewritten as a function of $\omega_q N_q(T_e)$ and functions of q_z and q_{\parallel} which are constant except near their cut-offs (F W Sheard private communication) we obtain,

$$P = \int_0^{\nu_c} \frac{\nu^4}{\exp((h\nu/kT_e) - 1)} d\nu \quad (6.2)$$

and by evaluating equation (6.2) numerically over the limits determined by the cut-off frequency, ν_c , shown in Figure 6.8, it is possible to calculate the electron temperature, assuming only TA or only LA phonon emission, as a function of gate voltage. This is shown in Figure 6.9. It is interesting to note that the low gate voltage turnover in the temperature of T_M , in Figure 6.5, occurs between the sudden increase in T_e for the TA and LA phonon emission cases. This calculation makes it apparent that for $20 \text{ V} \leq V_g \leq 60 \text{ V}$ LA phonon emission may become a more favourable mechanism for energy loss.

Some earlier work (Newton, 1987) supports this conclusion though the experimental conditions are rather different than those assumed in the calculation. Newton presented heat pulse data showing the proportion of LA and TA phonon emission from a heated Si MOSFET using a CdS bolometer mounted on the opposite face of a silicon substrate. The bolometer detected emission from 20° to 40° to allow the measurement of LA and TA emission. The data show the proportion of LA emission rising from approximately 30% to 55% with decreasing gate voltage. Direct comparison of the heat pulse data with our experiments is difficult as the power dissipated in the 2DEG is very much higher ($\sim 0.5 \text{ W mm}^{-2}$) to obtain a sufficient signal on the bolometer, and the power does not stay constant as the gate voltage is altered (source-drain voltage constant). However, it seems reasonable to assume from Figure 6.9, and the heat pulse data, that more LA emission is occurring at the lower gate voltages. Figures 6.6 and 4.4 show that the LA phonons are not constrained to such a narrow cone of emission as the TA phonons, and are not as

Electron Temperature (K)

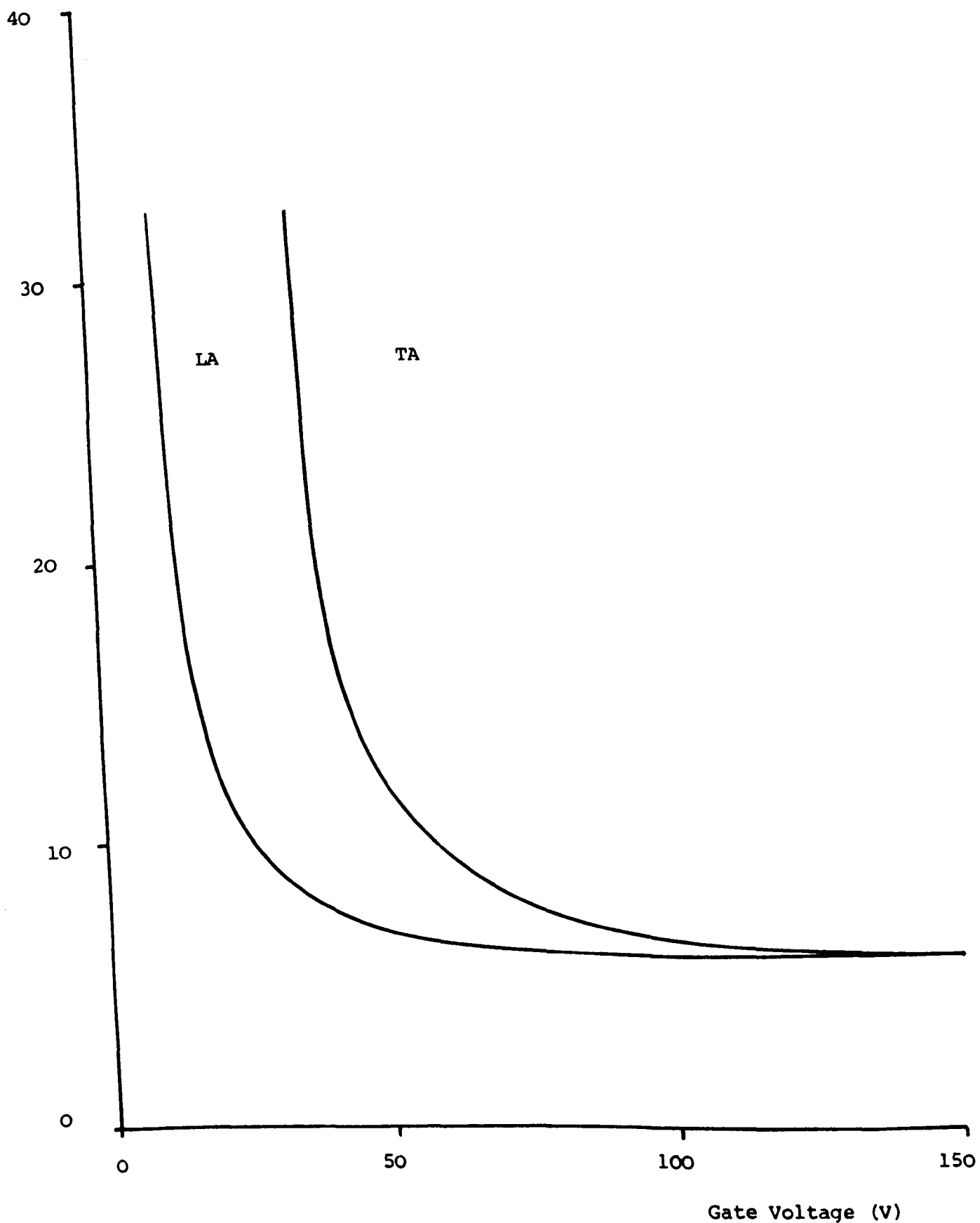


Figure 6.9: Variation of the Calculated Electron Temperature as a Function of Gate Voltage at Constant Power

strongly focused in the direction of the thermometer. Additionally, equation (4.4) shows that the LA phonons cannot be emitted normal to the plane of the 2DEG but can be emitted at larger angles since $\chi_g \neq 0$ for $\theta = 90^\circ$, unlike χ_t (see section 4.1.1). Thus, it is proposed, that the fall in the temperature of T_M seen at low gate voltages (Figure 6.5 region A) is due to increased LA phonon emission.

For gate voltages less than 15 V the constraints on the LA phonon emission are also becoming severe and the resulting increase in electron temperature may produce optical phonon emission and/or far infra-red (FIR) emission. The experimental arrangement allows the FIR emission to be monitored with the reference thermometer, T_R , as the temperature of this thermometer is solely determined by the phonon flux passing along the sample (and any small amount of FIR absorbed by the sample). So if the temperature of T_R drops it indicates that some of the device power is being emitted as FIR. Calibrating T_R against the device power allows the percentage of the FIR emission to be determined quantitatively, and results for two device powers are shown in Figure 6.10. Appreciable FIR emission is occurring for $V_g < 15$ V and by using Stefan's law we can calculate the electron temperature approximately. For $P = 67 \mu\text{W mm}^{-2}$ and $V_g = 5$ V this yields $T_e = 75$ K. This is below the value predicted by the calculations presented in Figure 6.9 for this V_g but we have ignored optical phonon emission which will also provide an energy loss mechanism, for $T_e > 50$ K. This will prevent T_e rising as rapidly and so this fits in with the explanation presented.

We next consider region A in Figure 6.5 more closely. It

Phonon Emission

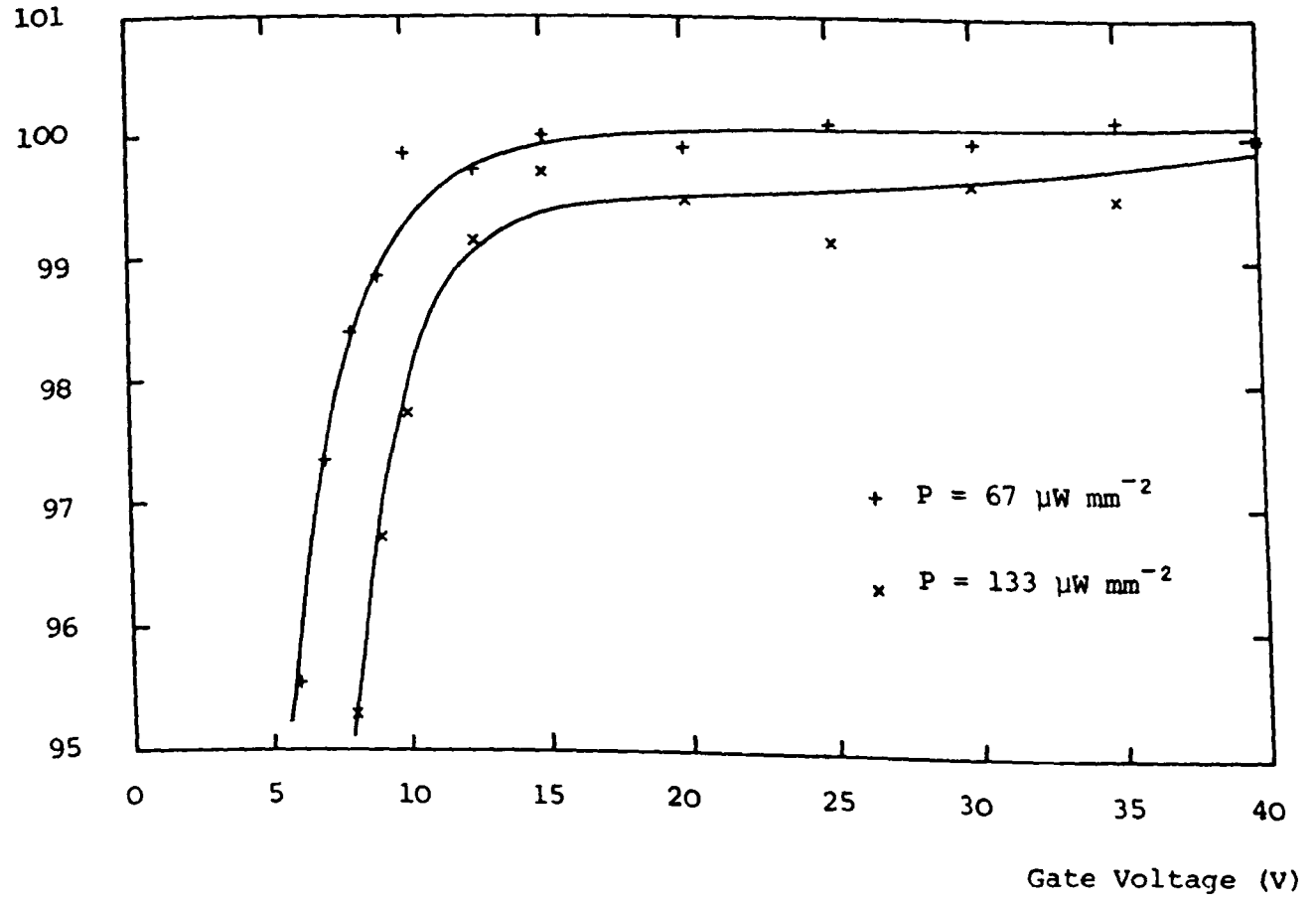


Figure 6.10: Experimental Results Showing FIR Emission at Low Gate Voltages

can be seen that the turnover point in the temperature of T_M is moving to higher gate voltages for higher powers. An investigation of this was performed over a wide range of powers and the results are shown in Figure 6.11. The observation that the turnover point moves to higher gate voltages with increasing power is consistent with the explanation proposed. Presumably, the turnover point corresponds to a particular proportion of the total phonon emission being LA phonons and it is apparent that the gate voltage where the restriction on the TA phonon emission makes the emission of LA phonons favourable will increase with increasing power. Furthermore, considering a device power of $P = 67 \mu\text{W mm}^{-2}$ where the turnover point was measured for three lattice temperatures, T_R , it is apparent that T_R is having very little effect. This indicates that $T_e > T_R$. Intriguingly, the mobility measurements show that the peak mobility occurs at exactly the same gate voltage as the turnover in the temperature of T_M for all the device powers measured. This will be discussed in section 6.3.2.

Figure 6.5 region C shows that T_M also increases for high gate voltages. The increase begins at $V_g = 180 \text{ V}$ corresponding to $n_s = 4.8 \times 10^{12} \text{ cm}^{-2}$. Rothenfusser et al (1987) saw anomalous effects in their heat pulse data for $n_s > 4.0 \times 10^{12} \text{ cm}^{-2}$ working with $\rho = 300 \Omega\text{cm}$ samples, which they attributed to the filling of an upper subband.

The calculation of the energies of upper subbands is a difficult problem due to their self-consistent nature, and calculating how the energies change with applied gate voltage is very time consuming. Howard and Fang (1976) performed calculations for four

Gate Voltage (V)

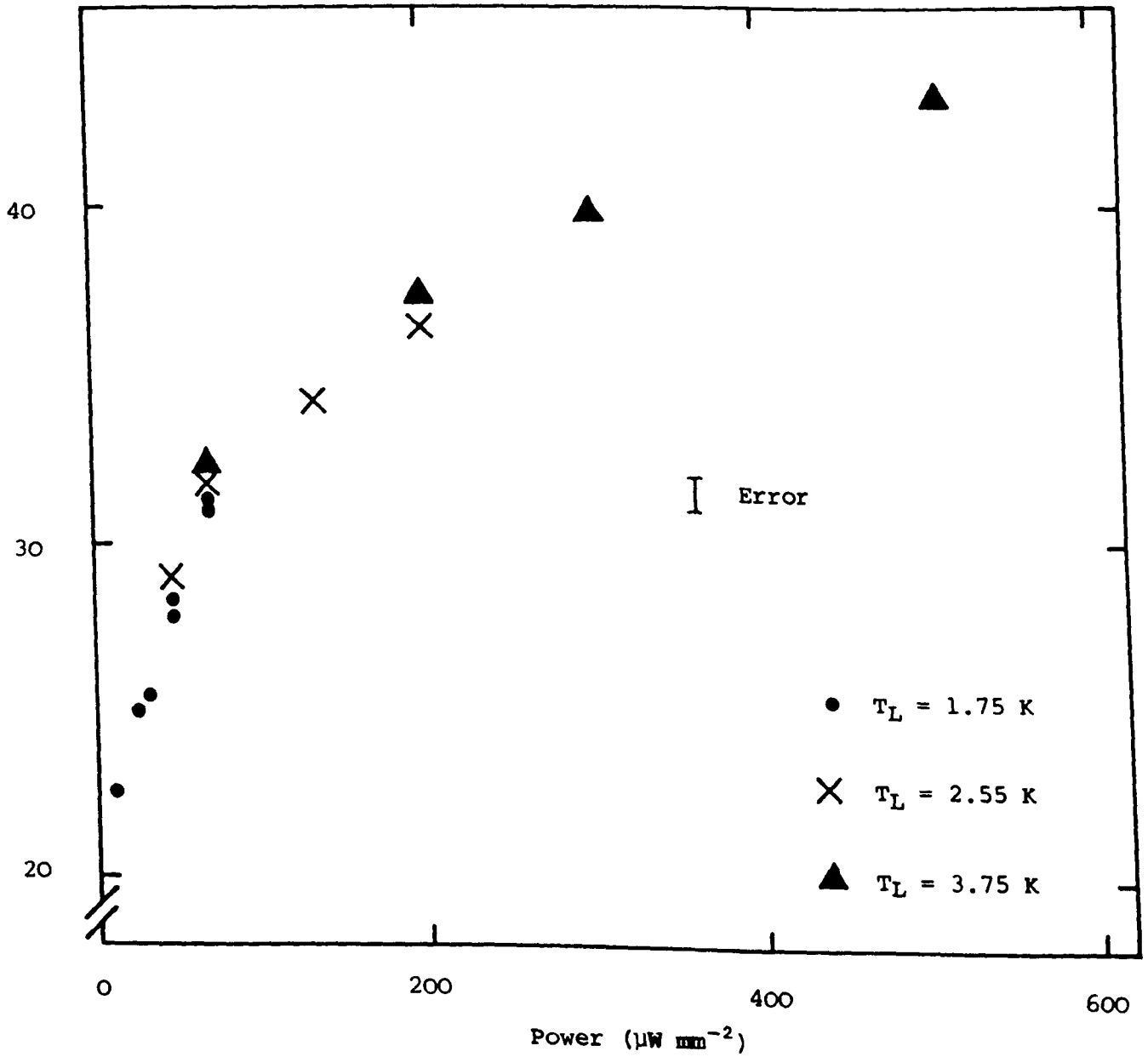


Figure 6.11: Variation in the Position of the Peak Mobility seen during the Thermal Experiments as a Function of Device Power

substrate resistivities up to $\rho = 100 \text{ } \Omega\text{cm}$. Extrapolating their theoretical results to $\rho = 1000 \text{ } \Omega\text{cm}$ shows that the upper subband begins to be populated for $n_s > 1.7 \times 10^{12} \text{ cm}^{-2}$. Howard and Fang also observed the population of the upper subband experimentally by accurately determining the period of SdH oscillations to measure the density of states. Extrapolating these measured values indicates that the upper subband in $\rho = 1000 \text{ } \Omega\text{cm}$ samples will become populated for $n_s > 3.0 \times 10^{12} \text{ cm}^{-2}$. Unfortunately the extrapolation of this experimental data is very inaccurate as they could only measure the population of the upper subband in samples with $\rho \leq 8.5 \text{ } \Omega\text{cm}$. In a $\rho = 100 \text{ } \Omega\text{cm}$ sample they failed to detect any change in period of the SdH measurements. Howard and Fang's theoretical calculations explain this failure by showing that the very different electronic wavefunctions and, hence, different charge distribution, for electrons in an upper subband alters the confining potential and that this alteration of the confining potential causes the energy of the subband to increase as population of the upper subband begins. Howard and Fang also show that for high resistivity samples, this increase in subband energy only allows the Fermi level to move very slowly up the band producing very small changes in the period of the SdH oscillations. During the experiments on our samples an investigation was undertaken using AC techniques to accurately measure the source-drain resistance. This techniques allows the SdH oscillations, and the first derivative of the SdH oscillations, to be measured. However, no change in period could be seen.

The filling of the upper subband will cause the observed rise in the temperature of T_M from the very tightly coned emission from the small Fermi circle or ellipse (depending upon which subband

is being occupied) of the upper subband. Thermal broadening as T_e rises, ie for higher powers, should cause the population of the upper subband to start at lower n_s but surprisingly this is not seen. It is, perhaps, possible that the increase in the energy of the upper subband as population commences may provide a feedback mechanism reducing this effect.

Comparing region C and region A of Figure 6.5 it is very interesting that T_M reaches a higher temperature for the upper subband filling than at low n_s even though, presumably, the diameter of the Fermi circles concerned in the two cases are similar. This may reflect the absence of the q_z cut-off for the upper subband situation or, perhaps, the fact that there are two bands emitting.

6.3.2 Electrical Transport Experiments

Electrical measurements were undertaken to determine the electron temperatures during the phonon emission studies. These measurements were limited to two-terminal measurements by the absence of Hall probes on the samples used and this will introduce a small error in the results $< 0.5\%$. A further problem was that the device characteristics at low gate voltages could change by 4% for no apparent reason. These changes would only occur two or three times during an experimental run of six weeks, and so generally the problem could be overcome.

To calibrate the electron temperature, DC measurements of the device resistance for a range of gate voltages using very low currents ($I_{sd} = 1 \mu A$) at various substrate temperatures were

performed. The temperature of the substrate was controlled with the auxiliary heater, and varied from 1 K (base temperature) to 30 K. Using this calibration the electron temperature can be determined from the device resistance measurements made during the phonon emission experiments and Figure 6.12 shows the results obtained for three powers (we note that this procedure assumes that the resistance only depends on the electron temperature and is wholly independent of the lattice temperature). The scatter seen at the higher gate voltages arises from the small variation of resistance with temperature at these carrier concentrations.

The decrease in electron temperature seen at low gate voltages is very surprising and contrary to the explanation given in section 6.2.1. A possible explanation is that the source-drain resistance is affected by localisation in this region making it dependent on the lattice temperature as well as the electron temperature. Thus, it is necessary to look at the electrical characteristics of the devices in detail.

Figure 6.13 shows measurements of the device mobility as a function of gate voltage at a substrate temperature of 1 K for different applied source-drain voltages. To simplify this diagram, data for $V_{sd} = 1$ mV and 5 mV have been neglected as the data lie very close to the $V_{sd} = 0.5$ mV data. This indicates that the $V_{sd} = 0.5$ mV data corresponds to negligible electron heating. The increase in the mobility with increasing source-drain voltage shows that "activated" behaviour is present for $V_g < 40$ V ie the mobility increases with T_e . From the high mobility ($\sim 12,000 \text{ cm}^2 \text{ s}^{-1} \text{ V}^{-1}$) and the low threshold voltage (~ 0.6 V) it can be concluded that the

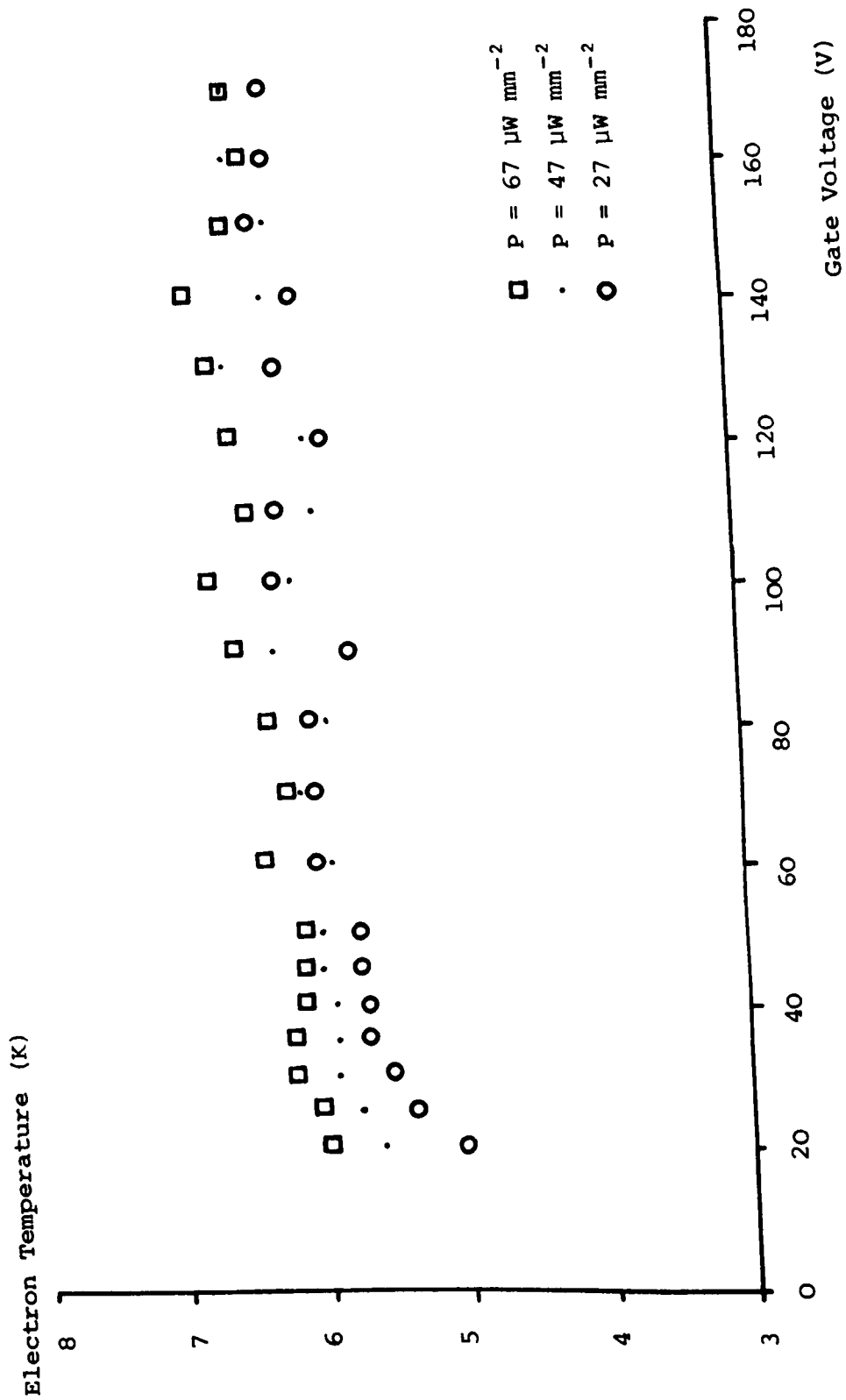


Figure 6.12: Variation of the Measured Electron Temperature with Gate Voltage

Mobility ($\text{cm}^2 \text{s}^{-1} \text{V}^{-1}$)

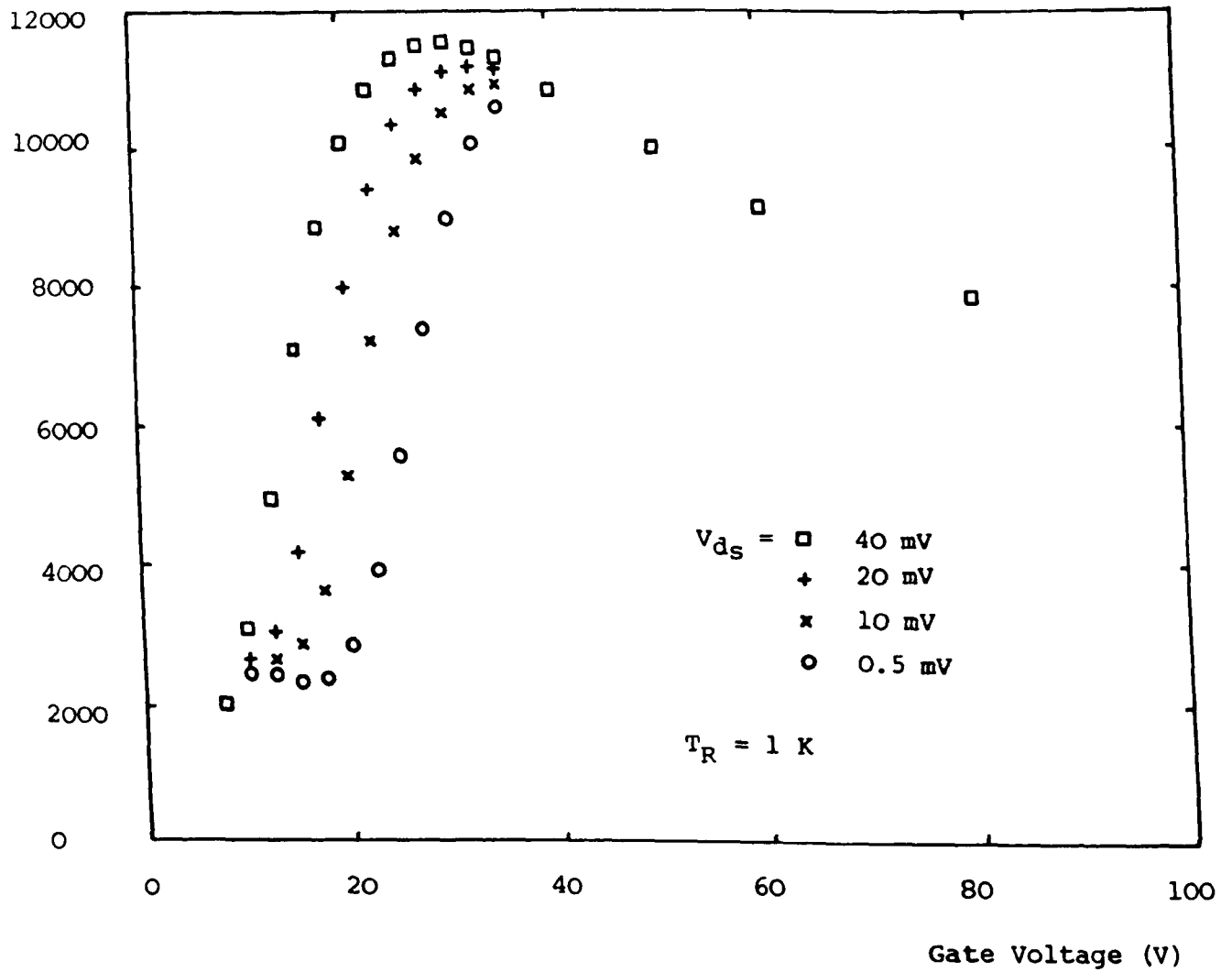


Figure 6.13: Experimental Results Showing the Device Mobility as a Function of Gate Voltage for different Applied Source-Drain Voltages

samples have very low disorder. This indicates that the "activated" behaviour cannot be due to strong localisation as for $T = 1$ K this will only be seen within ~ 0.5 V of the threshold voltage (this value results from the thermal energy available for activation). Thus, the anomalous behaviour must be weak localisation arising from coherent interference of the electronic states. It is interesting that this weak localisation is only seen in the region where long range Coulombic scattering is dominating the elastic scattering implying that there is less backscattering in the region where surface roughness scattering is dominating. It would also be noted that the weak localisation disappears for $V_g < 8$ V and this should be investigated in detail in any future studies.

Figure 6.13 shows that heating the electrons by increasing the applied source-drain voltage, increases the peak mobility and moves it to lower gate voltages. Heating the electrons further causes the opposite to happen with the peak mobility decreasing and the gate voltage corresponding to the peak mobility increasing. This is seen for either heating the electrons by passing a current through the 2DEG, or by raising the temperature of the substrate. Figure 6.14 shows the variation of mobility as a function of lattice temperature. A sensing current of $15 \mu\text{A}$ was used to slightly warm the electrons and reduce localisation effects. These results are very similar to those of Smith and Stiles (1986) who worked with very high mobility samples ($\sim 25000 \text{ cm}^2 \text{ s}^{-1} \text{ V}^{-1}$). They attributed their results to the temperature dependence of the electronic screening of the impurity and surface roughness potentials that cause elastic scattering. These effects are only seen in high mobility samples as the low Dingle temperature resulting from the

Device Mobility ($\text{cm}^2 \text{s}^{-1} \text{V}^{-1}$)

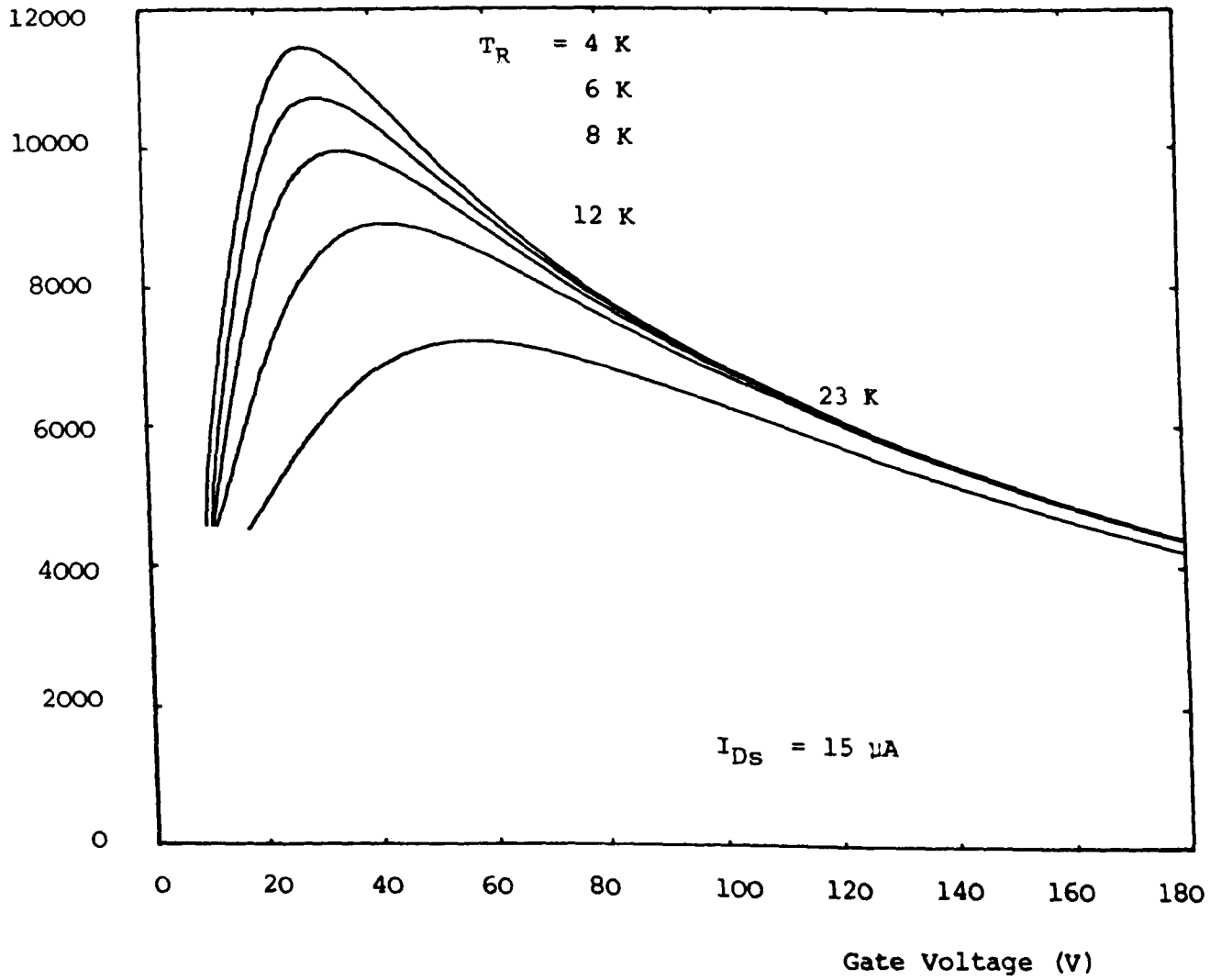


Figure 6.14: Experimental Results Showing the Effect of the Lattice Temperature on the Device Mobility

low disorder means that they are not masked.

Plotting the peak mobility and the gate voltage corresponding to the peak mobility as a function of lattice temperature yields the results in Figure 6.15. It is apparent that for $T_R < 4$ K we are still seeing some localisation effects despite the high sensing current. For $T_R > 4$ K, however, the gate voltage corresponding to the maximum mobility has a linear dependence on temperature which agrees with the data of Smith and Stiles. Using this dependence with the data given in Figure 6.11, which gives the turnover point seen in the phonon emission data as a function of input power, the electron temperature at this point can be deduced. The results obtained broadly agree with the electron temperature calibration shown in Figure 6.12. The dependence of the electron temperature on the input power is $T_e \propto P^{\frac{1}{2}}$, ie $P \propto T_e^2$.

The electrical measurements presented above show that both weak localisation and screening effects are important in the region of the discrepancy between the electron temperatures predicted by the analysis of the phonon emission experiments and the measured electron temperatures (shown in Figure 6.12). Figure 6.16 shows the variation of the device mobility as a function of substrate temperature for a gate voltage of 20 V with different applied source-drain voltages. Clearly for $T_R > 4$ K the weak localisation has been removed and since the electron temperatures measured are above this temperature it seems very unlikely that the discrepancy can be due to localisation effects.

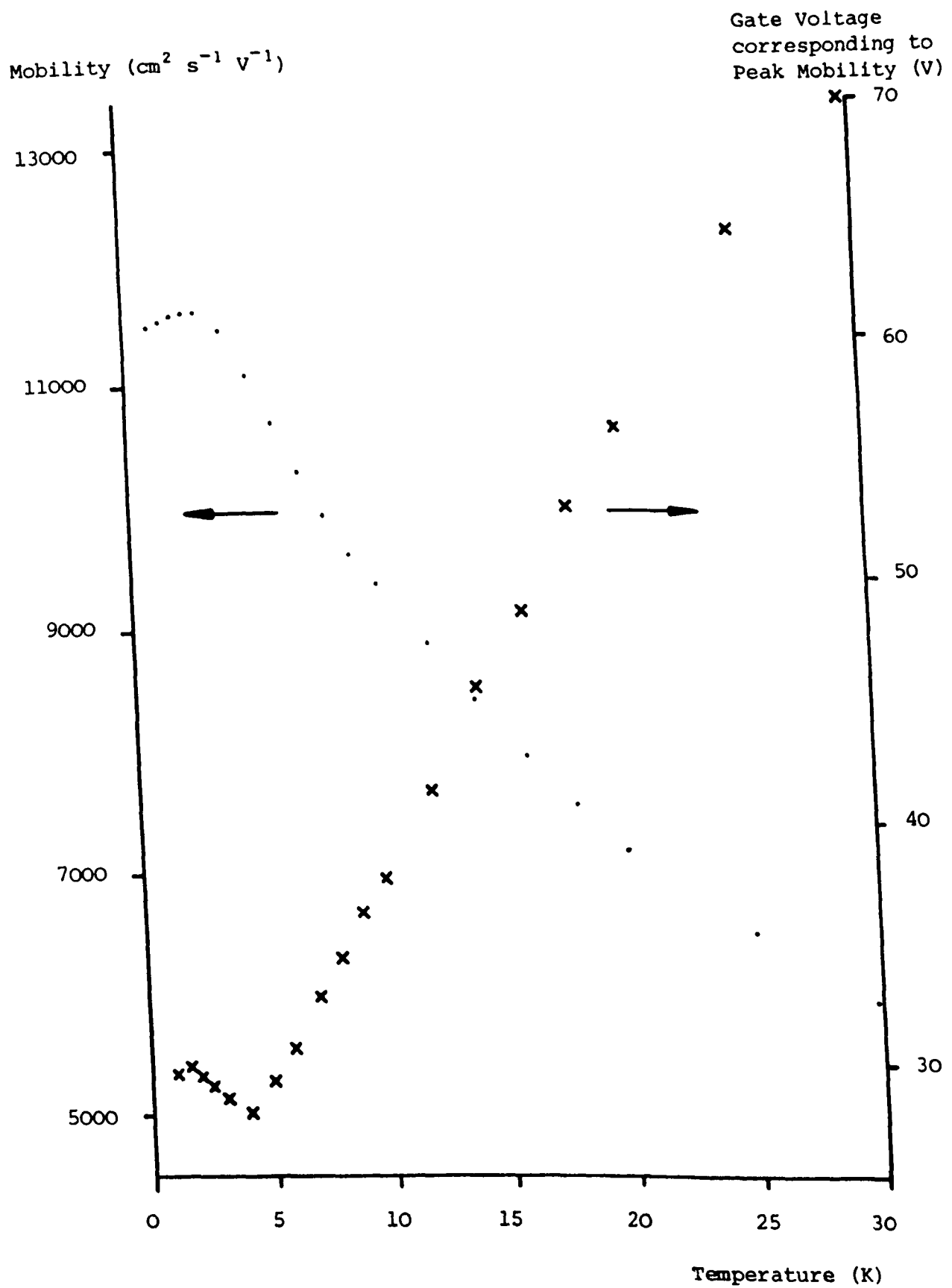


Figure 6.15: Variation of the Peak Mobility and the Gate Voltage Corresponding to Peak Mobility as a Function of Lattice Temperature

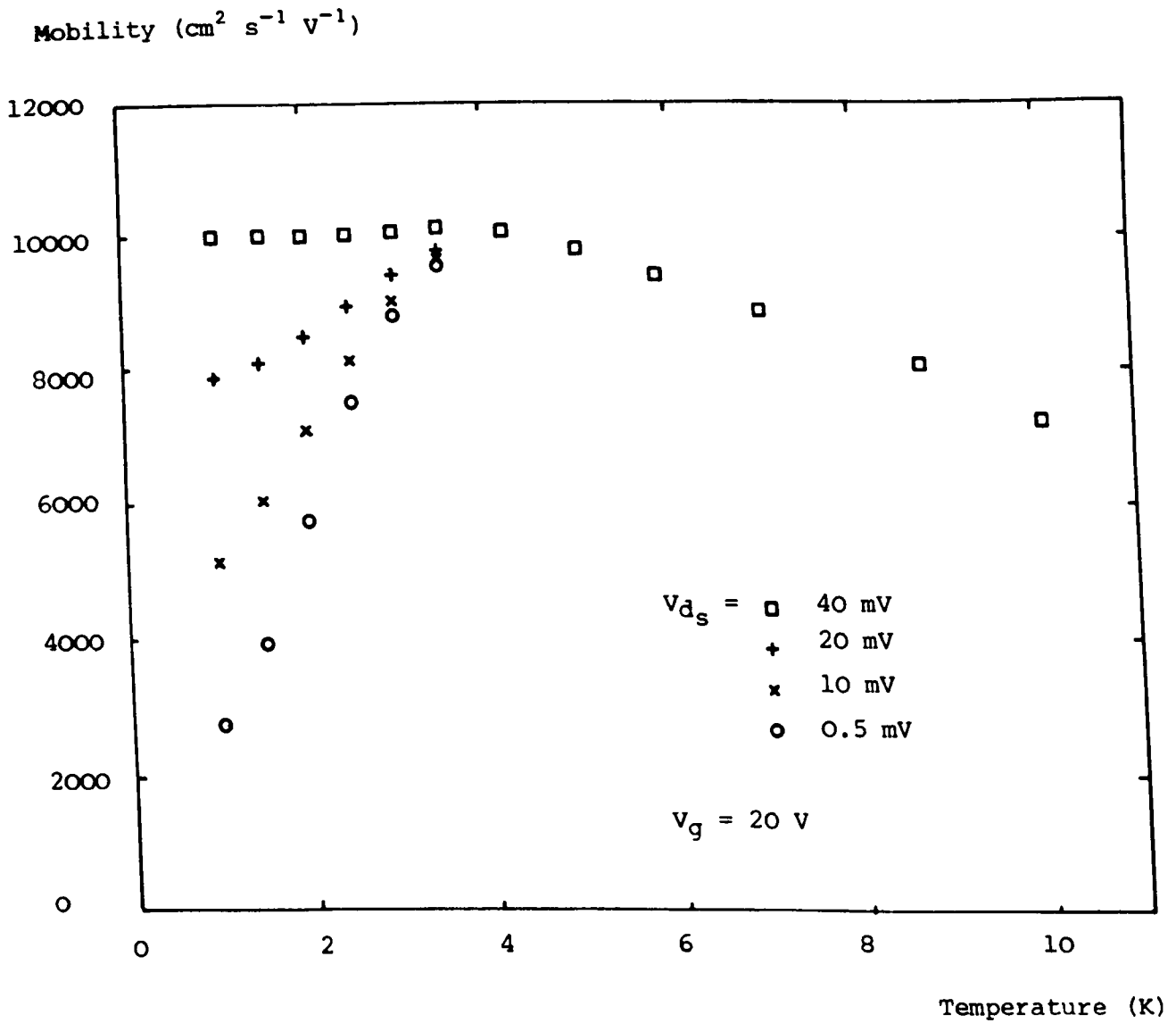


Figure 6.16: Experimental Results Showing the Variation of Device Mobility as a Function of Temperature for Different Applied Source-Drain Voltages

The details of screening are very complex. However, in general, for a given q the screening decreases with decreasing k_F (and, hence, n_3) and also with increasing temperature. The theory of Challis et al (1987) used for the analysis of the phonon emission experiments, neglects screening and predicts that reducing the gate voltage with constant power dissipation will produce a rise in the electron temperature as the number of phonon modes available for dissipation is reduced by the $2k_F$ and a^{-1} cut-offs. Including screening in this analysis may reduce the rise in electron temperature as the reduction in carrier concentration reduces the screening linking the phonon modes available for dissipation more efficiently to the electron system. The temperature dependence of the screening will also help reduce the rise in the electron temperature as any increase in temperature will also increase the cooling efficiency of the electron system.

A further indication that screening is very important comes from the electrical data collected during the phonon emission experiments. This data shows that the peak mobility occurs at exactly the same gate voltage as the turnover in the temperature of T_M measured relative to T_R (Figure 6.5 region A). This could perhaps indicate that the TA and LA phonon emission are being affected differently by the change in screening.

6.4 QUANTISING MAGNETIC FIELD RESULTS

The application of a quantising magnetic field perpendicular to the 2DEG produces the variation in T_M as a function of gate voltage shown in Figure 6.17. For comparison, this figure also

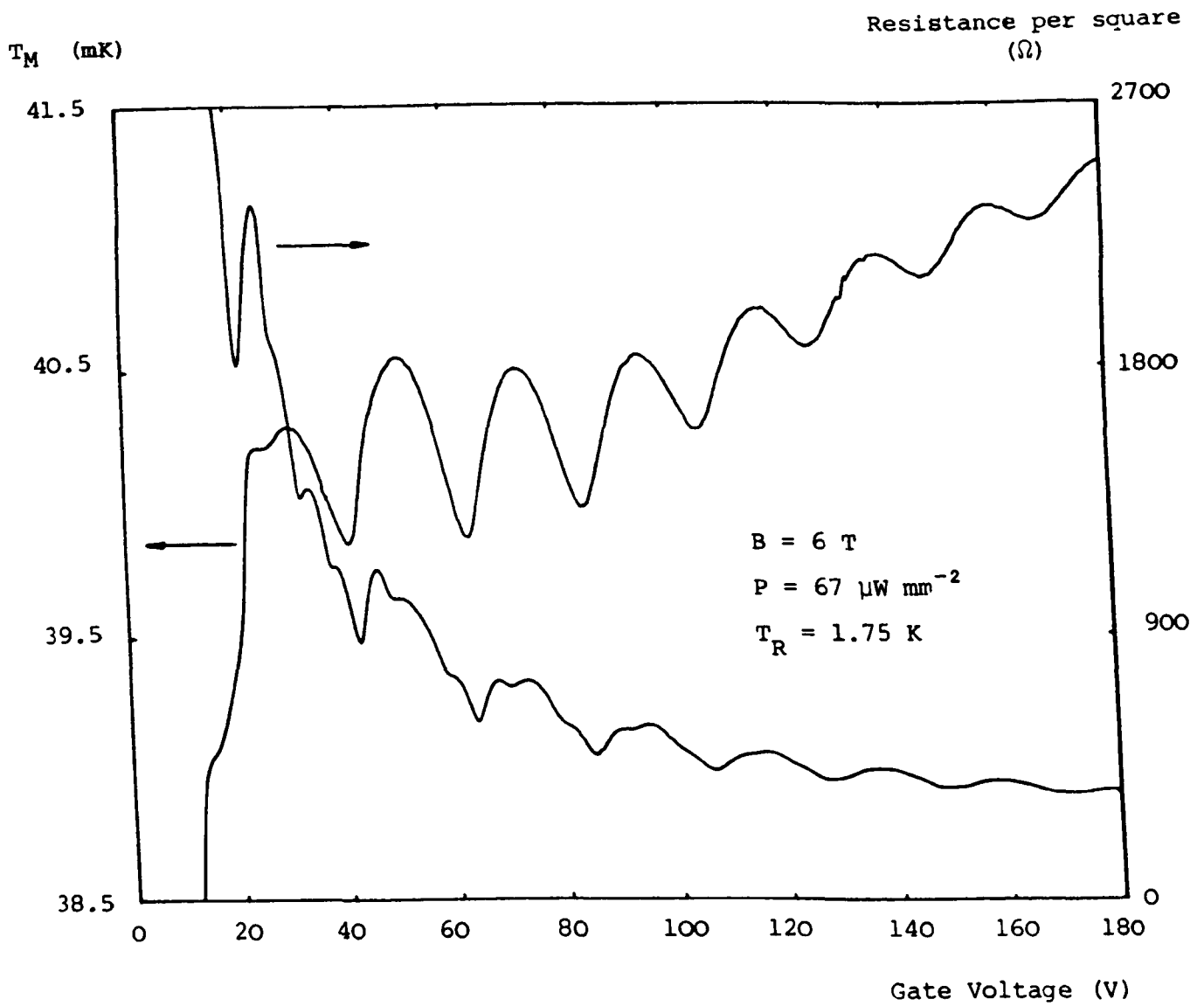


Figure 6.17: The Variation on the Temperature of the Main Thermometer as a Function of Gate Voltage in a Quantising Magnetic Field

shows the variation of the device resistance (R_{sd}) during the phonon emission experiment. The maxima in the temperature of T_M occur when R_{sd} is a maximum and this corresponds to the Fermi level being within a Landau level.

If we assume that the electron temperature does not change significantly with the application of a magnetic field Figure 6.12 indicates that the width of the electron energy distribution ($\sim k_B T_e$) is far less than the Landau level separation ($\hbar\omega_c$) for large magnetic fields. Hence, the emitted phonons arise from intra-Landau level transitions. This regime is close to the Quantum Hall regime and for very low powers plateaux are seen in the electrical measurements (distinct plateaux are seen when $\rho_{xy} \gg \rho_{xx}$ because the measurements are of source-drain resistance due to the lack of Hall probes on the samples used and the source-drain resistance is a combination of ρ_{xx} and ρ_{xy}). The lack of Hall probes on the samples prohibits a detailed study of these plateaux. Measurements using the source and drain contacts do not show exact quantisation due to contact effects, and close investigation reveals the plateaux to have structure, and no distinct breakdown current. The presence of the plateaux, however, indicates that the current distribution in the sample is distorted when the Fermi level is between levels, and that the 2DEG may well have hot spots at the corners as discussed in section 3.6.4. The presence of hot spots will reduce the temperature of T_M as some of the phonon flux will be emitted away from the thermometer contact situated directly opposite the middle of the 2DEG as shown schematically in Figure 6.18. Remembering that the power dissipated by the device is kept constant, sweeping the Fermi level will switch the phonon emission from occurring predominantly

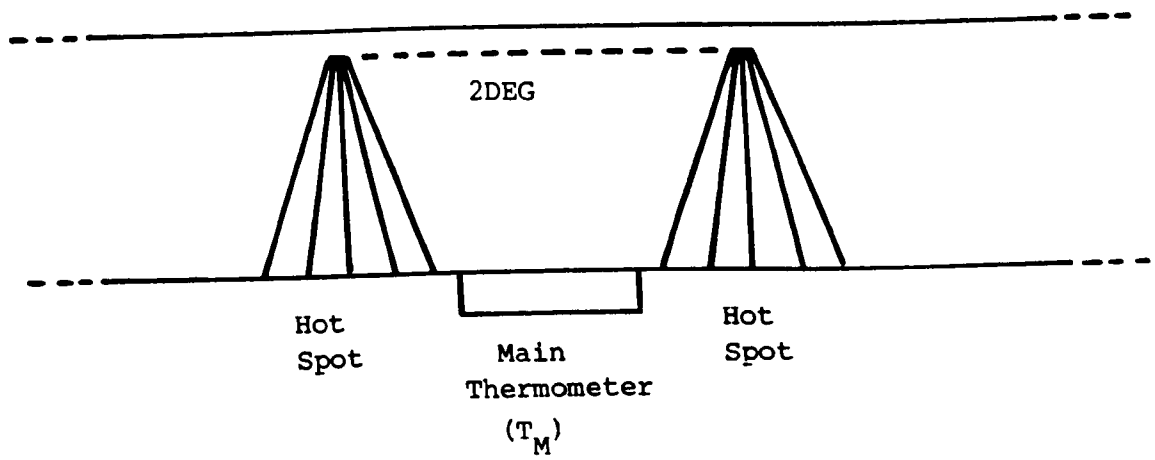


Figure 6.18: Schematic Diagram Showing Phonon Emission in the Quantum Hall Regime

at the corners when the Fermi level is between levels, to uniformly across the 2DEG when the Fermi level is within a Landau level. This will give rise to the oscillations in Figure 6.17. The oscillations are still present for very low powers. Figure 6.19 shows data for $P = 0.17 \mu\text{W mm}^{-2}$ ($T_R = 1.1 \pm 0.1 \text{ K}$) which is at a low enough power for plateaux to be seen in the electrical measurements indicating that we are in the Quantum Hall regime (the temperature scale is uncalibrated as the germanium resistance thermometer used to calibrate the carbon resistors is itself only calibrated for $T > 1.5 \text{ K}$). At this power we estimate that $T_e - T_R = 0.5 \text{ K}$ giving $T_e = 1.6 \text{ K}$.

Support for the argument that some of the phonon flux is missing the thermometer is given in Figure 6.20. Here the variation in the temperature difference between the top and the bottom of a particular temperature oscillation of T_M is shown as a function of device power for three magnetic fields. As the device power is increased we would expect the size of the oscillation to increase linearly if a constant proportion of the phonon flux were missing the thermometer. Considering the data for $B = 6 \text{ T}$ this is seen for $P < 25 \mu\text{W mm}^{-2}$. Presumably above this power the breakdown of the Quantum Hall Effect reduces the rate of increase in the size of the oscillation. For the lower magnetic fields the results are not clear enough to draw useful conclusions.

The transition from the zero field situation, to the situation in a high magnetic field is shown in Figure 6.21 (this data is corrected for the changes in the measured ΔT arising from the magneto-thermal conductivity of the Si(B) substrate and for changes in the sample temperature resulting from the magneto-thermal

T_M (Uncalibrated)

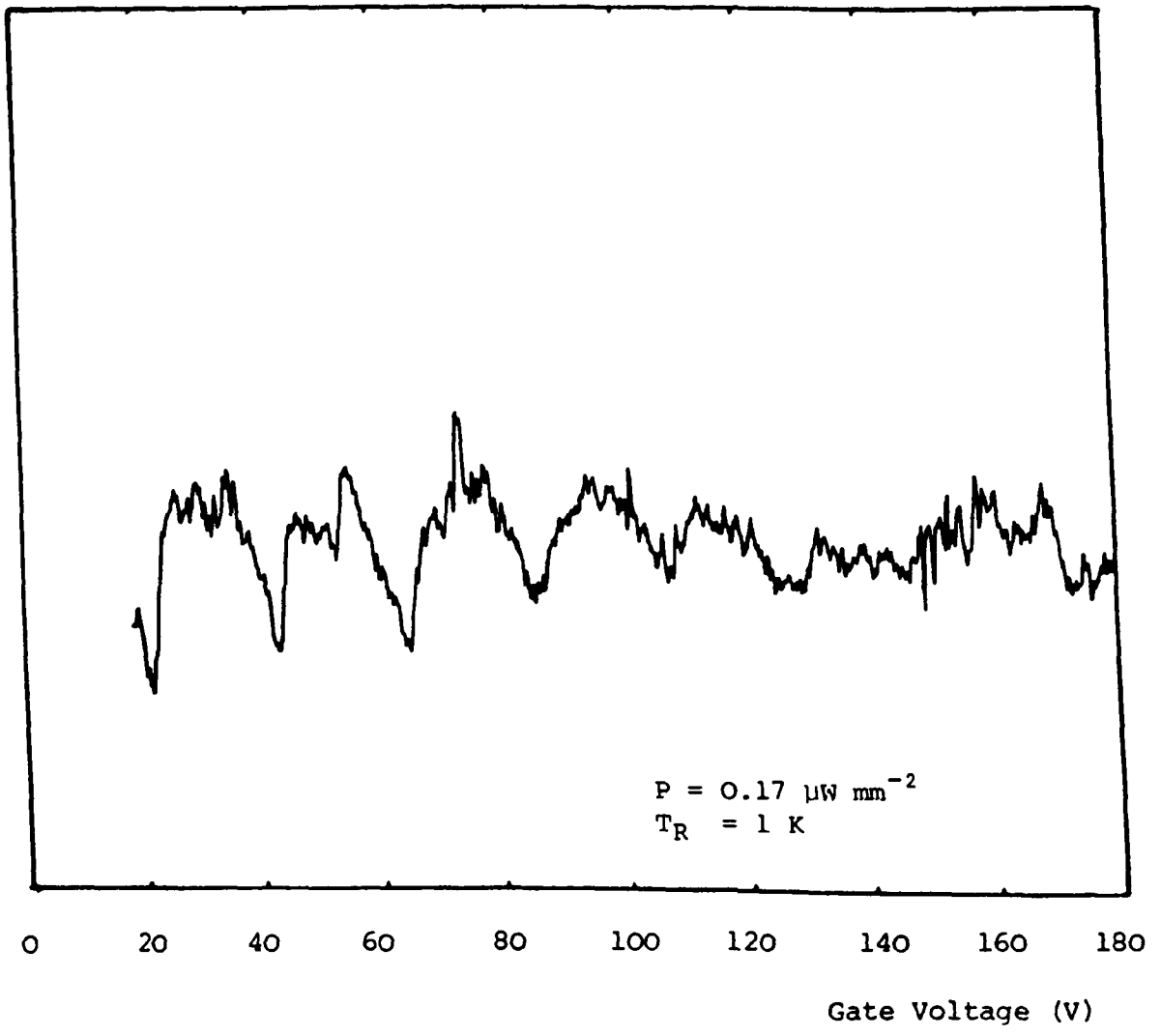


Figure 6.19: The Variation of the Temperature of T_M as a Function of Gate Voltage for Very Low Power Dissipation

Temperature Oscillation (mK)

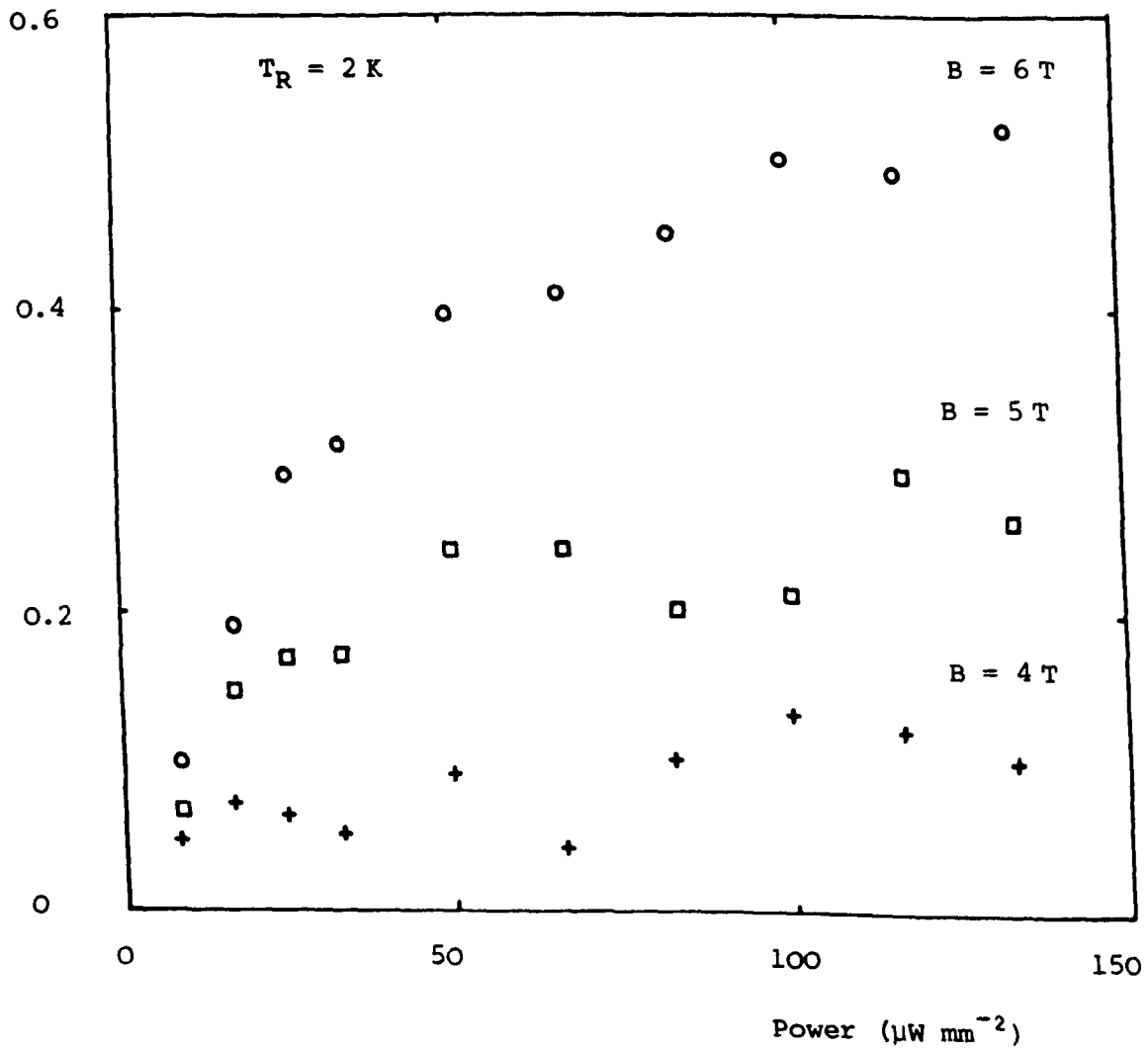


Figure 6.20: The Variation of the Measured Change in Temperature Difference for the Oscillation Corresponding to the 4th Landau Level as a Function of Gate Voltage

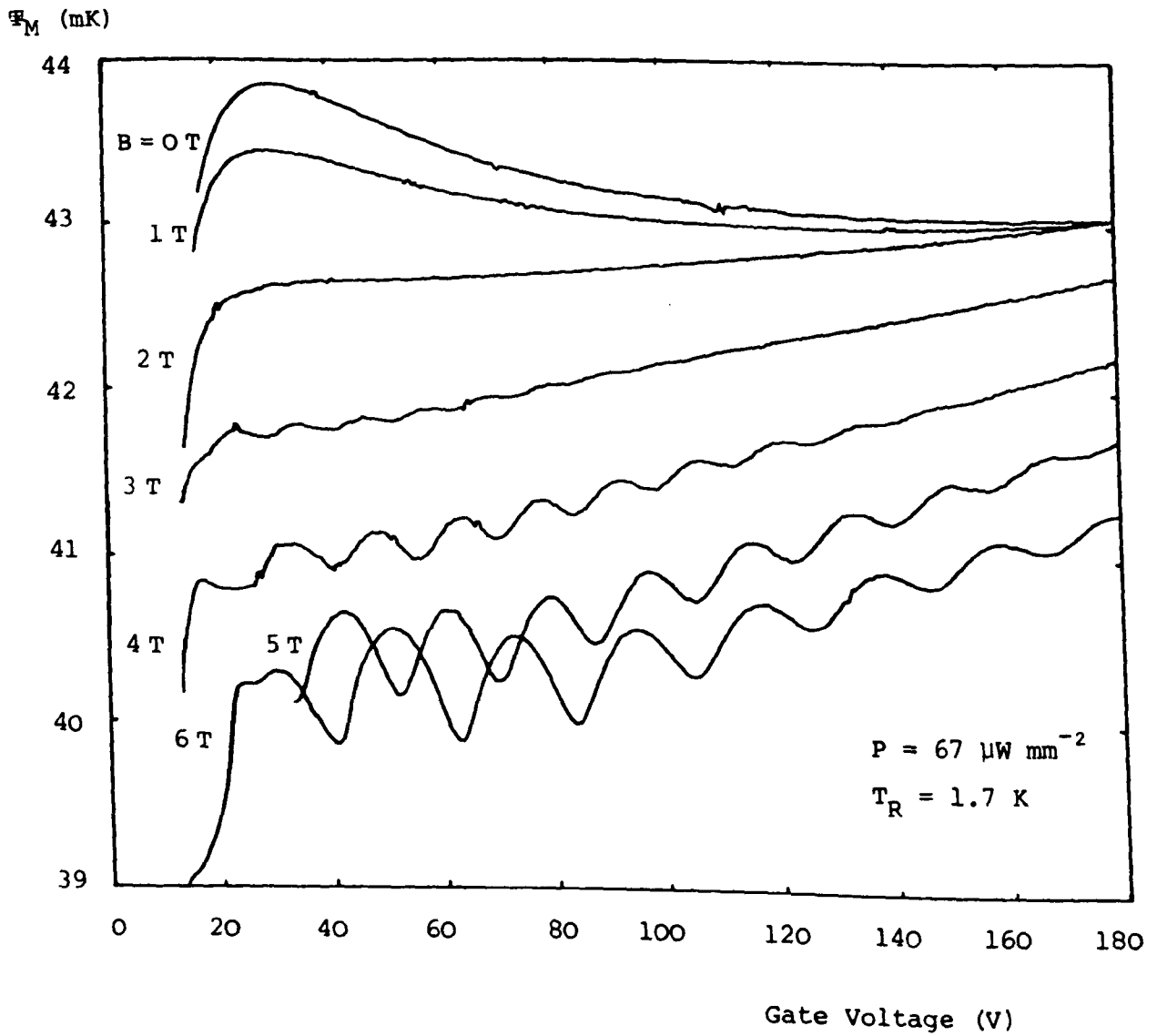


Figure 6.21: The Effect of Applying a Quantising Magnetic Field to the Temperature of T_M Measured Relative to T_R

conductivity of the apparatus discussed in section 2.6.3 using the temperature gradient measured with the resistive heater H2). We focus particularly on the peaks in T_M where E_F is inside a Landau level and the emission at least at the higher fields is from intra-Landau level transitions. It is apparent that the application of the magnetic field is removing the increase in the temperature of T_M as V_g (k_F) is reduced caused by the coning imposed by the $2k_F$ cut-off. This is surprising for although the magnetic field destroys the Fermi circle, it produces circular Landau levels in k -space broadened by electron scattering which when the Fermi level lies within a Landau level will allow scattering to occur around the level with the maximum possible q_{\parallel} given by twice the radius of the Landau level. This limit on the maximum q_{\parallel} that can be emitted is exactly like the zero field situation, and if successive Landau levels are considered, the restriction on q_{\parallel} relaxes as $n_s^{\frac{1}{2}}$. The constraint on q_z ($q_z < 1/a$) set by the thickness of the 2DEG is also present as this is unchanged by the application of the magnetic field.

The width of the Landau level will also impose a cut-off in the maximum energy of phonons that can be emitted in an intra-Landau level transition. Ando (1977) gives the width of the Landau levels as

$$2\Gamma = 2\left(\frac{2}{\pi} \hbar\omega_c \hbar/\tau\right)^{\frac{1}{2}} \quad (6.3)$$

when only short range scattering potentials are considered. Here τ is the zero field relaxation time which is obtained from the

mobility measurements. Evaluating this for $P = 67 \mu\text{W mm}^{-2}$ and $B = 6 \text{ T}$ the Landau level width 2Γ is 550 GHz for the peak mobility ($V_g = 31 \text{ V}$, $\tau = 1.16 \times 10^{-9} \text{ s}$) and 860 GHz for $V_g = 180 \text{ V}$. This restriction will, hence, affect the phonon emission as the peak in the phonon distribution is 480 GHz for this power and so black body emission would span a range up to $\sim 1000 \text{ GHz}$ (assuming again that the electron temperature is largely unaffected by the application of the magnetic field). The likely result is then that a greater proportion of the phonon emission will be LA phonons as V_g falls and, thus, will reduce T_M by the same argument as in the zero magnetic field case. Another affect of the restriction on the phonon energy imposed by the Landau level width is that the maximum q is limited. Since $\sin\theta = q_{\parallel}/q$, the restriction on θ imposed by reducing V_g and, hence, q_{\parallel} will not be as severe since q is also decreasing.

Support for the Landau level width being important comes from Figures 6.17 and 6.14 ($T_R = 6 \text{ K}$) since the values of T_M corresponding to the peak in the oscillation appear to fall as the mobility increases (producing narrower Landau levels) and then to stop falling and rise slightly in the region of the peak mobility. The flattening and small rise seen, however, occurs somewhat above the value of V_g corresponding to the peak mobility. Unfortunately this is rather difficult to judge, since the sudden decrease in the temperature of T_M for $V_g < 30 \text{ V}$ produced by the restriction on q_z imposed by the width of the 2DEG means that the number of oscillations in this region is limited.

In Figure 6.19 data is shown for very low input power and,

hence, electron temperature. It is apparent that T_M at the peaks of the oscillations is now independent of V_g . This supports the idea that the decrease seen at higher powers is related to the Landau level width which becomes increasingly restrictive on the phonon emission for higher powers and, hence, higher electron temperatures. However, even at this very low power the increase in T_M for low gate voltages seen for the zero field data is not observed. There will be a small increase in mobility at these low electron temperatures reducing the width of the Landau levels further but the zero magnetic field mobility measurements at this power show that this only reduces the Landau level by only 30 GHz.

Considering Figure 6.21 it is apparent that for $V_g = 180$ V the application of the magnetic field is only having a small effect on the temperature of T_M . This is reasonable as the decay in the oscillations makes it clear that the low mobility at these gate voltages is broadening the Landau levels considerably and merging them. This will produce a situation very similar to the zero field case. The merging of the Landau levels will be aided by the presence of the second subband which will produce a second ladder of Landau levels with a different period to those corresponding to the electric quantum limit.

The analysis of the results obtained in a magnetic field has so far neglected the effects of resonant phonon scattering from the raising of the degeneracy of the Γ_0 groundstate of the boron acceptor in silicon by the application of a magnetic field as discussed in section 4.2.3 (the results presented in Figure 6.21 were only corrected for the change in the magneto-thermal conductiv-

ity of the Si(B) as measured using the resistive heater H2). The resonant phonon scattering will remove the sample from the boundary scattering regime so far assumed, and clearly this will reduce the temperature of T_M by removing the geometric enhancement both from the high aspect ratio of the samples and from the phonon focussing arising from placing a thermometer directly underneath the 2DEG. Another, more important, consequence of the resonant phonon scattering will be the effect of the resonant phonon scattering acting as a phonon filter. This offers an alternative explanation to that given above of the dramatic change in the zero and high magnetic field cases. Comparing the $B = 0$ T and $B = 6$ T data in Figure 6.21 it can be seen that T_M for a gate voltage of 180 V has decreased by 1.7 mK ($\sim 4\%$) with the application of the magnetic field. This can reasonably be ascribed to the reduction of the phonon focussing (which raises T_M for phonon emission from a 2DEG 30% above the value obtained with a resistive heater) by scattering occurring in the bulk of the substrate. If we next consider the effect of reducing the gate voltage, the theory in section 4.1.1 and the analysis of the zero magnetic field results in section 6.3.1 make it clear that the restrictions imposed upon q_{\parallel} and q_z increases dramatically the number of low energy phonons emitted. From section 4.2.3 the application of a magnetic field causes resonant phonon scattering to occur at two frequencies given by

$$\nu_{12} = 16.4 B \text{ GHz}$$

and

$$\nu_{13} = 31.5 B \text{ GHz}$$

Thus, for $B = 6$ T we have $\nu_{1,2} = 98$ GHz and $\nu_{1,3} = 190$ GHz. Reducing V_g , therefore, we would expect T_M to fall as the number of phonons scattered resonantly increases. When the restriction on the emitted phonons is so severe that the peak in the phonon distribution falls below $\nu_{1,3}$, the decrease in T_M would be expected to halt over a small range of V_g before falling once again as $\nu_{1,2}$ becomes very important. This describes well the behaviour seen for $B = 6$ T. Figure 6.19 supports this argument as for very low powers the phonon emission without any restrictions is already concentrated at low frequencies and so reducing V_g will not significantly alter the number of phonons resonantly scattered removing the effect.

The use of a magnetic field to sweep the resonant phonon scattering energy through the phonon emission spectra may well provide a useful alternative to the experimentally more demanding stress method discussed in section 6.5 and this will be discussed in section 6.6.

Von Klitzing et al (1985) showed that in the Quantum Hall regime infra-red emission was occurring at the corners of the 2DEG when the Fermi level was between Landau levels. Using the technique described in section 6.3.1 any FIR emission can be monitored with the reference thermometer T_R . Measurements were made for $B = 6$ T and $P = 67 \mu\text{W mm}^{-2}$ but no difference in the temperature of T_R could be seen as the Fermi level was moved through the Landau levels. This failure to detect any significant FIR emission probably arises from the detection limit of 10^{-8} W that is possible with this technique. Although Von Klitzing does not discuss the detection limits we can

conclude from Hopfel and Weimann (1985) who use a similar experimental arrangement that FIR powers down to 10^{-13} W can be detected. Another factor contributing to this failure is that at the power levels used the Quantum Hall Effect has broken down significantly reducing the electric field gradients at the corners. For low gate voltages ($V_g < 15$ V) the temperature of T_R did fall, indicating FIR emission. The fall seen duplicated the results obtained in the zero magnetic field situation shown in Figure 6.10.

6.5 THE STRESS TUNED PHONON FILTER

The work presented in Section 4.3.2 and by Russell (1988) shows that the application of uniaxial stress along the [110] direction (along the length of the samples used in these experiments) will cause the degeneracy of the four-fold Γ_6 groundstate of the boron impurity in silicon to be lifted. The two Kramers doublets formed have an energy splitting, Δ , proportional to the applied stress and resonantly scatter phonons of this energy. This will "burn" a hole in the phonon energy distribution situated at Δ . By varying the applied stress this hole can be swept through the phonon energy distribution altering the measured thermal conductivity which can then be used to deduce the original phonon energy distribution.

Figure 6.22 shows preliminary results obtained from the Si(B) substrates before the MOSFET fabrication. In this experiment a resistive heater was positioned at the end of the sample (H2) with the two thermometers situated between the heater and the heat sink. The results show good qualitative agreement to the expected black

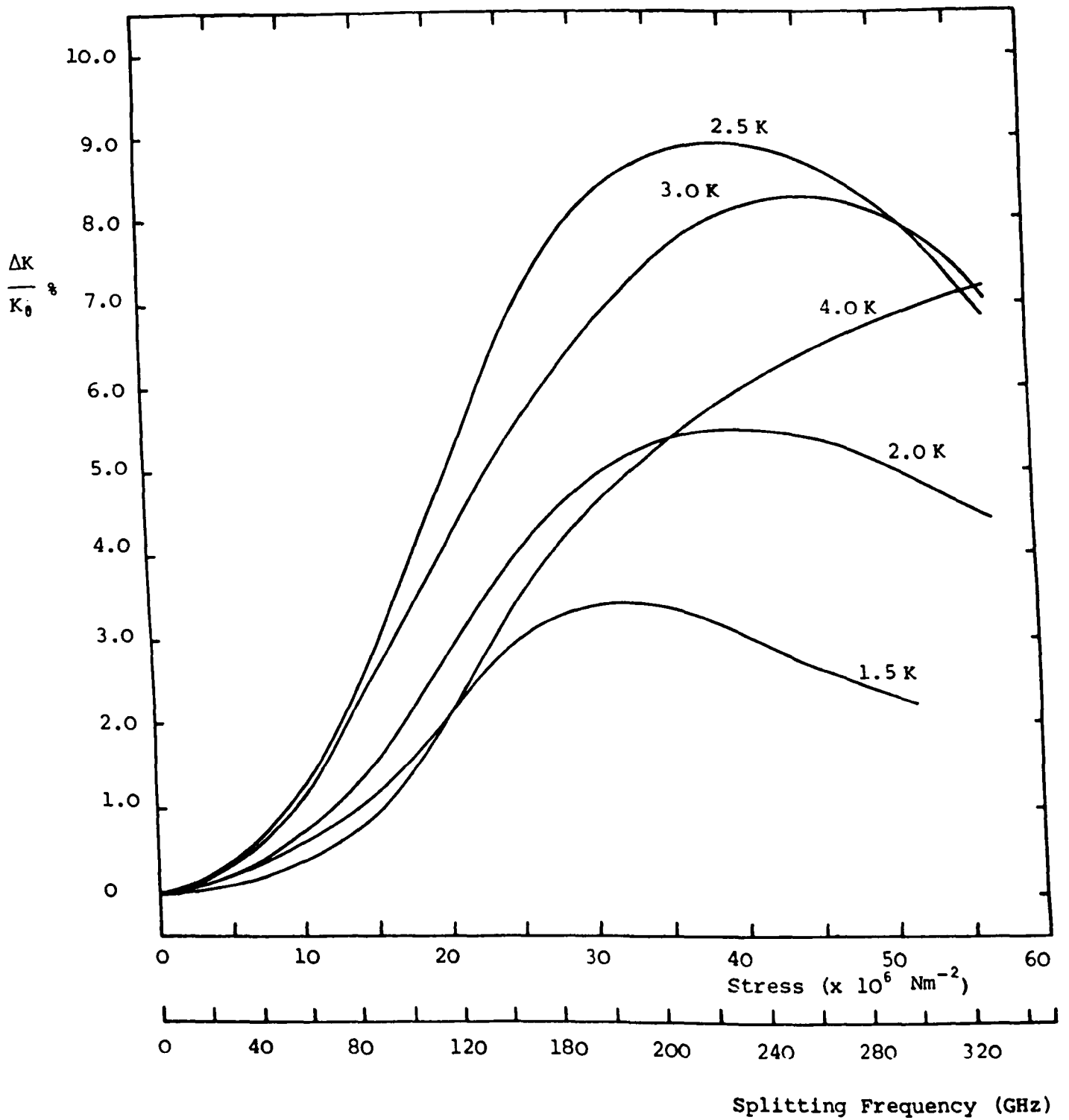


Figure 6.22: The Variation of Thermal Conductivity with Applied Uniaxial Stress

body phonon energy distribution with the peaks moving to higher energy with increasing temperature, however, the peaks in the measured spectra do not occur at the expected energy of $3.8k_B T_R$. This was found to be due to the variation in the width of the hole with applied stress. This width is proportional to the square of the energy splitting, and will weight the peaks to higher values of energy. Russell calculated the effect of this weighting, and found that the resulting energy of the peaks was $5.9k_B T_R$ in agreement with the measured spectra. Russell also calculated the expected change in thermal conductivity for the concentration of boron present in the samples and found that the experimental results produced significantly greater effect than that predicted theoretically.

It was hoped to use this technique to probe the frequency of the phonons emitted from a heated 2DEG. Unfortunately this experiment was never successful during the course of this work due to the difficulty of the technique. Applying stress changes the thermal conductivity of any contacts between the sample and the 1 K helium pot as outlined in section 2.6.3, and this alters the temperature of the sample and the measured temperature difference. Another factor complicating the experiment is that the temperature of the reference thermometer will also vary with stress as the thermal conductivity of the Si(B) between T_R and the heatsink changes. The change in temperature of T_R will correspond to the black body phonon spectrum of the temperature of the lattice and not the phonon energy distribution from the 2DEG. Further problems in the analysis of the results will arise from the change in the phonon focussing patterns caused by the application of the stress.

6.6 CONCLUSIONS AND FUTURE EXPERIMENTS

The experimental work presented in this thesis investigates the electron-phonon interaction at low device powers comparable with those used for electrical investigations into the behaviour of 2DEGs. It is also complementary to the heat pulse work at higher powers as it permits quantitative analysis.

The zero magnetic field results show the $2k_F$ cut-off distinctly. In addition, the cut-off arising from the variation in the 2DEG width as a function of gate voltage is also found to be important in the high resistivity samples used. These two cut-offs act together to limit the maximum emitted phonon frequency. This effect would be very interesting to investigate using the stress tuned phonon filter if the technique can be made to work, and the results successfully analysed. The samples are very interesting electrically since their high mobility ($12,000 \text{ cm}^2 \text{ V}^{-1} \text{ s}^{-1}$) and low threshold voltage ($\approx 0.6 \text{ V}$) allow the effect of the temperature dependence of screening to be investigated. Further electrical studies on these samples using a Hall bar geometry to increase the accuracy of the measurements could provide useful information on the effect of screening on the electron-phonon interaction which, from the experiments, is clearly an important effect. This effect should also be included in the theory of Challis et al (1987) to determine the effect on the angular emission. Theoretical calculations on the effect of electron temperature on the phonon emission when the emission is severely restricted would also be very interesting.

The samples show unexpected localisation effects in the

range $8 \text{ V} \leq V_g \leq 35 \text{ V}$ which need to be studied further as this range covers the most interesting region of the phonon emission experiments. The application of small magnetic fields in conjunction with electrical measurements would indicate whether the effects are due to coherent interference of the electronic states.

The results obtained in a quantising magnetic field show trends that seem initially to contradict those predicted by the phonon emission theory. Two possible explanations exist. (1) The Landau level width is restricting the phonon emission causing a greater proportion of the emitted phonons to be LA. (2) The splitting of the Γ_0 level by the magnetic field is resonantly scattering low frequency phonons emitted by the 2DEG and is, thus, making T_M sensitive to the emitted phonon spectrum. Both explanations are reasonable and so more work should be done to determine which is correct. Experimentally this may be achieved by using a large magnetic field parallel to the plane of the 2DEG which will produce resonant phonon scattering from the split Γ_0 groundstate while leaving the 2DEG largely unaffected. If it is found that the Γ_0 groundstate can be used as a magnetically tunable phonon filter this may well prove to be a powerful tool in probing the phonon emission from a 2DEG although large magnetic fields are required to probe high frequency phonons arising, for example, from cyclotron phonon emission.

To further investigate the temperature oscillations seen in a quantising magnetic field will require measurements with smaller thermometers situated directly opposite the corners of the device. This will allow the temperature of the corners to be determined when

the current distribution in the sample is severely distorted. An extension of this experiment would have the small thermometers situated along the length of the 2DEG. With this geometry it should be possible to monitor the breakdown of the Quantum Hall Effect starting at the corners and spreading throughout the 2DEG. This would test the QUILLs model proposed by Eaves and Sheard (1986).

The transition from intra-Landau level scattering to inter-Landau level scattering would be interesting to investigate. Unfortunately the high power required in the present large area devices to raise the electron temperature sufficiently also raises the lattice temperature, severely limiting the sensitivity of the thermometers. Thus, to investigate inter-Landau level scattering, it will be necessary to use smaller area devices allowing the electron temperature to be raised sufficiently while dissipating less power into the lattice. An alternative method would be to use pulse heating with a very asymmetric duty cycle. This would allow the average power to be low, while the electron temperature during the "on" part of the cycle could be high.

The failure to obtain useful results with the stress-tuned phonon filter indicates the difficulty of measuring temperature differences accurately while applying stress. During this work the pair of carbon resistors used became unstable due to the frequent thermal cycling that occurred during the debugging of the experiment and this contributed to the problems encountered during the later experiments when applying stress. It may, however, be necessary to redesign the stress apparatus to make it function more satisfactorily.

An obvious extension of the work presented in this thesis would be to use HEMT structures fabricated from GaAs/AlGaAs. However, problems arise from the low resistance of the 2DEG in these devices due to their very high mobility, and the comparatively large resistances of the ohmic contacts to the 2DEG. These two effects will produce a small phonon flux due to the two-dimensional effects, superimposed on a large black-body background. Further problems will arise from current leakage into the 2DEG from the gate used to control the carrier concentration.

APPENDIX A

This appendix contains an annotated listing of one of the programs used to produce the results presented in Chapter 5. This program corresponds to the model presented with the variable source temperature and the phonon emission limited to $\pm 30^\circ$ to the plane of the 2DEG.

```

DOUBLE PRECISION W,T,G,U,W2,U2,XA,XB,XC,XD,YA,YB,YC,YD
DOUBLE PRECISION E,RAX,RAY,RCX,RCY,DTH,CTH,DIFF,DCHK
DIMENSION W(128,128)
DIMENSION T(128),G(124),U(128)
DIMENSION W2(128,128),U2(128)
DIMENSION XA(128),XB(128),XC(128),XD(128)
DIMENSION YA(128),YB(128),YC(128),YD(128)
OPEN(7,FILE='RESULT7-DAT')
DO 10 I=1,60
    XA(I)=0.1*(60-I)
    YA(I)=0.38
    XC(I)=0.1*(61-I)
    YC(I)=0.38
10  CONTINUE
DO 20 I=65,124
    XA(I)=0.1*(I-65)
    YA(I)=0
    XC(I)=0.1*(I-64)
    YC(I)=0
20  CONTINUE
DO 30 I=61,64
    XA(I)=0
    YA(I)=0.095*(65-I)
    XC(I)=0
    YC(I)=0.095*(64-I)
30  CONTINUE
DO 40 I=125,128
    XA(I)=6
    YA(I)=0.095*(129-I)
    XC(I)=6
    YC(I)=0.095*(128-I)
40  CONTINUE
DO 50 I=1,124
    T(I)=0.5
50  CONTINUE

```

Initialise
Arrays

Open data file

Set the geometry
of the model

Initialise the
element temperature

```

DO 60 I=1,128
  XB(I)=0.5*(XA(I)+XC(I))
  YB(I)=0.5*(YA(I)+YC(I))
  XD(I)=YC(I)-YA(I)
  YD(I)=XA(I)-XC(I)
  E=SQRT(XD(I)*XD(I)+YD(I)*YD(I)+0.00000001)
  XD(I)=XD(I)/E
  YD(I)=YD(I)/E
60 CONTINUE
WRITE(6,*) 'FINISHED SETTING UP NOW ON MATRIX'
DO 70 I=1,128
  DO 80 J=1,128
    IF(J.EQ.I) W(I,J)=0
    IF(J.EQ.I) GO TO 80
    XR=XB(J)-XB(I)
    YR=YB(J)-YB(I)
    E=SQRT(XR*XR+YR*YR+0.0000000001)
    XR=XR/E
    YR=YR/E
    CTH=ABS(XR*XD(I)+YR*YD(I))
    RAX=XA(J)-XB(I)
    RAY=YA(J)-YB(I)
    E=SQRT(RAX*RAX+RAY*RAY+0.0000000001)
    RAX=RAX/E
    RAY=RAY/E
    RCX=XC(J)-XB(I)
    RCY=YC(J)-YB(I)
    E=SQRT(RCX*RCX+RCY*RCY+0.0000000001)
    RCX=RCX/E
    RCY=RCY/E
    DTH=ABS(RCX*RAX+RCY*RAY)*0.9999999
    DTH=ACOS(DTH)
    W(I,J)=CTH*DTH
    W2(I,J)=0
    IF(CTH.GT.0.866) W2(I,J)=CTH*DTH
80 CONTINUE
    U(I)=0
    U2(I)=0
    DO 90 J=1,128
      U(I)=U(I)+W(I,J)
      U2(I)=U2(I)+W2(I,J)
90 CONTINUE
    DO 100 J=1,128
      W(I,J)=W(I,J)/U(I)
      W2(I,J)=W2(I,J)/U2(I)
100 CONTINUE
70 CONTINUE
DO 110 I=1,124
  G(I)=0
110 CONTINUE
DO 120 I=41,50
  G(I)=1/U(I)
120 CONTINUE

```

Calculate
linking
coefficients
between
elements

Set emission angle
for source elements

Normalise linking
coefficients

```

DO 130 I=61,124
  G(I)=0
  DO 140 J=41,50
    G(I)=G(I)+W2(J,I)
140    CONTINUE
      G(I)=G(I)/U(I)
130    CONTINUE
      NUM=128
      WRITE(7,*) NUM
      DO 450 I=1,128
        WRITE(7,*) U(I)
450    CONTINUE
      DO 460 I=1,128
        WRITE(7,*) U2(I)
460    CONTINUE
      WRITE(6,*) 'FINISHED W(I,J) STARTING ITERATION'
      DCHK=99999
      DO 150 II=1,2000
        DO 160 I=1,124
          T(I)=G(I)
          DO 170 J=1,124
            T(I)=T(I)+W(I,J)*T(J)
170          CONTINUE
160          CONTINUE
            WRITE(6,*) T(5),T(20),T(50),T(80)
            DIFF=ABS(T(80)-DCHK)
            IF (DIFF.LT.0.00001) II=2000
            DCHK=T(80)
150          CONTINUE
            DO 180 I=1,128
              WRITE(6,*) I,T(I)
              WRITE(7,*) I,T(I)
180          CONTINUE
            CLOSE(7)
            END

```

Calculate an element's temperature

Check if accuracy achieved

Write data to screen

Write data to file

REFERENCES

- Anderson, P.W. (1958), Phys. Rev. 109, 1492.
- Ando, T., Fowler, A.B. and Stern, F. (1982), Rev. Mod. Phys. 54, 437.
- Ando, T. (1977), J. Phys. Soc. Jap. 43, 1616.
- Bardeen, J. and Shockley, W. (1950), Phys. Rev. 80, 72.
- Berman, R., Simon, F.E. and Ziman, J.M. (1953), Proc. Roy. Soc. A220, 176.
- Bhattacharjee, A.K. and Rodriguez, S. (1972), Phys. Rev. B6, 3836.
- Callaway, J. (1959), Phys. Rev. 113, 1046.
- Casimir, H.B.G. (1938), Physica 5, 495.
- Challis, L.J., Toombs, G.A. and Sheard, F.W. (1987), Proc. Karpaz Winter School on Phonon Physics (to be published by Springer, Berlin).
- Chin, M.A., Narayanamurti, V., Stormer, H.L. and Hwang, J.C.M. (1984), Proc. 4th Int. Conf. on Phonon Scattering in Condensed Matter, Stuttgart, FRG, eds. W. Eisenmenger, K. Lassmann and S. Dottinger (Springer, Berlin) p. 328.
- Dietsche, J.W. (1986), Proc. 5th Int. Conf. on Phonon Scattering in Condensed Matter, Urbana, 1986, eds. A.C. Anderson and J.P. Wolfe (Springer, Berlin) p. 366.
- Eaves, L. and Sheard, F.W. (1986), Semiconductor Science and Technology 1, 346.
- Eddison, C.G. and Wybourne, M.N. (1985), J. Phys. C. 18, 5225.
- Eisenstein, J.P., Narayanamurti, V., Stormer, H.L., Cho, A.Y. and Hwang, J.C.M. (1986), Proc. 5th Int. Conf. on Phonon Scattering in Condensed Matter, eds. A.C. Anderson and J.P. Wolfe (Springer, Berlin) p. 401.
- Eisenstein, J.P., Gossard, A.C. and Narayanamurti, V. (1988), Surf. Sci. 196, 445.
- Fang, F.F. and Fowler, A.B. (1968), Phys. Rev. 169, 619.
- Fowler, A.B., Fang, F.F., Howard, W.E. and Stiles, P.J. (1966), Phys. Rev. Letts. 16, 901.
- Ghazi, A.A. (1978), Ph.D. Thesis, University of Nottingham.
- Hardy, G.A. (1989), Ph.D. Thesis, University of Nottingham.

- Hartstein, A., Fowler, A.B. and Albert, M. (1980), Surf. Sci. 98, 181.
- Hensel, J.C., Dynes, R.C. and Tsui, D.C. (1983a), Phys. Rev. 124, 1041.
- Hensel, J.C., Halperin, B.I. and Dynes, R.C. (1983b), Phys. Rev. Letts. 51, 2302.
- Heraud, A.P. (1985), Ph.D. Thesis, University of Nottingham.
- Herring, C. and Vogt, E. (1956), Phys. Rev. 101, 944.
- Holland, M.G. and Neuringer, L.J. (1962), Proc. Int. Conf. on the Physics of Semiconductors, Exeter, 1962, (The Inst. of Physics and the Physical Soc., London) p. 474.
- Hopfel, R.A. and Weimann, G. (1985), Appl. Phys. Letts. 46, 291.
- Howard, W.E. and Fang, F.F. (1976), Phys. Rev. B13, 2519.
- Kawaji, S. (1978), Surf. Sci. 73, 46.
- Kent A.J., Hardy, G.A., Hawker, P., Rampton, V.W., Newton, M.I., Russell, P.A. and Challis L.J. (1987), Phys. Rev. Lett. 61, 180.
- Kleiner, W.H. and Roth, L. (1959), Phys. Rev. Letts. 2, 334.
- Klemens, P.G. (1955), Proc. Roy. Soc. London A68, 1113.
- Kwok, P.C. (1966), Phys. Rev. 149, 666.
- Marx, D. and Eisenmenger, W. (1982), Z. Phys. B. 48, 277.
- McCurdy, A.K., Maris, H.J. and Elbaum, C. (1970), Phys. Rev. B2, 4077.
- Mott, N., Pepper, M., Pollitt, S., Wallis, R.H. and Adkins, C.J. (1975), Proc. Roy. Soc. A345, 169.
- Nakamura, K. (1976), Surf. Sci. 58, 480.
- Newton, M.I. (1987), Ph.D. Thesis, University of Nottingham.
- Odoni, W., Fuchs, P. and Ott, H.R. (1983), Phys. Rev. B28, 1314.
- Olsen, J.L. (1962), in 'Electron Transport in Metals', Interscience Tracts in Physics and Astronomy No. 12, ed. R.E. Marshak (John Wiley & Sons, New York) p. 68.
- Payne, M.C., Davies, R.A., Inkson, J.C. and Pepper, M. (1983), J.Phys. C. 16, 291.
- Pepper, M. (1977), Contemp. Phys. 18, 423.
- Pepper, M. (1985), Contemp. Phys. 26, 257.

Rampton, V.W., Newton, M.I., Kent, A.J., Carter, P.A., Hardy, G.A., Russell, P.A. and Challis, L.J. (1987), Proc. 18th Conf. on Low Temperature Physics, Kyoto, Japanese Journal of Applied Physics 26, Supplement 26-3, 1755.

Rothenfusser, M., Kuster, L. and Dietsche, W. (1986), Phys. Rev. B34, 5518.

Russell, P.A. (1988), Ph.D. Thesis, University of Nottingham.

Schreiffer, J.R. (1957), in 'Semiconductor Surface Physics', ed. R.H. Kingston (University of Pennsylvania Press, Philadelphia) p. 55.

Shinba, Y., Nakamura, K., Fukuchi, M. and Sakata, M. (1982), J. Phys. Soc. Jap. 51, 157.

Smith, R.P. and Stiles, F.J. (1986), Sol. State Comm. 58, 511.

Stern, F. (1974), CRC Critical Reviews in Solid State Physics 4, 499.

Suzuki, K. and Mikoshiba, N. (1971a), Phys. Rev. B3, 2550.

Suzuki, K. and Mikoshiba, N. (1971b), J. Phys. soc. Jap. 32, 164.

Toombs, G.A., Sheard, F.W., Nielson, D. and Challis, L.J. (1987), Sol. State Comm. 64, 577.

Von Klitzing, K., Dorda, G. and Pepper, M. (1980), Phys. Rev. Letts. 45, 494.

Von Klitzing, K., Ebert, G., Kleinmichel, N. and Obloh, H. (1985), Proc. 17th Int. Conf. on the Physics of Semiconductors, San Francisco, eds. D.J. Chadi and W.A. Harrison (Springer, Berlin), p. 271.

Wixforth, A., Kotthaus, J.P. and Weimann, G. (1986), Phys. Rev. Letts. 56, 2104.

Wybourne, M.N., Eddison, C.G. and Kelly, M.J. (1984), J. Phys. C. 17, L607.

ACKNOWLEDGEMENTS

I would like to thank Professors S Clough and C A Bates for extending to me the facilities of the Department and the SERC and the GEC Hirst Research Centre for the award of a CASE studentship.

I am very grateful to my supervisor at Nottingham University, Professor L J Challis, for his constant enthusiasm and support. I must also thank Dr Martyn Wybourne and Mrs Caroline Murray for making my visits to GEC enjoyable, and for considerable technical advice.

Special thanks to Dr Paul Russell who introduced me to the secrets of phonon spectroscopy and helped to keep me sane while working through the small hours.

My thanks to my close colleagues Drs Nick Butler, Paul Russell and Mohammed Sahraoui-Tahar and Ms Fouzia Ouali and Mr John Cooper for their help and advice.

I would like to thank Drs Bryan Gallagher and Tony Kent for many useful discussions and Drs Peter Main and John Owers-Bradley for considerable help with leak detecting.

The experiments would not have been possible without the excellent technical assistance of Mr Malcolm Carter and Mr Barry Hill who had to put up with a great deal. My thanks also to Mr Bill Roys and Mr John Middleton for technical assistance and Mr John

Dennis for supplying the cryogenic liquids.

My thanks to the "lunch club", Paul, Nick, Ian, Bryan, Alberto and Mike who covered an unbelievable variety of topics.

I am very grateful to Paul for proof reading this thesis, and Christina for her skilful typing.

Finally, I would like to thank all my friends for making my three years at Nottingham so enjoyable.